Finite Element Modelling of Smart TRIP Steel Sensors and Systems

David Jonson

Submitted in fulfillment of the academic requirements for the degree of
Doctor of Philosophy in the Department of Mechanical Engineering
at the University of Natal.

Durban, South Africa
January 2003

Abstract

Transformation Induced Plasticity (TRIP) steels undergo a phase transformation when subjected to high levels of mechanical strain. This transformation from a paramagnetic austenitic parent phase to a ferromagnetic martensitic phase is irreversible and the resultant magnetic properties may therefore be used as a measure of strain history. The transformation behaviour of TRIP steels has been recognised as a potential smart characteristic and various proposals have appeared aimed at producing a structure that performs its primary structural function as well a strain sensing function simultaneously. However the strain induced nature of the transformation implies that transformation will occur in areas of high stress concentration and therefore engineered stress concentration features will be required to provide a consistent measure of the changes in the magnetic properties of the material as a function of applied load. In order to predict the performance of smart TRIP steel sensors, an analysis method capable of quantifying the effectiveness of a component in its dual role as structure and sensor is needed. The thesis addresses the development of a methodology for correlating the changing magnetic permeability of TRIP steel sensors and structures with martensitic transformation behaviour. The prediction of the deformation behaviour including transformation is implemented by considering a mechanical analysis based on the finite element method and a constitutive model incorporating strain-induced martensitic transformation kinetics. Extensions to the model which allow for a wide range of deformation rates and temperatures are also discussed. In order to demonstrate the application of the methodology, an analysis of a simple tensile element used in strain measurement applications is presented. The analysis also includes the effect of temperature on the performance of the sensor. An analysis of a design proposal for a smart aircraft bolt is also included to investigate the effects of geometry, particularly engineered stress concentrations, and sensor placement.

Declaration

I declare that this dissertation is my own unaided work except where due acknowledgement is made to others. This dissertation is being submitted for the Degree of Doctor of Philosophy to the University of Natal, Durban, and has not been submitted previously for any other degree or examination.

David Jonson January 2003

Acknowledgements

I would like to express my gradtitude to my supervisors, Professor Viktor Verijenko and Professor Sarp Adali for their support and encouragement.

List of Figures

2.1 A Comparison of the Tensile Properties of Structural Steels [97]. . . . 14

2.2 Representative Engineering Stress-Strain Curves for Structural Materials [97]. 14

2.3 Stress-Strain Curves for a Structural Grade Steel and a Low-Strength TRIP Steel [97]. 15

2.4 A True Stress - Strain Curve Divided into Pre and Post-Necking Regimes [94]. 17

2.5 True stress-strain curves for a HSLA steel and a type I TRIP steel [55]. 17

2.6 High Cycle Fatigue Properties of a TRIP Steel and High Performance Structural Steels [55]. 20

2.7 Generic strain-induced martensitic phase transformation curve. 22

2.8 Stress-strain curves (top) and Hall output-strain curves (bottom) for Fe-8.4Cr-8.4Ni-2.1mn-0.262C TRIP sensor material [101] 25

2.9 Hall unit output as a function of displacement for a candidate sensor material [100]. 27

2.10 Idealized behaviour of an installed sensor element in a bridge monitoring system [100]. 27

2.11 Hall Unit Output as a Function of Displacement for Three Different Strain Rates [100]. 30

5.1 Strain monitor attachment 98

5.2 TRIP steel sensor element geometry 101

5.3 The stress - strain relationships for 304 stainless steel at various temperatures [201] 102

5.4 The martensite volume fraction as a function of plastic strain for 304 stainless steel at various temperatures 104

5.5 Finite element model of TRIP steel sensor element 104

5.6 Finite element model of sensor element for magnetostatic modelling . 105

5.7 Inductance change as a function of sensor displacement at various temperatures 107

5.8 Geometry of the aircraft bolt 111

5.9 Finite element model of the aircraft bolt 112

5.10 Finite element model for magnetostatic analysis of the aircraft bolt . 113

5.11 Detailed view of the megnetostatic response model of the aircraft bolt. 114

5.12 Inductance change vs. bolt extension for various temperatures 115

5.13 Inductance change measured for head sensors (both grooved and ungrooved) and thread sensor for TRIP aircraft bolt 116

List of Tables

2.1 Energy Absorption Characteristics for TRIP Steels and HSLA 4340 Steels 19

5.1 Dimensions of sensor element 101

5.2 304 stainless steel martensite evoluation parameters 103

Contents

Declaration i

Acknowledgements ii

1 Introduction 1

2 Structural Health Monitoring and TRIP Steels 4

2.1 Introduction 4

2.2 Smart Structural Health Monitoring Technology - A General Overview 6

2.2.1 Sensing systems 7

2.3 Current Research Issues in Smart Structural Health Monitoring Technology 8

2.3.1 Sensing Technology 8

2.3.2 Damage Interpretation Identification Analysis 9

2.4 Strain Memory Alloys - Transformation Induced Plasticity Steels . . . 11

2.4.1 Background 12

2.4.2 Structural Characteristics of TRIP Steels 13

2.4.3 Strain Memory Alloys as Smart Materials 19

2.5 Feasibility of Metastable Alloys as Deformation Sensing Materials . . 21

2.5.1 Characteristics of Metastable Alloy Sensors 21

2.5.2 The Ferromagnetic Response of Strain Memory Alloy Sensors 26

3 Response Modelling using the Finite Element Method 32

3.1 Introduction 32

3.2 The Concept of the Finite Element Method 33

3.3 A Brief History of The Finite Element Method 35

3.4 Theoretical Formulation 36

3.4.1 Continuum Problems 36

3.4.2 Problem Statement 37

3.4.3 The Variational Approach 38

3.4.4 Basic Two-Dimensional Element Shapes 45

3.4.5 Basic Element Shape Functions for Two-Dimensional Problems 46

3.4.6 Discretisation of the Problem Domain 49

3.5 Mechanical Response Modelling - The Application of the Finite Element Method to Solid Mechanics Problems 50

3.5.1 Formulation for Small Deformation Two-dimensional Elastic Problems 50

3.5.2 Displacement Interpolation Functions 51

3.5.3 Element Stiffness Equations 52

3.5.4 The System Equations 56

3.5.5 Formulation for Small Deformation Non-Linear Problems . . . 56

3.5.6 Finite Deformation Formulation 60

3.6 Magnetostatic Response Modelling - The Application of the Finite Element Method to Linear Magnetostatic Problems 68

3.6.1 Finite element formulation 68

3.6.2 Boundary Conditions 70

3.6.3 Open boundary problems 71

3.6.4 Solvers 73

4 Development of Constitutive Equations for TRIP steels **74**

4.1 Introduction 74

4.2 Kinetics of Martensite Transformation 75

4.2.1 Nucleation and Growth of Martensite 75

4.2.2 The Olsen-Cohen Transformation Model 77

4.2.3 The Stringfellow Transformation Model 80

4.2.4 The Tomita-Iwamoto Transformation Model 83

4.3 Constitutive Equation Formulation 84

4.3.1 The Eshelby Inclusion Model 85

4.3.2 The Stringfellow Constitutive Model 89

4.3.3 The Tomita-Iwamoto Constitutive Models 94

5 Mechanical-Magnetostatic Response Modelling Examples 97

5.1 Introduction 97

5.2 TRIP Steel Sensor Element 100

5.2.1 Geometry 100

5.2.2 Sensor Material Characterisation 100

5.2.3 Finite Element models 103

5.2.4 Results and Discussion 106

5.3 Aircraft Bolt 110

5.3.1 Geometry 110

5.3.2 Material properties 111

5.3.3 Mechanical response model 111

5.3.4 Magnetostatic response model 112

5.3.5 Results and Discussion 114

6 Conclusion 121

Chapter 1

Introduction

Structural health monitoring (SHM) is becoming an important issue as the costs associated with the replacement of damage prone and aging infrastructure and equipment become increasing unaffordable. There is currently interest in the development of structural health monitoring based on the implementation of smart systems for damage sensing and assessment. Smart materials encompass a very broad range of materials which can be manipulated under given input conditions or which have the inherent ability to indicate the amount of damage or deformation. The damage indicating materials fall into two classes; materials which are composites of normal structural materials and sensors to obtain feedback and those which contain an inherent feature that changes with deformation and therefore can be used as a damage indicator. The inherent advantage of the latter class of smart materials is that the material can act as both structure and sensor simultaneously without any need for the attachment of sensors. In addition these smart materials will retain information useful in assessing damage regardless of what happens to the system in the event of power loss etc. This information will be useful for damage assessment and in the utilisation of passive monitoring systems.

Smart SHM technology essentially entails the development of autonomous systems based on the use of smart materials for the continuous monitoring, inspection, and

damage detection of structures with minimum labour involvement. The information acquired by the smart SHM system is automatically monitored and evaluated by a local system or is fed to a remote centre. The development of such systems typically involves different disciplines, for example, structural analysis, material science, computational techniques, signal processing, etc. Many sensors that are currently available or under development, such as fiber optics, dielectric measurement sensors, piezoelectric materials, strain gages and shape memory alloys (SMA), can be used in SHM applications. Transformation Induced Plasticity (TRIP) steels were originally developed as ultra-high strength structural steels with improved toughness as compared with the high-strength, low-alloy steels used for aircraft landing gear and similar applications. TRIP steels display a solid-state, strain dependent phase transformation from a metastable, austenitic parent phase to the thermodynamically stable, martensitic product phase. The product martensitic phase is ferromagnetic due to its body-centered structure whereas the parent austenitic phase is paramagnetic due to its face-centered cubic structure and therefore has no significant ferromagnetic response. It is therefore possible to monitor the extent of deformation in a metastable sensor material using a transformation calibration curve for the particular strain-sensing alloy. Instrumentation may be used to interrogate the material in order to obtain the ferromagnetic response, and ultimately correlate the response with the amount of strain required to produce the corresponding degree of phase transition.

The foundations and some of the practical issues for the development of a mechanical-magnetostatic prediction capability are presented in this work The primary objective is the integration of models for the prediction of the mechanical and magnetostatic response of smart sensors based on strain memory alloys. The prediction of martensite evolution as a function of load requires a well-developed and consistent constitutive model that couples the mechanical parameters with the evolution of martensite within the parent phase. The functional dependence of the martensite evolution on the strain and stress state within the material, various models describing the transformation kinetics and corresponding constitutive formulations

are presented and discussed. The models range from relatively simple treatments in which only the plastic strain is considered to models in which the strain rate, the stress state and temperature influences are included. The solution methodology is based on the use of the finite element method. The versatility and flexibility of the finite element approach allows response predictions for a wide range of sensor geometries and materials to be considered.

The methodology developed to predict the mechanical and corresponding magnetostatic response of strain memory, specifically TRIP steel, components and structures is divided into two phases. The first phase involves the simulation of the martensite transformation as a function of applied loading, i.e. establishing the location and amount of transformed material. This is determined using the finite element method to develop a model incorporating the transformation kinetics and constitutive equations appropriate for TRIP steels. The finite element analyses are implemented as non-linear material models using an updated kinematic formulation. Once the location and amount of transformed material is known a second finite element model is created, this being the magnetostatic model. The magnetostatic model is formulated to included the magnetic permeability of the TRIP steel which is adjusted for each load increment according to the amount of transformed material calculated for any given location within the TRIP steel component. The magnetostatic models are analysed using a simple linear formulation.

In order to demonstrate the application of the numerical modelling methodology, two test-cases are presented. The tests-cases are derived from practical real-world examples of peak strain sensors that are currently under development. The aim of the analyses described are to determine the electrical response characteristics of the peak strain sensors as a function of mechanical loading. The test cases presented concentrate on the analysis of temperature effects and the influence of geometry, demonstrating the application and flexibility of the methodology.

Chapter 2

Structural Health Monitoring and TRIP Steels

2.1 Introduction

Structural health monitoring is an important safety and cost issue that may benefit from the implementation of smart systems for damage sensing and assessment. An example of the critical nature of health monitoring involves the commercial aviation sector where, due to stringent regulatory requirements, high levels of safety and reliability are mandatory. Currently the statistics in respect of catastrophic mechanical failure do not provide sufficient motivation for the installation of structural health monitoring systems (SHMS) as part of the flight package. However, as inspection procedures play an increasingly critical role under current operational safety policies, the possibility that structural health assessment may be compromised by the reliability of inspection must be considered.

The reliability and consequently the cost considerations related to inspection and maintenance procedures are directly influenced by the problems associated with the required sensitivity, poor accessibility and the effects of negative human factors. Structural health and structural performance relate directly to the operational safety

of equipment in that a change in structural health will affect structural performance to a greater or lesser degree. In this context SHM may be considered a safety issue. The possibility and consequence of structural failure are prime considerations in many industries since failure may well lead to fatal accidents. For this reason continuous research in critical areas such as fatigue and corrosion has resulted in high levels of structural reliability. In addition the well-developed understanding of metal behaviour and the provision of accurate quantitative loading descriptions has led to damage tolerant design practices that are well supported by proven inspection techniques. For these reasons any interest in automated (or smart) inspection systems for increased safety would have to be motivated for in terms of greater reliability of inspection. (This may well become an issue in the near future as the world's fleet of ageing aircraft is expected to carry the rapidly increasing volume of air transport).

Another, more important factor stimulating the development of smart SHMS relates to a cost issue, specifically the costs of inspection and consequently the cost of repair. The cost of structural repair may be broadly divided between two groups. The first involves the direct costs associated with the design and implementation of the required repair work. The second involves the indirect costs associated with the removal of the equipment from service and the associated loss of revenue or the cost of leasing substitute equipment. These direct and indirect costs may be minimised by adopting a suitable repair strategy. For example, direct costs may be minimised by repair at an early stage of damage development, or alternatively the indirect costs may be reduced by postponing the repair until a scheduled overhaul. Cost-effective decisions of this type could be made based on an analysis of the quantitative data, relating to the severity and propagation rate of the damage [2].

With regard to the costs of inspection, there is little published data on the potential for cost reductions involved in the use of a smart SHMS, however, a recent study of the inspection requirements for a modern fighter aircraft (with both metal and composite components) has shown that a forty four percent inspection time saving may be possible [2]. In a similar case study involving the costs of the inspection of the wing root structure of the Hercules C130 transport aircraft, it was determined

that the inspection time could be reduced from the 200 person-hours usually required (due to access difficulties) to a few minutes. The above comments indicate that, at present, the potential for cost reduction associated with inspection and repair does provide a strong motivation for the development of smart SHM systems.

The following discussion introduces some of the important issues that are currently receiving attention in the development of SHM systems, however the focus of the discussion involves the possible use of TRIP steel as a sensor material for application in smart SHMS.

2.2 Smart Structural Health Monitoring Technology - A General Overview

Although some conventional non-destructive evaluation (NDE) techniques can be considered within the framework of structural health monitoring, there may be differences in terms of data interpretation between the traditional NDE methods and the SHM approach. Traditional NDE techniques tend to use direct measurements to determine the physical condition of a particular structure. No history data is generally required and the accuracy of the diagnosis strongly depends upon the resolution of the measurements, which, in turn, rely heavily on the equipment. The SHM techniques however use the change in the measurements at the same location at two different times to identify the condition of the structure. Hence, the data history is crucial in the application of the technique and the accuracy of the identification depends strongly upon the sensitivity of the sensors and on the interpretation methods used. Hence, NDE relies more on the equipment, where SHM is more dependent upon the interpretation of the data. The potential direct benefits from such SHM systems as opposed to NDE include [3]:

- In-service, real-time monitoring and reporting thereby reducing maintenance costs associated with scheduled inspection.

- Minimum human involvement which in effect reduces specialised labour requirements, equipment downtime, and the possibility of human error.
- Automatic systems for data acquisition, reporting and analysis which have the potential of improving the safety and reliability of the structure.

2.2.1 Sensing systems

Typically, a built-in diagnostic SHMS, in addition to the host structure, consists of at least two major components, the first being a built-in network of sensors for collecting sensor measurements, i.e. the hardware, and the second being software for the interpretation of sensor measurements in terms of the physical condition of the structure. Depending upon the inputs, the diagnostic systems can be divided into two types; passive sensing systems without known inputs (with sensors only) and active sensors with known inputs (with both sensors and actuators).

Passive Sensing Diagnostics

In a passive sensing system, only the sensors are installed in the structure. Structural integrity is usually ascertained by comparing sensor measurements with a set of reference (healthy) data. The sensor-based system therefore estimates the condition of the structure based on the data comparison. Hence, the techniques used in the comparison of the data for the purposes of condition assessment are crucial in order to ensure reliability of the system. In addition, the system would require either a data bank which has a history of pre-stored data or a structural simulator which could generate the needed reference data. Because the input energy to the structures is typically random and unknown, the corresponding sensor measurements reflect the response of the structures to the unknown inputs. This type of diagnostic capability has been primarily applied to the determination of the unknown inputs which cause the changes in sensor measurements, such as external loads, temperature, pressure, etc.

Active Sensing Diagnostics

In the case of an active sensing system, known external mechanical or non-mechanical loads are input to the structures through built-in devices such as transducers or actuators. Since the inputs are known, the difference in the local sensor measurements based on the same input is directly related to a physical change in the structural condition such as the introduction of damage.

2.3 Current Research Issues in Smart Structural Health Monitoring Technology

In general, a SHMS would include five major parts: sensing technology, diagnostic signal generation, signal processing, identification and interpretation, and integration [3].

2.3.1 Sensing Technology

Many sensors that are currently available or under development, such as fiber optics, dielectric measurement sensors, piezoelectric materials, strain gages and shape memory alloys (SMA), can be used in SHM applications. For example, fiber optics sensors have found applications ranging from civil infrastructures to aircraft structures [4]. Piezoelectric materials have been used as both measurement sensors and as actuators for generating diagnostic signals for monitoring damage in structures made of both metals and composites [10]. Although there are a variety of sensors available on the market, they may not be readily applicable to the condition monitoring of large continuous structures where a distributed network of sensors is required. Accordingly, key technology issues in the sensing are as follows:

Distributed sensor arrays

Techniques need to be developed for the design and implementation of large distributed arrays of sensors. The installation of the sensor network would need to be economical whist still retaining effective performance with regard to specified sensitivity requirements. Other issues in this area include the development of techniques for the retro-fitting of sensors to existing structures.

Remote sensing

Ultimately wireless communication between local sensors and the processor/controller would represent the most effective solution to a large distributed sensor array. As the number of sensors increases with the size of the structure, so does the number of communication wires. The management and handling of large numbers of wires will complicate the installation of the system. With remote sensing capability data could be gathered locally but the structures could be monitored remotely.

Sensor reliability and integrity

The failure of sensors or actuators may result in fault signals or the failure of the entire SMHS. The integrity of sensors and actuators under various loading conditions and environments for particular applications needs to be studied. Issues affecting the long-term behaviour of sensors and actuators also needs to be considered.

2.3.2 Damage Interpretation Identification Analysis

Damage detection and identification analysis plays a major role in a health monitoring system. The accuracy and reliability of the system strongly rely on analysis for relating the sensor measurements to the physical changes in the structure. Sensor measurements are point-wise in the continuous structures and it is likely that

damage or an abnormal condition may not appear at the location where the sensor is located. Therefore, sensor information needs to be extrapolated for damage that occurs at a distance away from the sensor locations. Furthermore, there are many other factors that may influence the sensor measurements beside the particular defects. Hence, it becomes difficult to interpret the sensor measurements in terms of the actual physical condition of the structure.

Mathematically, the determination of the physical condition of a structure based on sensor measurements is a non-linear inverse problem. Several numerical and analytical techniques have been proposed or adopted for the different applications [6]. Modal analyses, system identification, neural network algorithms, generic algorithms etc., have shown some promising results. However, most results are limited to controlled laboratory environments and to simple structural configurations. In practice, most techniques require an extensive amount of history data of the structures in both undamaged and damage conditions, which is usually difficult to obtain. Areas of interest include the following [3]

Damage diagnosis

Novel identification or interpretation algorithms are required to relate the sensor measurements to the physical conditions of the structures in terms of damage and defects.

Damage characterisation

The relationship between damage or defects and the measurable physical quantities of the structure needs to be established. Such quantifiable relationships would provide the necessary foundation for the development of effective identification techniques for different applications.

System Integration

Integration of the system involves aspects related to both hardware and software. Ultimately the system must be reliable. It is a general concern that inclusion of sensors and actuators as a part of the structure may influence or compromise the performance of the structure. Such influence should be minimised as much as possible if it cannot be avoided. In addition the system must be easy to use. It would be desirable that the proposed system could display through its initial interrogation the condition of the structure in a simple format, for example damage severity may be judged on one of the three coloured lights: green - safe to use, yellow- use with caution, needs inspection, and red- unsafe, do not use. More detailed information regarding the structural condition could be obtained if further interrogation is needed.

2.4 Strain Memory Alloys - Transformation Induced Plasticity Steels

Transformation Induced Plasticity (TRIP) steels were originally developed as ultra-high strength structural steels with improved toughness as compared with the high-strength, low-alloy steels used for aircraft landing gear and similar applications. TRIP steels display a solid-state, strain dependent phase transformation from a metastable, austenitic parent phase to the thermodynamically stable, martensitic product phase.

The strain-induced phase transformation is responsible for the large values of ductility and strain-hardening that are observed in these steels. The phase transformation is triggered as the material begins to yield and enters the plastic deformation regime. The extent of the transformation increases with the applied strain resulting in an increasing martensitic fraction. Observation during tensile testing indicates that transformation occurs inhomogeneously along the gauge length of the tensile spec-

imen, regions where martensite has formed become stronger than the rest of the gauge length thereby delaying necking of the specimen. Once the transformation progresses to a significant degree along the entire gauge length the specimen deforms homogeneously throughout the gauge length until failure. Failure typically occurs with very little or no necking. Specimen elongations of 40 to 60% have been observed for materials with yield strengths of 1379 MPa. These levels of ductility are high when compared with those of high strength steels where elongations are typically in the range of 10 to 15%. Much attention has been directed at investigating TRIP steels [7] - [57] particularly the strain induced martensite phase transition [21], [45] - [47], [51], [52], [55], [56].

Besides the obvious advantages offered by the above mentioned structural properties, the transformation from an austenitic face-centered cubic (FCC) crystal structure parent phase to a martensitic body-centered cubic (BCC) product phase results in a change in the magnetic properties of the steel. The magnetic signature of the steel is therefore dependent on the fraction of martensite present and thus changes as the transformation progresses with increasing levels of strain. This behaviour provides the principle basis for a structural health monitoring system.

2.4.1 Background

Researchers have recognized that certain austenitic stainless steels are metastable with respect to deformation [58] - [72]. Early work in this area was centered on understanding the nature of the phase transformation and the associated changes in mechanical behaviour accompanying the phase transition. Attention was directed at ausforming, a fabrication method involving a thermo-mechanical treatment whereby metastable austenite is warm-rolled to produce a high dislocation density thereby increasing the yield strength of the material [73] - [75]. This warm-rolling process was performed at temperatures above that necessary to cause any strain-induced phase transformations. References [76] - [84] detail research investigating the phase transformations in austenitic stainless steel. Much of the understanding of the be-

haviour of austenitic stainless steels can be applied either directly or indirectly to TRIP steels which are initially austenitic.

Studies evaluating the behaviour of Fe-Mn and Fe-Mn-Cr alloys have been conducted in parallel with those involving the conventional austenitic stainless steels (AISI 300 series materials) [85] - [92]. It is possible to develop an austenitic microstructure in the Fe-Mn-Cr system and attempts were made to develop austenitic stainless steels from this base alloy system. Technically, the Fe-Mn-Cr steels are not TRIP steels, but they do transform from face-centered cubic to hexagonally close-packed to body-centered cubic (or body-centered tetragonal depending on the carbon concentration of the strain-induced martensite). The phase transformation can be triggered by lowering the temperature below the martensite start temperatures, referred to here as them M^s temperature. The same transformation sequence is exhibited when the material is mechanically strained provided that the phase stabilities are adjusted properly through control of the alloy chemistry.

2.4.2 Structural Characteristics of TRIP Steels

Figure 2.1 compares the tensile properties of high-strength and low-strength variants of TRIP steels (referred to here as Type I and Type II respectively) with those of structural steels (bridges, civil engineering applications) and the high strength low alloy (HSLA) steels (aircraft landing gear, high stress applications). While the strongest TRIP steels compare favourably with the HSLA steels with regards to strength, the ductility values and energy absorption capacities of the TRIP steels are higher than those offered by the HSLA steels. Figure 2.2 compares representative stress-strain curves for the TRIP steels as compared to the HSLA steels and structural steels and figure 2.3 compares the stress-strain curves for a low-strength TRIP steel and a grade 60 structural steel. The high levels of toughness exhibited by the TRIP steels are as a direct consequence of the phase transformation of the austenitic parent phase into the stronger martensitic phase.

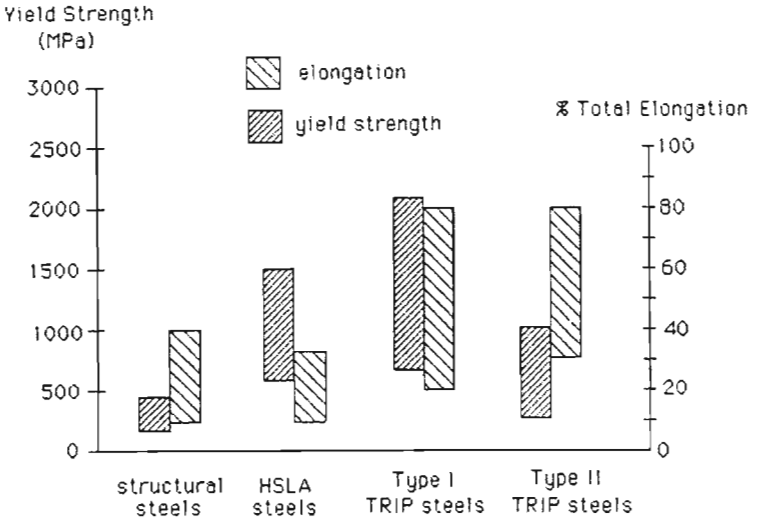

Figure 2.1: A Comparison of the Tensile Properties of Structural Steels [97].

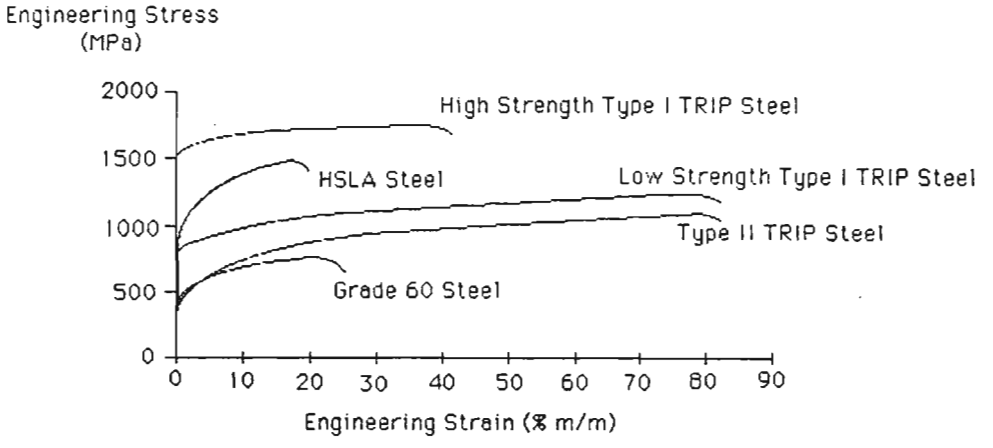

Figure 2.2: Representative Engineering Stress-Strain Curves for Structural Materials [97].

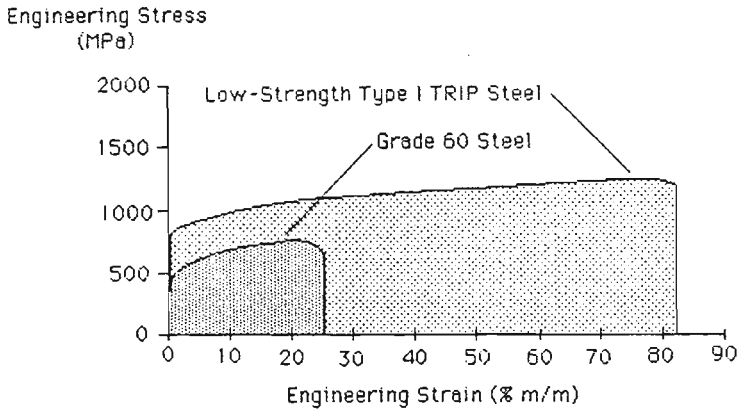

Figure 2.3: Stress-Strain Curves for a Structural Grade Steel and a Low-Strength TRIP Steel [97].

Although the Type II steels, which include the metastable Fe-Mn-Cr alloys are not apparently as strong as the Type I steels, it should be noted that these steels have not been evaluated in a condition other than the as-austenitised condition using the simplest heat treatment schemes. To obtain the highest yield strengths depicted in figure 2.1 for the Type I TRIP steels it is necessary to thermo-mechanically process the material using complicated and expensive schemes. The Type II materials were simply austenitised and either air-cooled or quenched to room temperature. The Type I TRIP steels have much lower yield strengths if not thermo-mechanically processed but still retain high levels of uniform elongation. Type I TRIP steels in this weaker condition will be referred to as Low Strength Type I TRIP steels. The lower yield strengths of the Type II TRIP steels, more typical of those in standard structural grade steels reflect the lack of thermo-mechanical processing. High strain-hardening rates and elongations have been observed in both Type I and Type II steels with ultimate tensile strength to yield strength ratios in the range of three to four being common.

The corrosion resistance of the Type II TRIP steels is superior to that of the Type I materials due to the higher levels of chromium added to their chemical formulations. In addition, both the Type I and Type II TRIP steels experience the strain-induced phase transformations responsible for delaying mechanical instability and necking

in uniaxial tensile testing, The increased uniform plastic deformation observed in these alloys corresponds to increased levels of energy absorption capacity. A direct measurement of the energy absorbing capacity of TRIP steels may be made by considering the true stress-strain curves in order to calculate the energy absorbed during fracture

$$E_v = \int_0^{\varepsilon_f} \sigma(\varepsilon)\, d\varepsilon \tag{2.1}$$

where, $\sigma(\varepsilon)$ represents the true stress expressed as a function of true strain. Energy absorption should be considered in terms of pre-neck and post-neck regimes as shown in figure 2.4. While the energy absorbed per unit volume is generally greater after the neck forms, the actual volume of material participating in the deformation process should be taken into account. TRIP steels generally display uniform elongation, i.e., non-localised deformation throughout the entire gauge length, and in so doing, the entire gauge length is contributing to energy absorption. If a mechanical instability initiates during plastic deformation any further straining is concentrated within the unstable region. This would lead to the formation of a true neck in conventional steel materials. The unstable region in a TRIP steel component however transforms from the weaker austenitic phase to the stronger martensitic phase resulting in the region becoming locally stronger than the surrounding material so that the deformation continues without the formation of a true neck. This process is repeated throughout the deforming gauge section of a tensile specimen or deforming region of a component. Many TRIP steels therefore display little localised deformation prior to failure.

Figure 2.5 shows the true stress-strain curves for a TRIP steel processed using three different treatments, the stress-strain curves for two different tempers of 4340 steel are also included. A circle on each of the respective curves shows the necking point for each test. Any further deformation beyond the necking strain is considered to be locally concentrated within the necked region of the tensile specimen gauge length. At strains below the necking strain the entire volume (either gauge or component) absorbs deformation energy whilst beyond the necking strain limit, only the neck volume absorbs energy. The true strain at necking sometimes referred to as the strain

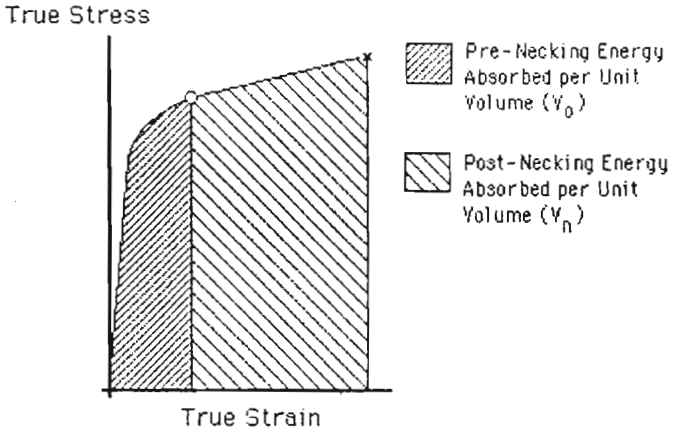

Figure 2.4: A True Stress - Strain Curve Divided into Pre and Post-Necking Regimes [94].

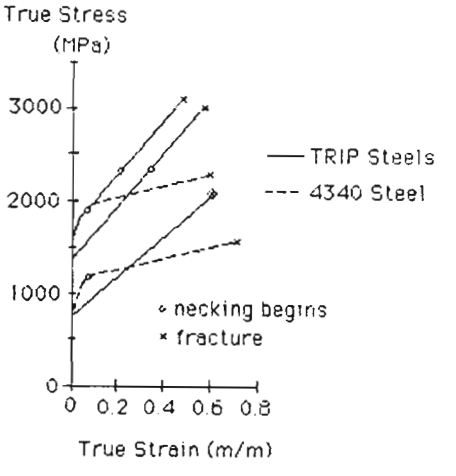

Figure 2.5: True stress-strain curves for a HSLA steel and a type I TRIP steel [55].

hardening exponent n is therefore a useful parameter in modelling the deformation response of a material. The fracture energy absorption capacity of a material is therefore directly related to the strain-hardening exponent. TRIP steels have a combination of high strength and high ductility thus accounting for their increased fracture resistance. The total fracture energy per unit volume (E_v) is the sum of energy absorbed per unit volume prior to and after necking.

$$E_v = \int_0^{\varepsilon_{uts}} \sigma(\varepsilon)\, d\varepsilon + \int_0^{\varepsilon_f} \sigma(\varepsilon)\, d\varepsilon \tag{2.2}$$

where ε_{uts} represents the true strain at ultimate tensile strength (necking) and ε_f represents the true failure strain. The total energy absorption during fracture is obtained by multiplying the respective integrals by the corresponding volumes participating in deformation before (V_0) and after (V_n) necking.

$$E_v = V_0 \int_0^{\varepsilon_{uts}} \sigma(\varepsilon)\, d\varepsilon + V_n \int_0^{\varepsilon_f} \sigma(\varepsilon)\, d\varepsilon \tag{2.3}$$

Table 2.1 compares the energy absorption characteristics of the materials for which the properties are displayed in figure 2.5 [104]. The volume of material associated with necking was assumed to be one-tenth of the total gauge length volume, i.e. $0.1V_0$. As mentioned above it is assumed that the entire gauge volume absorbs energy during the uniform plastic deformation at true strains less than the strain hardening exponent n whereas only the necking volume is absorbing energy at true strain levels greater than n. The values contained in the table indicate that the three TRIP steel variants absorbed considerably more energy during fracture than the two variants of HSLA steels. Although both types of steel can be processed to achieve a range of stress-strain behaviour as illustrated in Figure 2.3, the effectiveness in delaying necking of the deforming gauge section is readily apparent in the levels of energy absorbed. One aspect evident in the data is that the lower strength TRIP steel variant, which has a true strain at necking equal to 0.60, absorbed considerably more energy than the high-strength steels including the high strength TRIP steels. These estimates of energy absorption indicate the enhanced structural safety that could be realized through selective utilisation of TRIP steels as structural components. The additional energy absorption would be particularly beneficial in

Steel	σ_{yield}	n	E_v ($\varepsilon < n$)	E_v ($\varepsilon > n$)	E_{total}
	[MPa]		[MJ/m^3]	[MJ/m^3]	[MJ/m^3]
TRIP	760	0.60	858		858
TRIP	1400	0.35	433	56	489
TRIP	1600	0.25	395	104	499
4340	800	0.10	100	85	185
4340	1600	0.08	138	104	242

Table 2.1: Energy Absorption Characteristics for TRIP Steels and HSLA 4340 Steels

structures subjected to cyclic deformation where the energy absorption would delay structural failure thereby enhancing structural safety.

In addition to the studies mentioned above, low-cycle and high-cycle fatigue properties of TRIP steels have also been investigated [40], [55]. The energy absorption capability of TRIP steels results in reduced rates of fatigue crack growth thereby delaying ultimate failure. Figure 2.7 shows the fatigue results for TRIP steels as compared with those of conventionally melted 4340, electro-slag re-melted (ESR) 4340, high-strength alloy 300M (currently used in aircraft landing gear applications) and high performance alloy HP 9-4. The ultimate tensile strengths and fatigue endurance limits for 107 cycles are plotted for fatigue tests with a minimum to maximum load ratio, R, of 0.1. The TRIP steels displayed good fatigue properties particularly in the higher strength materials where the combination of tensile strength and fatigue endurance limits are superior to those of the other materials.

2.4.3 Strain Memory Alloys as Smart Materials

SMART structures and materials development has become an important research area. Systems are being developed to adapt to given loading conditions to increase operational performance e.g. to flex an aircraft wing so as to produce more lift. Smart materials encompass a very broad range of materials which on the one hand can be manipulated under given input conditions or which have the inherent ability

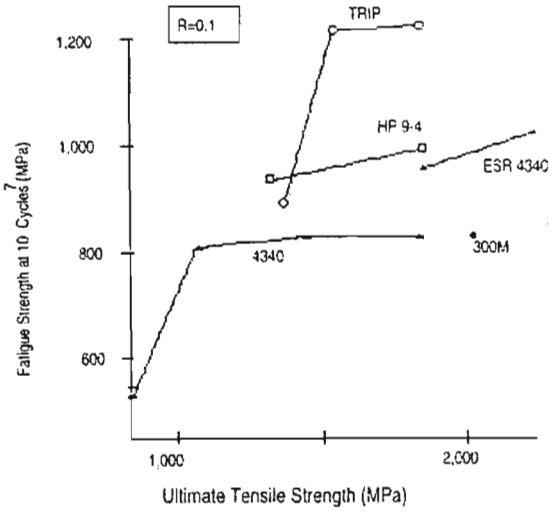

Figure 2.6: High Cycle Fatigue Properties of a TRIP Steel and High Performance Structural Steels [55].

to indicate the amount of deformation. The damage indicating materials fall into two classes; materials which are composites of normal structural material and sensors to obtain feedback which will be referred to as class II smart materials, and those which contain an inherent feature that changes with deformation and therefore can be used as a damage indicator. These latter materials will be referred to as class I smart materials.

The TRIP steels fall into the class I category. Some of the alloys being investigated for sensor element applications are simply metastable such as the austenitic stainless steels and are not truly TRIP steels, they are also however categorised as class I smart materials since the metastable alloys can be formulated in such a way as to produce measurable changes in ferromagnetic response as a function of applied strain. Although the ferromagnetic response increases markedly as the amount or volume fraction of strain induced martensite increases, instrumentation is needed to interrogate the material in order to obtain the ferromagnetic response, and ultimately correlate the response with the amount of strain required to produce the corresponding degree of phase transition.

The inherent advantage of a class I smart material over a class II smart material is

that the material can act a both structure and sensor simultaneously without any need for the attachment of sensors. In addition the class I smart materials will retain information useful in assessing damage regardless of events such as power loss etc. This is an advantage when it comes to damage assessment and in the utilisation of passive monitoring systems for infrastructural concerns. Cost is reduced with the ease of measurement and correlation with damage being relatively straightforward.

The sensor element geometry can also be adjusted to control the amount of sensor material which actually deforms in response to structural loading. For example it is possible to increase the attachment distance on a structure while decreasing the gauge length of the sensor element to gain a mechanical advantage. The effect magnification makes it possible to accurately measure small strains. It has been demonstrated that strain levels as low as 50 microstrain may be measured using a strip sensor element [103].

2.5 Feasibility of Metastable Alloys as Deformation Sensing Materials

2.5.1 Characteristics of Metastable Alloy Sensors

As mentioned above, the strain-induced phase transformation exhibited by TRIP steels has been recognised as a candidate mechanism for detecting and monitoring strain in mechanical components. The product martensitic phase is ferromagnetic due to the body-centered structure whereas the parent austenitic phase is paramagnetic (due to its face-centered cubic structure) with no significant ferromagnetic response. It is therefore possible to monitor the extent of deformation in a metastable sensor material using a transformation calibration curve for the particular strain-sensing alloy. The transformation behaviour depends on the chemical composition and it is possible, through tailoring the sensor alloy chemistry, to produce different transformation rates and transformation strain ranges depending on the type of ap-

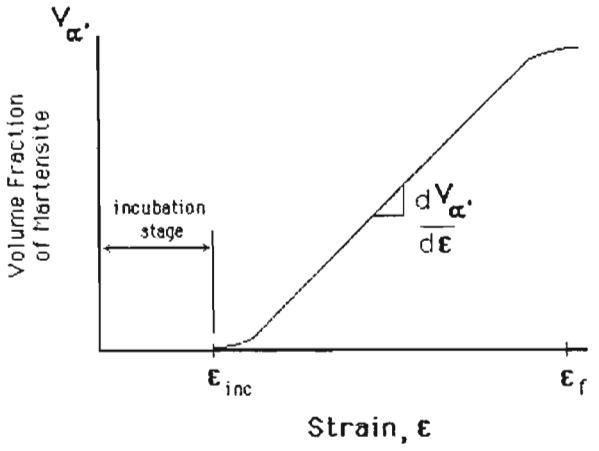

Figure 2.7: Generic strain-induced martensitic phase transformation curve.

plication being considered and the specific monitoring requirements desired. Several researchers have been engaged in the development of structural health monitoring systems based on this fundamental approach over the last few years [93] - [104].

Figure 2.7 shows a generic transformation curve for a metastable sensor alloy. The incubation strain corresponds to the initiation of the strain-induced transformation and is therefore the lowest measurable strain. It is possible to adjust or eliminate the incubation strain and likewise, the martensitic transformation rate, which controls the sensitivity and range of the sensor material response, can be increased or decreased depending on the monitoring strain range desired and the sensitivity required. Steep transformation rates are desirable for many structural applications where the TRIP steel would be used as both the structural component material and the sensor, for example aircraft fasteners such as bolts where little deformation is generally acceptable before repairs are required. Incubation strains equal to or close to zero would also be required to provide an indication of an impending structural deformation problem as soon as possible. This approach, in which a deforming structural component is monitored over a certain time period is possible only where some structural instability is tolerable in the design.

For sensor element applications the advantage of TRIP steels lies in the fact that the shape of the transformation curve can be controlled and the level of incubation

strain which triggers the transformation can be modified. The sensor material can be adjusted to produce the optimised transformation behaviour depending on the application. Once thermo-mechanically processed to produce the required metastable, austenitic microstructure, the TRIP steels inherently possess the damage detecting and monitoring capacity by producing the ferromagnetic, martensitic product phase. The austenite is paramagnetic and, therefore, does not display a significant ferromagnetic response. The magnetic susceptibility changes by a factor of approximately five orders of magnitude between purely paramagnetic austenite and a 100% ferromagnetic martensite. Thus, the detection of small amounts of martensite (of the order of less than one volume percent) is relatively simple using off-the-shelf detectors based either on the Hall effect or on inductance readings. This aspect of the TRIP steels makes them an inherently SMART material.

Although as mentioned above it is possible to alter chemistry to change and control the transformation behaviour, it is also possible to affect the transformation by altering the thermo-mechanical processing history of the material as shown in figure 2.8. In this case a TRIP steel was warm rolled at 450° C to introduce a 0, 20, 40, 60 or 80% (/0, /1, /2, /3, /4, respectively) austenitic fraction. The austenite does not transform at 450° C, but the dislocation density does increase with larger strains thus the higher yield strengths as the extent of warm-rolling is increased. Specimens A15/1 and A15/3 were not taken to failure whereas the remaining specimens were. Note that the transformation curves tend to become sharper indicating higher transformation rates with increasing initial deformation. Engineering component materials can therefore be chosen based on the strength required plus the specific transformation behaviour which would yield the optimum monitoring data for the intended application consistent with the strain sensitivity and range desired. The prior deformation of austenite increases the martensite nucleation site density thereby increasing the rate of martensite formation as a function of applied strain. A lower amount of initial austenite deformation is desired if relatively lower strengths and high service strains are tolerable in the component design. Higher strengths are also achievable, but at a decrease in total strain range over which the

transformation occurs, i.e., the range over which strains can be monitored once the initiation of structural instability has occurred (consistent with the lower levels of tolerable strain for most high-strength bolt applications). The transformation rates are highest in the early stages of martensite formation therefore making it possible to pre-strain the material to a level where any further deformation will cause a rapid increase in the rate of martensite formation and a corresponding marked increase in ferromagnetic response. Pre-straining thus provides an additional variable in fastener alloy thermo-mechanical processing which can he utilised to decrease any incubation strain effect that is unwanted in a specific application.

Figure 2.8 shows the stress-strain curves for a TRIP steel warm rolled at 450° C to varying extents along with the Hall output voltages from an attached Hall sensor. A wide range of yield strengths can be achieved utilizing the warm rolling as a process variable. A/15-3 and A/15-1 were not tested to failure whereas the remaining specimens were. The incubation strain is excessively large for the warm rolled materials, therefore in order to optimise the alloys for structural applications either a pre-straining (cold-working treatment) would be required to eliminate the incubation strain or the alloy chemistry could be adjusted to destabilise the austenitic phase with respect to applied strain. These curves illustrate the range of properties that can be achieved through the thermo-mechanical processing options available. Although the warm rolling does increase the material fabrication costs, the additional cost may be offset by the amount of material required to support the design stresses considering the increased strength of the TRIP steels.

The high strength TRIP steel compositions, if thermo-mechanically processed to achieve high strengths, are not weldable since welding would alter the microstructure and hence result in weak material in the heat-affected region of the weld. Design considerations would have to anticipate this constraint, perhaps by employing bolted connections as opposed to welded connections. Some designs can easily be modified or reconfigured to accommodate this constraint. The lower strength TRIP steels, particularly the Type II materials, should be weldable based on their compositions and the fact that warm rolling is not employed. The Type II materials can also

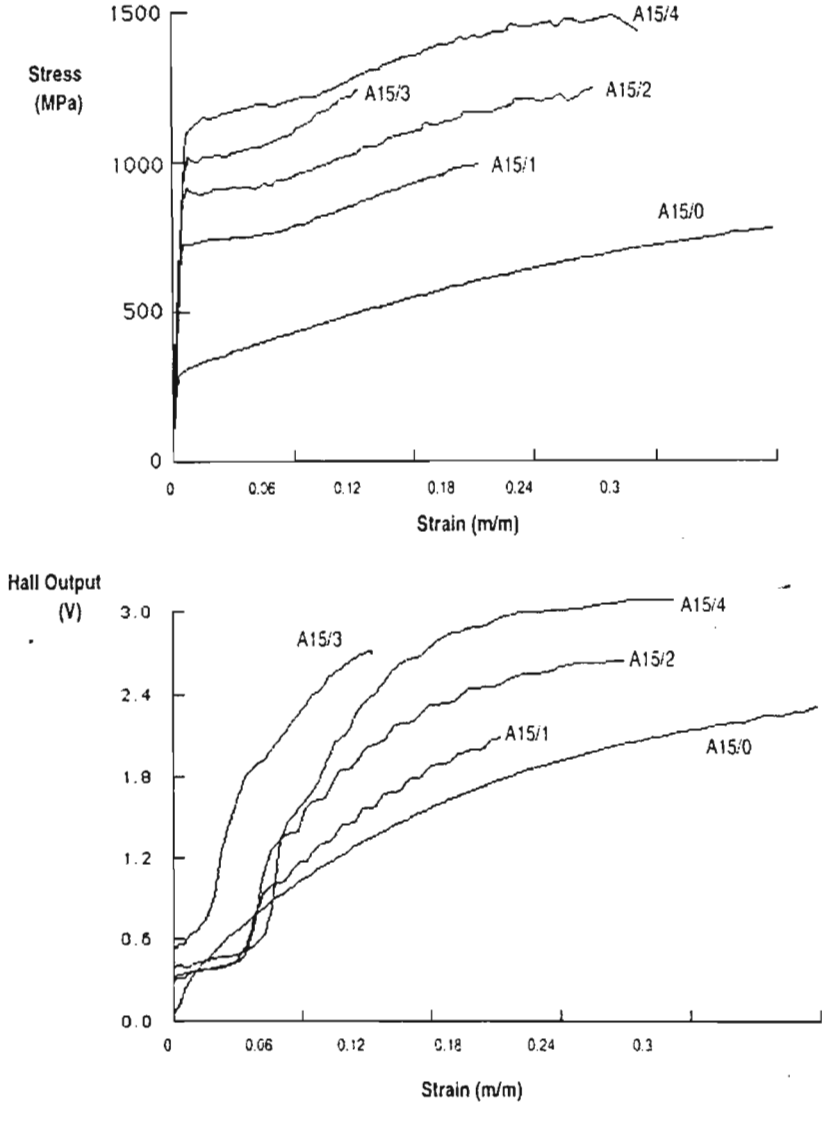

Figure 2.8: Stress-strain curves (top) and Hall output-strain curves (bottom) for Fe-8.4Cr-8.4Ni-2.1mn-0.262C TRIP sensor material [101]

be prepared as fully stainless materials with corrosion resistance levels typical of austenitic stainless steels.

2.5.2 The Ferromagnetic Response of Strain Memory Alloy Sensors

There are three primary issues associated with the use of metastable alloy sensors in structural deformation sensing and monitoring. The first involves the inhomogeneity of the phase transformation, the second involves the temperature dependence of the transformation process and the third and last involves strain rate effect on transformation behaviour.

As mentioned previously, metastable alloys deform inhomogeneously during the initial stages of plastic deformation [52]. The measurement technique, i.e., the methodology of obtaining the ferromagnetic response from a sensor element designed to have a measurable gauge length over which the reading is taken, will determine how extensively any inhomogeneous deformation will affect the measured value. A ferromagnetic sensor, such as a Hall sensor, which measures the localized ferromagnetic response of the sensor element in the location where the Hall sensor is positioned will produce a localised rather than overall measurement. Measurement of the ferromagnetic response using an induction coil arrangement will produce a reading which reflects the overall behaviour of the deforming gauge length. Using this latter approach the reading is then an averaged response which takes into account the deformation occurring within the entire gauge length of the sensor element.

With regard to temperature effects, the phase transformation from the metastable, austenitic parent phase to the thermodynamically stable, martensitic product phase occurs due to the Gibb's free energy change that occurs when the transformation proceeds, which varies as a function of the deformation temperature. Experiments have show that more martensite forms as the deformation temperature decreases in agreement with the behaviour documented by TRIP steel researchers. Figure

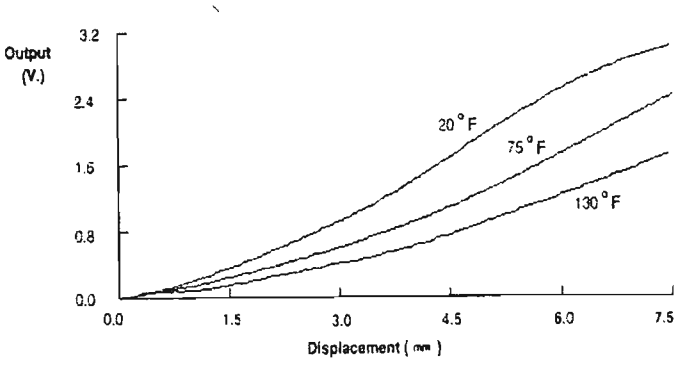

Figure 2.9: Hall unit output as a function of displacement for a candidate sensor material [100].

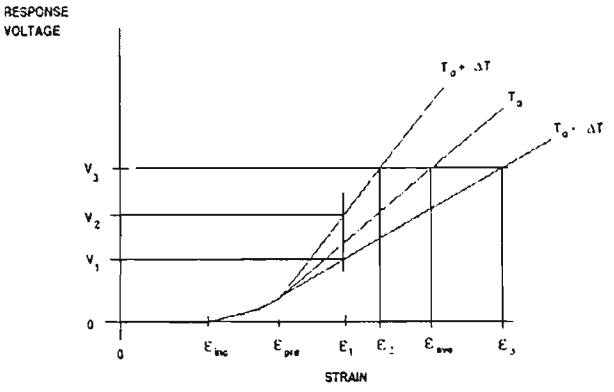

Figure 2.10: Idealized behaviour of an installed sensor element in a bridge monitoring system [100].

2.9 shows the temperature variation of the response of a metastable sensor alloy based on a carbon free version of an austenitic stainless steel, a material known to transform similarly to TRIP steels.

The temperature dependence of the response does affect the overall performance level of a passive monitoring system. The primary affect is to increase the error bands associated with a particular reading that might have been obtained for a particular sensor. The error introduced by the temperature dependence increases as the amount of martensite formed increases. This can be appreciated by considering the idealised diagram shown in figure 2.10.

When the sensor is installed the element is pre-strained to produce the ε_{pre} shown on the curve (where $\varepsilon_{pre} > \varepsilon_{inc}$). A set point reading is then established which is the baseline reading for that sensor element. Any deformation, i.e., further plastic straining of the element, will increase the amount of martensite beyond the initially measured level. The amount of additional martensite would then depend on the deformation temperature at which it was formed. If the additional strain produced a total strain of ε_1 then the corresponding ferromagnetic response reading, presented here in terms of measured voltage, would lie between V_1 and V_2. From the sensor point of view, one would measure a particular voltage, say V_3, which would then correspond to an additional straining of between (ε_2 - ε_{pre}) and (ε_3 - ε_{pre}) depending on the temperature at which the additional straining occurred. It is possible to obtain an estimate of the actual strain by assuming that the deformation occurred at the average temperature during the time between the last inspection and the current inspection. In this case the average temperature is assumed to be the same as the sensor installation temperature, T_0. The error bars on the strain measurement would then extend between ε_2 and ε_3. For illustration purposes V_3 was chosen to correspond to a considerable proportion of martensite formed. Note that if the measured voltage was near the set point voltage, V_0, say at the V_1 level, then the error bars are far smaller. In certain applications it may be possible to change the operating mode to a semi-active mode, for example a thermistor and data acquisition chip may be installed on conjunction with a particular sensor or sensor array so that changes are stored as a function of time along with the temperature when the deformation occurred.

Variations in ferromagnetic response due to the instrumentation and variances that might exist in the sensor elements themselves are lumped together to produce what is termed the error related to the sensor system. The utilisation of inductance measurements rather than Hall sensor measurements will produce less variability in the output. Likewise, careful fabrication of sensor elements so as to produce consistent sensors will reduce the variability within the sensor elements themselves, thus quality control of the sensor element manufacturing becomes of extreme importance in

reducing variability.

The optimum solution to the temperature dependence issue is to identify alloy compositions with little or no temperature dependence. This is a difficult problem considering that thermodynamics control the transformation rate. The problem is equivalent to finding alloys where there is little change in the martensite free energy over the range of temperatures appropriate for the monitoring application. The Fe-Mn-Cr alloy systems are attractive in this case since the intermediate phase, ε (epsilon) martensite forms prior to the formation of the stable, ferromagnetic, α' (alpha prime) martensite. The ε martensite forms as intersecting bands parallel to the $\{1\ 1\ 1\}$ planes in the austenite. Considering that α' martensite nucleates at ε martensite band intersections, it is possible to control the number of effective α' martensite nucleation by controlling the ε band intersection density within the austenite. The amount of α' martensite that can form is then constant regardless of temperature assuming that the lowest temperature of service is above the temperature where the precursor ε bands are formed.

Another approach to reducing the temperature sensitivity of the transformation process involves producing a dislocation substructure by deforming the strain memory alloy at a temperature below the lowest service temperature. The substructure will be consistent with the low temperature where the deformation was applied and assuming that the initial deformation strain is small the alloy will contain a density of α' martensite nucleation sites which should be greater than would be produced at a higher temperature. Considering that the range of expected service temperatures would be higher than the pre-deformation temperature, the amount of α' martensite that forms during service should be relatively constant reflecting the initial distribution of nucleation sites formed prior to installation of the sensor. In effect, the sensor material will behave as though it was being loaded at the pre-deformation temperature as long as the actual temperature is higher than the pre-deformation temperature.

The final issue involves the effect of the strain rate on the phase transformation

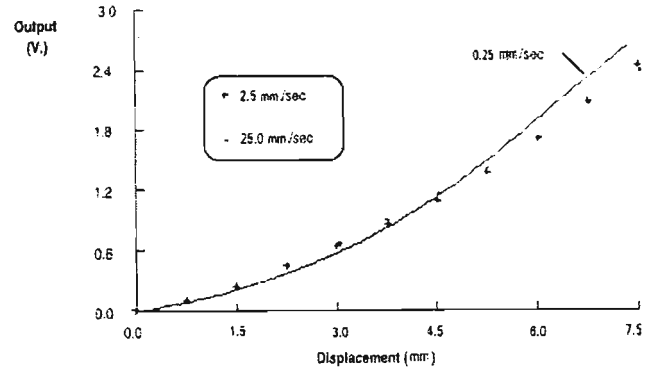

Figure 2.11: Hall Unit Output as a Function of Displacement for Three Different Strain Rates [100].

behaviour. It has been determined empirically that sensor alloys which are based on carbon-free chemical formulations do not display strain rate effects that are considered to be large enough to present a problem. Within the strain rates considered typical for the accumulation of damage in conventional structures carbon-free alloys display virtually no strain rate effects as shown by the data in Figure 2.11.

Alloys which contain carbon as a principal alloying element e.g. the high strength TRIP steel formulations, display a strong strain rate effect with more a$\not{c}$ martensite forming at lower strain rates and also tend to display discontinuities whereby the curves contain steps where the strain would increase a small amount with no increase in response voltage as measured with a Hall sensor. These steps correspond to the inhomogeneous deformation along the gauge length of the element as cited earlier. The reading beneath the Hall sensor will increase when the transformation occurs in that particular region. As more and more martensite forms, that region of the gauge length eventually becomes stronger than other regions at which point the other regions deform preferentially. For small strains, generally less than 2%, no change will occur under the Hall sensor. Once the gauge length has strengthened throughout, the region under the Hall sensor will again transform. Any further deformation occurs uniformly throughout the entire gauge length. This is of course undesirable for sensor element applications so research has concentrated on alloy

design efforts for sensor element applications along the lines of carbon-free alloy compositions to avoid these problems.

Chapter 3

Response Modelling using the Finite Element Method

3.1 Introduction

The finite element method is a numerical analysis technique for obtaining approximate solutions to engineering problems. Although it was originally developed to study the stresses in complex airframes, it has since been extended and applied to continuum mechanics. It is in general necessary to obtain approximate numerical solutions to engineering problems rather than analytical solutions. The governing equations and boundary conditions of these problems may be readily available, however there is usually no simple analytical solution to these problems. The difficulty, for example may arise as a result of a complex geometry or some other features of the problem which is either irregular or complicated. One possibility is to make some simplifying assumptions that make the problem easier to solve. In some cases, this may be acceptable, however, this approach may result in serious inaccuracies or incorrect answers. An alternative approach is to maintain the complexity of the problem and employ an approximate solution using a numerical technique. Several approximate numerical analysis methods have been developed. One of the most

commonly used methods is the general finite difference scheme [105], [106]. The finite difference model of a problem gives a pointwise approximation to governing equations which is improved as more points are included. This method may be used to solve fairly difficult problems.

If irregular geometries or unusual boundary conditions are considered, the finite difference techniques become difficult to implement. The finite element method overcomes these limitations by considering the solution region in terms of many discrete, interconnected sub-domains or elements. A finite element model of a problem therefore provides a piecewise approximation to the governing equations. The elements can be assembled together in many ways to cover the solution domain, even for very complex geometries.

3.2 The Concept of the Finite Element Method

The finite element discretisation procedures reduce the problem to one of a finite number of unknowns by dividing the solution region into elements and the final solution is defined in terms of assumed approximating functions for each element. The approximating functions are defined at specified locations termed nodal points. Nodes are usually placed on the element boundaries. In addition to boundary nodes an element may also have interior nodes. For the finite element representation of a problem, the nodal values of the field variables become the new unknowns. The degree of approximation depends on the size and number of the elements as well as on the interpolation functions selected. The functions cannot be chosen arbitrarily, because special conditions should be satisfied. The functions are usually chosen so that the field variable or its derivatives are continuous across adjoining element boundaries. An important advantage of the finite element method is its ability to formulate expressions for individual elements before assembling them together to model the entire problem. The steps listed below are useful in explaining how the finite element method is used [107].

1. Discretise the continuum. The fist step is to divide the continuum or solution region into elements. It is not only desirable but also may be necessary to use different types of elements in the same solution. The number and the types of elements to be used in a given problem are matters of engineering judgment.

2. Select interpolation functions. The next step is to assign nodes to each element and then choose the type of interpolation function to represent the variation of the field variable over the element. Polynomials are usually selected as interpolation functions for the field variable, since they are easily integrated and differentiated.

3. Find the element properties. Once the finite element model has been established (the elements and interpolation functions have been selected) the matrix equations are determined to express the properties of the individual elements.

4. Assemble the element properties to obtain the system equations. The matrix equations are combined to express the behaviour of the elements and formed to express the behaviour of the entire solution system.

5. Solve the system equations.

One of the main advantages of the finite element method is that the method can handle irregular geometries routinely which is useful considering that closed-form solutions are not generally available for irregular geometries. The flexibility with regard to node spacing and the size and shape of the elements can be used to create highly irregular geometric forms. Triangular elements are particularly flexible in this respect, while rectangular elements can be simpler in other cases. As the element size can be varied, areas of steep stress gradients can be approximated in accurate detail. Another advantage of the finite element method over analytical solution techniques is its ability to handle non-homogeneous and anisotropic materials. There is little extra effort involved in the finite element formulation when these types of materials are modelled. Any type of external load can be considered. Distributed loads are replaced by equivalent concentrated nodal point loads. The choice of boundary

conditions is variable and it is possible to examine the effects of nonlinear properties of materials. Examples include the simulation of plasticity [108], complex buckling [109] and vibration problems [110], as well as crack and fatigue effects [110].

3.3 A Brief History of The Finite Element Method

The finite element method was developed simultaneously in the fields of applied mathematics and engineering. The first study to use piecewise continuous functions defined over triangular domains appears in the applied mathematics literature with the work of Courant [111] in 1943, who, by extension of Euler's [112] work, used an assemblage of triangular elements and the principle of minimum potential energy to study the St. Venant torsion problem. Polya [113], [114], Hersch [115] and Weinberger [116], [117] worked on finding bounds on eigenvalues using this method. In 1959, Grenestadt [118], using principles described by Morse and Feshback [119], developed an approach involving cells instead of points, dividing the solution domain into sub-domains. In his theory, he describes a procedure for representing the unknown functions by a series of functions. Using continuity requirements, continuous problem are then discretised. This theory allows for irregularly shaped cell meshes and contains many of the essential and fundamental ideas of finite elements. White [120] and Friedrichs [121] used triangularly shaped elements, in regular meshes, to develop difference equations from variational principles. Numerous studies concerning discretisation errors, rates of convergence and stability for different types of finite element approximations have appeared in the literature. The finite element method has also been extensively applied to the solution of nonlinear problems [144]. Mathematical literature on the finite element method has increased considerably since 1970. A survey paper by Oden [158] in 1972 summarizes some of the important mathematical contributions.

The earliest study in the engineering literature appears to be that of Hrenikoff [159], who assumed a continuum structure to be divided into elements or structural

sections. McHenry [160] in 1943 and Newmark [161] in 1949 further developed this concept of discretisation. Argyris and collaborators published a series of papers on linear structural analysis and efficient solution techniques suited for automatic digital computation. In 1956, Turner, Clough, Martin and Topp [169] published a paper on the solution of plane stress problems by means of triangular elements whose properties were determined from the equations of elasticity theory. This study introduced the direct stiffness method for determining finite element properties. A further study on the plane elasticity problem was presented by Clough [170]. Besseling [171], Melosh [172], Fraeijs de Veubeke [173] and Jones [174] recognized that the finite element method was a form of the Ritz method and confirmed it as a general technique to handle elastic continuum problems. Zienkiewicz and Cheung [175] reported that the finite element method is applicable to all field problems which can be put into variational form. Numerous papers may be found in the literature, dealing with all aspects of the finite element method and its applications to areas such as static and dynamic structural analysis, fluid flow, heat transfer and magnetostatics.

3.4 Theoretical Formulation

3.4.1 Continuum Problems

In the continuum or Eulerian approach, all processes are characterised by field quantities that are defined at every point in space. The independent variables in continuum problems are the coordinates of space and time. Continuum problems are concerned with fields of temperature, stress, mass concentration, displacement, electromagnetic and acoustic potentials, etc. These problems arise from the phenomena that are approximately characterised by partial differential equations and their boundary conditions.

Continuum problems of mathematical physics are often referred to as boundary

value problems because their solution is sought in some domain defined by a given boundary, on which certain conditions termed boundary conditions are specified. The boundary is said to be closed if conditions affecting the solution of the problem are specified everywhere on the boundary and open if part of the boundary extends to infinity and no boundary conditions are specified on the part at infinity [176].

3.4.2 Problem Statement

Consider some domain Ω bounded by the surface Γ . Let ϕ be a scalar function defined in the interior of Ω such that the behaviour of ϕ is given by

$$L(\phi) - f = 0 \tag{3.1}$$

where f is a known scalar function of the independent variables and L is a linear or nonlinear differential operator. It is assumed that the physical parameters in the differential operator are known constants or functions. In n dimensions, second-order differential operators can usually be reduced, by a suitable transformation, to the form

$$L(\phi) = \sum_{i=1}^{n} A_i \frac{\partial^2(\phi)}{\partial x_i^2} + \sum_{i=1}^{n} B_i \frac{\partial(\phi)}{\partial x_i} + (\phi)C + D \tag{3.2}$$

where coefficients A_i, B_i and C and the term D may be functions. The operator as given in equation (3.2) is linear if A_i, B_i, C and D are functions only of the independent variables $(x_1, x_2, x_3, ..., x_n)$, and quasilinear if A_i, B_i, C and D are functions of x_i; and the dependent parameter, as well as first derivatives of the dependent parameter. An operator is linear only if

$$L(f + g) = L(f) + L(g) \tag{3.3}$$

The general definition of the operator $L(\phi)$ in equation (3.1) precludes a discussion of appropriate boundary conditions. However, without boundary conditions, equation (3.1) does not describe a specific problem. From equation (3.1), it is seen that the general problem is to determine the unknown function ϕ that satisfies equation (3.1) and the associated boundary conditions specified on Γ. There are many alternative

approaches to the solution of linear and nonlinear boundary value problems and they range from completely analytical to completely numerical, here the application of the variational approach will be discussed with direct reference to the finite element method.

3.4.3 The Variational Approach

Often continuum problems have different, but equivalent, differential and variational formulations. In the differential equation formulation, the problem involves the integration of a differential equation or a system of differential equations subject to given boundary conditions. In the classical variational formulation, the problem is to find the unknown function or functions that make stationary a functional such as $I(\phi)$ or a system of functionals subject to the same boundary conditions. The two problem formulations are equivalent because the functions which satisfy the differential equations and their boundary conditions also extremise or make stationary the functionals. The classical variational formulation of a continuum problem often has advantages over the differential equation formulation from the viewpoint of obtaining an approximate solution.

Firstly, the functional, which may actually represent some physical quantity in the problem, contains derivatives of order lower than that of the differential operator and an approximate solution can be sought in a larger class of functions. Secondly, the problem may possess reciprocal variational formulations, that is, one functional must be minimized and another one of a different form must be maximized. Thirdly, the variational formulation allows us to treat very complicated boundary conditions as natural boundary conditions and fourth, from a mathematical viewpoint the variational formulation is helpful because it can sometimes be used to prove the existence of a solution by using calculus of variations. If the variational approach is to be used, a variational statement for the continuum problem must be formulated, which implies that the problem must be posed in a variational form.

Historically, variational methods are among the oldest means of obtaining solutions to problems in physics and engineering. One general method for obtaining approximate solutions to problems expressed in variational form is known as the Ritz method. This method is basically a forerunner of the finite element procedure. The finite element method is in fact a special case of the Ritz method in which the interpolation functions satisfy certain continuity requirements.

The Ritz Method

The Ritz method consists of assuming the form of the unknown solution in terms of known or trial functions with unknown adjustable parameters. The trial functions are also termed coordinate functions. The procedure involves substitution of the trial functions into the functional and thereby expressing the functional in terms of the adjustable parameters. The functional is then differentiated with respect to each parameter and the resulting equation is set equal to zero. If there are n unknown parameters, there will be n simultaneous equations to be solved for these parameters. The accuracy of the approximate solution depends on the choice of trial functions. The trial functions are defined over the whole solution domain and they satisfy at least some and usually all of the boundary conditions. If the exact solution is contained in the family of trial solutions, the Ritz procedure gives the exact solution. Generally, the approximation improves as the size of the family of trial functions and the number of adjustable parameters increase. The process of including more and more trial functions leads to a series of approximate solutions which converges to the true solution. Often a family of trial functions is constructed from polynomials of successively increasing degree, but in certain cases other kinds of functions may also offer advantages [177].

Relation of the finite element method to the Ritz Method

The finite element method and the Ritz method are essentially equivalent. Each method uses a set of trial functions as the starting point for obtaining an approximate solution; both methods employ linear combinations of these trial functions and both models seek the combination of the trial functions that makes a given functional stationary. The major difference between the methods is that the assumed trial functions in the finite element method are not defined over the whole solution domain and they have to satisfy no boundary conditions but only certain continuity conditions. Because the Ritz method uses functions defined over the whole domain, it can be used only for domains of relatively simple geometric shape. In the finite element method the same geometric limitations exist, but only for the elements. Due to the fact that elements with simple shapes can be assembled to represent quite complex geometries, the finite element is more versatile and flexible than the Ritz method.

Generalisation of the definition of an element

The mathematical interpretation of the finite element requires the generalisation of the definition of an element in less physical terms. Essentially elements are defined as regions of space where a field variable exists, the elements are interconnected only at nodal points located at the boundaries or surfaces of the elements. The nodes of an element are generally located in space where the field variable and possibility its derivatives are known or sought. The mathematical interpretation of a finite element mesh is that it is a spatial subdivision rather than a material subdivision [178]. Once the element mesh for the solution domain has been established, the behaviour of the unknown field variable over each element is approximated by continuous functions expressed in terms of the nodal values of its derivatives up to a certain degree. The functions defined over each finite element are termed interpolation functions, shape functions, or field variable models. The collection of the interpolation functions for the whole solution domain provides a piecewise approximation to the field variable.

The development of element equations using the Variational Principle

The finite element solution to the problem involves determining the nodal values of the field variable ϕ so as to make the functional $I(\phi)$ stationary. To make $I(\phi)$ stationary with respect to the nodal values of ϕ, it is required that

$$\partial I(\phi) = \sum_{i=1}^{n} \frac{\partial I}{\partial \phi_i} \delta\phi_i = 0 \tag{3.4}$$

where n is the total number of discrete values of field variable, ϕ_i, assigned to the solution domain. Since the terms $\delta\phi_i$ are independent, equation (3.4) can be satisfied only if

$$\frac{\partial I}{\partial \phi_i} = 0, \qquad i = 1, 2, ..., n \tag{3.5}$$

The functional $I(\phi)$ may be written as a sum of individual functionals defined for all elements within the solution domain, that is,

$$I(\phi) = \sum_{e=1}^{M} I^{(e)}(\phi^{(e)}) \tag{3.6}$$

where M is the total number of elements and the superscript (e) denotes an element. From equation (3.6), it follows that

$$\delta I = \sum_{e=1}^{M} \delta I^{(e)} = 0 \tag{3.7}$$

where the variation of $I^{(e)}$ is taken only with respect to the nodal values associated with the element (e). Equation (3.7) implies that

$$\frac{\partial I^{(e)}}{\partial \phi} = \frac{\partial I}{\partial \phi_j} = 0, \; j = 1, 2, ..., r \tag{3.8}$$

where r is the number of nodes assigned to element (e). Equation (3.8) comprises a system of r equations that characterize the behavior of element (e). Equation (3.8) for element (e) can always be written as [179]

$$\frac{\partial I^{(e)}}{\partial \phi} = \mathbf{K}^{(e)}\phi^{(e)} - \mathbf{F}^{(e)} = \mathbf{0} \tag{3.9}$$

where $\mathbf{K}^{(e)}$ is a square matrix of constant coefficients, $\phi^{(e)}$ is the column vector containing nodal values of the field variable and $\{F\}$ is the vector of resultant nodal

actions. Symbolically, the complete set of equations can be written as

$$\frac{\partial I}{\partial \phi_i} = \sum_{e=1}^{M} \frac{\partial I^{(e)}}{\partial \phi_i} = 0, \quad i = 1, 2, ..., n \tag{3.10}$$

or

$$\{\frac{\partial I}{\partial \phi}\} = \{0\} \tag{3.11}$$

The problem is solved when the set of n equations (3.10) is solved simultaneously for the n nodal values of ϕ. If there are q nodes in the solution domain where ϕ is specified by boundary conditions, there will be $n - q$ equations to be solved for the $n - q$ unknowns.

Requirements for the interpolation functions

Approximate solutions converge to the correct solution where an increasing number of elements are used, that is, when the element mesh is refined. Mathematical proofs of convergence assume that the process of mesh refinement occurs in a regular fashion, defined by three conditions [180].

1. The elements must be made smaller in such a way that every point of the solution domain can always be within an element, regardless of how small the element may be;

2. All previous meshes must be contained in the refined meshes;

3. The form of interpolation functions must remain unchanged during the process of mesh refinement.

To guarantee monotonic convergence in the sense just described and to make the assembly of the individual equations meaningful, it is required that the interpolation functions $N^{(e)}$ in the expressions

$$\phi^{(e)} \left\lfloor N^{(e)} \right\rfloor \{\phi\}^{(e)}, \quad e = 1, 2, ..., M \tag{3.12}$$

(where $\lfloor N^{(e)} \rfloor$ is the row vector of interpolation functions that are functions of the coordinates of the nodes and $\{\phi\}^{(e)}$ is the column vector) are chosen so as to satisfy the following general requirements:

1. At element interfaces (boundaries) the field variable ϕ and any of its partial derivatives up to one order less than the highest order derivative appearing in $I(\phi)$ must be continuous.

2. All uniform states of ϕ and its partial derivatives up to one order less than the highest order derivative appearing in $I(\phi)$ should have representation in $\phi^{(e)}$ when, in the limit, the element size shrinks to zero.

These requirements were given by Felippa and Clough [180] and justified by Oliveira [181]. The first one is known as the compatibility requirement, and the second as the completeness requirement. Elements whose interpolation functions satisfy the first requirement are called compatible elements, those satisfying the second requirement, complete elements. In addition to satisfying these requirements, it is also required that the field variable representation within an element and hence the polynomial expansion for the element remain unchanged under a linear transformation from one coordinate system to another. Polynomials that exhibit this invariance property are said to possess geometric isotropy.

A standard definition and notation to express the degree of continuity of a field variable at element interfaces has been developed, if the field variable is continuous at element interfaces it is said that there is C^0 continuity. If the field variable is continuous for the first derivatives there is C^1 continuity, if the second derivatives are also continuous there is C^2 continuity and so on. The functions appearing in the element equations may contain derivatives up to $(r+1)th$ order and the compatibility and completeness requirements must be satisfied to have assurance of convergence as element size decreases. These requirements hold whether the element equations were derived using the variational method, the Galerkin method or some other method.

Polynomial Interpolation Functions

Although it is conceivable that many types of functions could serve as interpolation functions, only polynomials have received widespread use. They can be integrated or differentiated without difficulty.

One independent variable

In one dimension a general complete nth-order polynomial may be written as

$$P_n(x) = \sum_{i=0}^{T_n^{(1)}} \alpha_i x^i \tag{3.13}$$

where the number of terms in the polynomial is $T_n^{(1)} = n + 1$. For $n = 1$, $T_1^{(1)} = 2$ and

$$P_1(x) = \alpha_o + \alpha_1 x$$

for $n = 2$, $T_2^{(1)} = 3$ and

$$P_2(x) = \alpha_o + \alpha_1 x + \alpha_2 x^2$$

and so on.

Two independent variables

In two dimensions a complete nth-order polynomial may be written as

$$P_n(x, y) = \sum_{k=0}^{T_n^{(2)}} \alpha_k x^i y^j, \; i + j \leq n \tag{3.14}$$

where the number of terms in the polynomial is $T_n^{(2)} = (n + 1)(n + 2)/2$. For $n = 1$, $T_1^{(2)} = 3$ and

$$P_1(x, y) = \alpha_1 + \alpha_2 x + \alpha_3 y$$

For $n = 2$, $T_2^{(2)} = 6$ and

$$P_2(x, y) = \alpha_1 + \alpha_2 x + \alpha_3 y + \alpha_4 xy + \alpha_5 x^2 + \alpha_6 y^2$$

and so on.

Three independent variables

In three dimensions a complete nth-order polynomial may be written as

$$xP_n(x,y,z) = \sum_{l=0}^{T_n^{(3)}} \alpha_l x^i y^j z^k, \; i+j+k \leq n \tag{3.15}$$

where the number of terms in the polynomial is

$$T_n^{(3)} = \frac{(n+1)(n+2)(n+3)}{6} \tag{3.16}$$

For $n = 1$, $T_1^{(3)} = 4$ and

$$P_1(x,y,z) = \alpha_1 + \alpha_2 x + \alpha_3 y + \alpha_4 z$$

for $n = 2$, $T_2^{(3)} = 10$ and

$$P_2(x,y,z) = \alpha_1 + \alpha_2 x + \alpha_3 y + \alpha_4 z + \alpha_5 xy + \alpha_6 xz + \alpha_7 yz + \alpha_8 x^2 + \alpha_9 y^2 + \alpha_{10} z^2$$

and so on.

3.4.4 Basic Two-Dimensional Element Shapes

The continuum or solution domain of arbitrary shape can be accurately modeled by an assemblage of simple shapes. Most finite elements are geometrically simple. For one-dimensional problems with only one independent variable, the elements are line segments. The number of nodes assigned to a particular element depends on the type of nodal variables, the type of interpolation function and the degree of continuity required. For some one-dimensional problems the finite element method is the most rational approach, for example, frame analysis in solid mechanics and flow network analysis in fluid mechanics. In elasticity problems where spars are used as stiffeners, one-dimensional elements can represent the spars while being connected to other two- or three-dimensional elements that represent the rest of the elastic solid.

The three-node flat triangular element is the simplest two-dimensional element and it is generally the first and most often used basic finite element. The reason is that an assemblage of triangles can always represent a two-dimensional domain of any shape. A simple but less useful two-dimensional element is the four node rectangle

whose sides are parallel to the global coordinate system. This type of element is easy to construct automatically by computer because of its regular shape, but is not well suited for approximating curved boundaries. In addition to the simplest triangle and the rectangle, other common two-dimensional elements include the six-node triangle, and the general quadrilateral. Quadrilateral elements may be formed directly or they may be developed by combining two or four basic triangle elements. Other types of elements that are actually three-dimensional but described by only one or two independent variables are axisymmetric or ring-type elements. These elements are useful when treating problems that possess axial symmetry in cylindrical coordinates.

3.4.5 Basic Element Shape Functions for Two-Dimensional Problems

Elements for C^0 problems

The number of elements capable of satisfying C^0 continuity is infinite since nodes and degrees of freedom may be added to the elements to form ever increasing higher-order elements. In general, as the complexity of the elements is increased by adding more nodes and more degrees of freedom and using higher-order polynomials, the number of elements and total number of degrees of freedom needed to achieve a given accuracy in a given problem are less than would be required if simpler elements were used. None the less, this does not suggest that higher-order elements always be used in preference to lower order elements.

There is no general guideline for choosing the optimum element for a given problem, because the type of element that yields good accuracy with low computing time is problem dependent. For C^0 problems, elements that require polynomials of order greater than three are rarely used, since little additional accuracy is gained for the extra effort expended. If a complicated boundary is to be modeled, it is more advantageous to use a large number of simple elements than a few complex elements.

Triangular elements

A portion of the family of higher-order elements may be obtained by assigning additional external and interior nodes to triangles. Each element in this series has a sufficient number of nodes to specify a complete polynomial of the order necessary to give C^0 continuity. The compatibility, completeness and geometric isotropy requirements are satisfied.

For the three-node triangular element, the linear variation of ϕ is written as

$$\phi(x, y) = \alpha_1 + \alpha_2 x + \alpha_3 y = [1 \; x \; y]\{\alpha\} = \mathbf{P}\;\boldsymbol{\alpha} \tag{3.17}$$

and by evaluating this expression at each node, we obtain

$$\boldsymbol{\phi} = \mathbf{G}\;\boldsymbol{\alpha} \tag{3.18}$$

According to the procedure of deriving interpolation functions, this can be written as

$$\begin{aligned} \boldsymbol{\phi} &= \mathbf{P}\;\mathbf{G}^{-1}\boldsymbol{\alpha} = \mathbf{N}\;\boldsymbol{\phi} \\ \mathbf{N} &= \mathbf{P}\;\mathbf{G}^{-1} \end{aligned} \tag{3.19}$$

where the elements of $\mathbf{N}$, $N_i = L_i$ are the area coordinates for the triangle.

Rectangular elements

Interpolation functions for rectangular elements with sides parallel to the global axes are easily developed using Lagrangian interpolation concepts. After the local coordinates are defined the function may be written as

$$\phi(\xi, \eta) = N_1(\xi, \eta)\phi_1 + N_2(\xi, \eta)\phi_2 + N_3(\xi, \eta)\phi_3 + N_4(\xi, \eta)\phi_4 \tag{3.20}$$

where

$$\begin{aligned} N_1(\xi, \eta) &= L_1(\xi)L_1(\eta), \\ N_2(\xi, \eta) &= L_2(\xi)L_2(\eta), \\ &\textit{etc.} \end{aligned} \tag{3.21}$$

and the L_i are the Lagrange polynomials. Interpolation functions formed as products in this way satisfy the requirements of possessing unit value at the node for which they are defined and zero at the other nodes.

Elements for C^1 Problems

Constructing two-dimensional elements that can be used for problems requiring continuity of the field variable ϕ as well as its normal derivative $\frac{\partial \phi}{\partial n}$ along element boundaries is more complicated than constructing elements for C^0 continuity alone and only a brief treatment is given here.

The field variable ϕ and $\frac{\partial \phi}{\partial n}$ are uniquely specified along the element boundaries by the degrees of freedom assigned to the nodes along a particular boundary. According to Felippa and Clough [180], the difficulties arise from the following principles:

1. The interpolation functions must contain at least some cubic terms, because the three nodal values ϕ, $\frac{\partial \phi}{\partial x}$ and $\frac{\partial \phi}{\partial y}$ must be specified at each corner of the element.

2. For non rectangular elements C^1 continuity requires the specification of at least the six nodal values, ϕ, $\frac{\partial \phi}{\partial x}$, $\frac{\partial \phi}{\partial y}$, $\frac{\partial^2 \phi}{\partial x^2}$, $\frac{\partial^2 \phi}{\partial y^2}$ and $\frac{\partial^2 \phi}{\partial x \partial y}$. at the corner nodes. For a rectangular element with sides parallel to the global axes it is necessary to specify at the corner nodes only ϕ, $\frac{\partial \phi}{\partial x}$, $\frac{\partial \phi}{\partial y}$ and $\frac{\partial^2 \phi}{\partial x \partial y}$.

3.4.6 Discretisation of the Problem Domain

As mentioned previously, the first task in a finite element solution consists of discretising the continuum by dividing it into a series of elements. The formulation of the element that should be used depends on the problem being considered. Often only one type of element may be used to represent the continuum, however, it is often the case that the problem may require several different types of elements

to be employed. An example from solid mechanics would be an elastic body supported by pin connected bars. In this case the elastic body would be represented by three-dimensional solid elements whilst the bars would be approximated by one dimensional elements.

The most popular and versatile elements, because of the ease with which they can be assembled to fit complex geometries, are the two-dimensional triangular elements. However, although a uniform element mesh is easy to construct, it does not always provide a good representation of the continuum. In many cases more elements are used in regions where the boundary is irregular, this often results in skewing of the elements and it is important to consider that the ratio of the elements' smallest dimension to its largest dimension should be near unity. Long narrow elements should be avoided as they lead to a solution with directional bias. When solving a particular type of problem for the first time, it is generally good practice to employ convergence testing of the mesh. The process involves solving the problem a number of times using varying average mesh densities. The results will converge if the quality and density of the mesh is suitable .

3.5 Mechanical Response Modelling - The Application of the Finite Element Method to Solid Mechanics Problems

Most applications of the finite element method to solid mechanics problems employ a variational principle to derive the necessary element properties or equations. The three most commonly used variational principles are the principle of minimum potential energy, the principle of complementary energy and Reissner's principle. When the principle of minimum potential energy is used, the field variable is defined as the displacement field within each element, this approach is usually termed the displacement method or the compatibility method. When the complementary

energy method is used, the stress field is taken as the field variable, this approach is known as the force method or equilibrium method. Pian and Tong [182] tabulated these and other variational bases of the finite element method for application to problems in solid mechanics. For particular problems, one principle may be more suitable than another, but for a large class of problems the displacement method is the simplest to apply and the most widely used.

3.5.1 Formulation for Small Deformation Two-dimensional Elastic Problems

The potential energy of a two-dimensional elastic body acted upon by surface and body forces and in equilibrium can be written as

$$\begin{aligned}\Pi(u,v) = \tfrac{1}{2}\int\int_A \left(\tilde{\delta}\mathrm{B}^T\mathrm{C}\delta - 2\tilde{\delta}\mathrm{B}^T\mathrm{C}\epsilon_0\right) t dA \\ - \int\int_A \mathbf{F}\,\tilde{\delta}\, t dA - \int_{C_1} \mathbf{T}\,\tilde{\delta} dS\end{aligned} \tag{3.22}$$

where $t = t(x,y)$ is the thickness of the body and $\tilde{\delta}$ is the column matrix of the components of the displacement field measured from some datum given by

$$\tilde{\delta} = \left\{ \begin{array}{c} u(x,y) \\ v(x,y) \end{array} \right\} \tag{3.23}$$

The components of B are derived by considering the two-dimensional strain-displacement relationship,

$$\mathrm{B} = \left[\begin{array}{cc} \partial/\partial x & 0 \\ 0 & \partial/\partial y \\ \partial/\partial x & \partial/\partial y \end{array} \right]$$

The matrix C contains material stiffness coefficients consistent with the constitutive stress-strain relationship and which takes different forms according to the problem considered, ϵ_0 is the column vector of initial strains which may be due to non-uniform temperature distributions, shrink fits etc. $\mathbf{F} = [X, Y]$ are the body force components due to gravity, centrifugal action, and the like, and $\mathbf{T} = [T_x, T_y]$ are the boundary traction components acting on portion Γ_1 of the boundary; these are defined per unit length for a unit thickness.

Generally, the initial strains ε_0, body force components, $\mathbf{F}$, and boundary traction components, $\mathbf{T}$, are known quantities. At equilibrium the displacement field (u, v) in the body is such that the total system potential energy assumes a minimum value. After using a suitable variational principle, general finite element equations for the elastic continuum may be developed. First the continuum will be subdivided into elements of some shape, then the form of displacement function is assumed over each element. For the general formulation, it is not needed to specify the type of element nor the particular displacement function. Firstly the equations for the general case can be developed. Subsequently they are specialised for particular cases.

3.5.2 Displacement Interpolation Functions

If it is assumed that the area A of the problem domain Ω is divided into M discrete elements, the potential energy of the elements is the sum of the potential energies of all elements provided that the interpolation functions expressing the variation of the displacement within each element satisfy the compatibility and completeness requirements. In other words to write

$$\Pi(u, v) = \sum_{e=1}^{M} \Pi^{(e)}(u, v) \tag{3.24}$$

and to be assured of convergence as element mesh size decreases, the interpolation must satisfy the compatibility and completeness requirements. For plane stress and plane strain as well as three-dimensional elasticity problems polynomial interpolations satisfy the compatibility and completeness requirements when the polynomials contain at least a constant and a combination of linear terms.

To express $\Pi^{(e)}(u, v)$, which is the potential energy function for a single element, in terms of discrete values of displacement components, it is assumed that within each element having r nodes, the displacement field is approximately related to its nodal values by r interpolating functions $N_i(x, y)$. Thus the distributed displacement field

can be expressed as

$$\boldsymbol{\delta}^{(e)} = \left\{ \begin{array}{c} u(x,y) \\ v(x,y) \end{array} \right\}^{(e)} = \left\{ \begin{array}{c} \sum_{i=1}^{r} N_i(x,y)u_i \\ \sum_{i=1}^{r} N_i(x,y)v_i \end{array} \right\} = \left\{ \begin{array}{c} \mathbf{N}\ \mathbf{u} \\ \mathbf{N}\ \mathbf{v} \end{array} \right\}^{(e)} = \mathbf{N}\ \boldsymbol{\delta}^{(e)} \tag{3.25}$$

where $\boldsymbol{\delta}^{(e)}$ denotes the element nodal displacements.

3.5.3 Element Stiffness Equations

Since the displacement field for the element has been expressed in terms of known interpolation functions and unknown displacements, the potential energy functional will be similarly expressed. Thus for element (e), the discretised functional is

$$\Pi^{(e)}(\boldsymbol{\delta}^{(e)}) = \Pi^{(e)}(u_1, u_2, ..., u_r, v_1, v_2, ..., v_r) \tag{3.26}$$

or more explicitly

$$\begin{aligned} \Pi^{(e)}(\boldsymbol{\delta}^{(e)}) = \tfrac{1}{2} \int\int_{A^{(e)}} [\boldsymbol{\delta}^{(e)} \mathbf{B}^{T^{(e)}} \mathbf{C}^{(e)} \mathbf{B}^{(e)} \boldsymbol{\delta}^{(e)} - 2\boldsymbol{\delta}^{(e)} \mathbf{B}^{T^{(e)}} \mathbf{C}^{(e)} \boldsymbol{\varepsilon}_0{}^{(e)}] t^{(e)} dA^{(e)} \\ - \int\int_{A^{(e)}} \mathbf{F}^{(e)} \boldsymbol{\delta}^{(e)} t^{(e)} dA^{(e)} - \int_{C_1^{(e)}} \mathbf{T}^{(e)} \boldsymbol{\delta}^{(e)} dS^{(e)} \end{aligned} \tag{3.27}$$

At equilibrium, the potential energy of the system assumes a minimum value when the first variation of the functional vanishes, that is

$$\delta\Pi(u,v) = \sum_{e=1}^{M} \delta\Pi^{(e)}(u,v) = 0 \tag{3.28}$$

where

$$\delta\Pi(u,v) = \sum_{i=1}^{r} \frac{\delta\Pi^{(e)}}{\delta u_i} \delta u_i + \sum_{i=1}^{r} \frac{\delta\Pi^{(e)}}{\delta v_i} \delta v_i = 0 \tag{3.29}$$

But the δu_i and the δv_i are independent variations and equation (3.29) is satisfied only if

$$\frac{\delta\Pi^{(e)}}{\delta u_i} = \frac{\delta\Pi^{(e)}}{\delta v_i} = 0,\ i = 1, 2, ..., r \tag{3.30}$$

for every element (e) of the system. Equation (3.30) expresses the condition we use

to find the element equations. A typical equation in submatrix form is

$$\left\lfloor [k]^{q1}[k]^{q2}...[k]^{qp}...[k]^{qr} \right\rfloor \begin{bmatrix} u_1 \\ v_1 \\ \vdots \\ u_q \\ v_q \\ \vdots \\ u_r \\ v_r \end{bmatrix} = \mathbf{F}^q, \qquad q = 1, 2, ..., r \tag{3.31}$$

where $p = 1, 2, ..., r$ and r is the number of element nodes. A typical 2×2 submatrix $[k]^{qp}$ denotes the stiffness relationship between nodes q and p and $\mathbf{F}^q$ is the resultant external load vector at node q.

$$\begin{aligned} \frac{\delta\Pi^{(e)}}{\delta u_q} \Big/ \frac{\delta\Pi^{(e)}}{\delta u_v} = 0 = \int\int_{A^{(e)}} \mathbf{B}_q^{T^{(e)}} \mathbf{C}^{(e)} \mathbf{B}_p^{(e)} \boldsymbol{\delta}^q t^{(e)} dA^{(e)} \\ - \int\int_{A^{(e)}} \mathbf{B}_q^{T^{(e)}} \mathbf{C}^{(e)} \boldsymbol{\varepsilon}_{0q}^{(e)} t^{(e)} dA^{(e)} \\ - \int\int_{A^{(e)}} \mathbf{N}_q \mathbf{F}_q^{(e)} t^{(e)} dA^{(e)} - \int_{C_i^{(e)}} \mathbf{N}_q \mathbf{T}_q^{(e)} dS_q^{(e)} \end{aligned} \tag{3.32}$$

where

$$\boldsymbol{\delta}^q = \begin{Bmatrix} u_q \\ v_q \end{Bmatrix} \tag{3.33}$$

is the column vector of the two displacement components at node q.

$$\mathbf{B}_q^{(e)} = \begin{bmatrix} \delta\mathbf{N}_q/\delta x & 0 \\ 0 & \delta\mathbf{N}_q/\delta y \\ \delta\mathbf{N}_q\delta y & \delta\mathbf{N}_q/\delta x \end{bmatrix} \qquad q = 1, 2, ..., r \tag{3.34}$$

The definition of the strain-displacement matrix, $\mathbf{B}_q^{(e)}$, in equation (3.34), for a two-dimensional elastic follows from the definitions of the three non-zero strain components ε_x, ε_y, and γ_{xy}. Since the traction vector $\mathbf{T}$ is a boundary effect, the last term of equation (3.32) applies only if element (e) lies on the boundary where traction is specified.

Equation (3.32) is the force-displacement relation for node q. In matrix notation it can be written as

$$\mathbf{k}^{qp}\boldsymbol{\delta}^q = \mathbf{F}_0{}^q + \mathbf{F}_B{}^q + \mathbf{F}_T{}^q = \mathbf{F}^q \tag{3.35}$$

where

$$\mathrm{k}^{qp} = \int\int_{A^{(e)}} \mathrm{B}_q^{T^{(e)}} \mathrm{C}^{(e)} \varepsilon_{0_q}^{(e)} t^{(e)} dA^{(e)} \tag{3.36}$$

is the initial force vector at node q,

$$\mathrm{F}_B{}^q = \int\int_{A^{(e)}} \mathrm{N}_q(x,y) \mathrm{F}_q^{(e)} t^{(e)} dA^{(e)} \tag{3.37}$$

is the nodal body force vector and

$$\mathrm{F}_T{}^q = \int\int_{C_1^{(e)}} \mathrm{N}_q(x,y) \mathrm{T}_q^{(e)} dS_q^{(e)} \tag{3.38}$$

is the nodal force vector due to surface loading (present only for boundary elements). Finally $\mathbf{F}^q$ resultant external load vector at node q

Equation (3.35) expresses the stiffness submatrices associated with a typical node, but since each element has r nodes, the complete stiffness for the element is a $2r \times 2r$ matrix of the form

$$\mathrm{K}^{(e)} = \begin{bmatrix} \mathrm{k}^{11} & \mathrm{k}^{12} & \dots & \mathrm{k}^{1r} \\ \mathrm{k}^{21} & \mathrm{k}^{22} & \dots & \mathrm{k}^{2r} \\ \vdots & \vdots & \vdots & \vdots \\ \mathrm{k}^{q1} & \mathrm{k}^{q2} & \dots & \mathrm{k}^{qr} \\ \vdots & \vdots & \vdots & \vdots \\ \mathrm{k}^{r1} & \mathrm{k}^{r2} & \dots & \mathrm{k}^{rr} \end{bmatrix} \tag{3.39}$$

The arrangement of terms in the element stiffness matrix implies that the column matrix of discrete nodal displacements for the elements has the form

$$\boldsymbol{\delta}^{(e)} = \begin{Bmatrix} \boldsymbol{\delta}^1 \\ \boldsymbol{\delta}^2 \\ \vdots \\ \boldsymbol{\delta}^r \end{Bmatrix} = \begin{Bmatrix} u_1 \\ v_1 \\ u_2 \\ v_2 \\ \vdots \\ u_r \\ v_r \end{Bmatrix} \tag{3.40}$$

thus the force-displacement equations for the element take the standard form

$$\mathrm{K}^{(e)} \boldsymbol{\delta}^{(e)} = \mathrm{F}^{(e)} \tag{3.41}$$

where

$$\mathbf{F}^{(e)} = \begin{Bmatrix} \mathbf{F}^1 \\ \mathbf{F}^2 \\ \vdots \\ \mathbf{F}^q \\ \vdots \\ \mathbf{F}^r \end{Bmatrix} \tag{3.42}$$

It is important to note that $\boldsymbol{\delta}^{(e)}$, defined by equation (3.40), is the column vector of discrete nodal displacements for element (e), whereas $\tilde{\boldsymbol{\delta}}^{(e)}$, defined by equation (3.2) is the column vector of the continuous displacement field within the element.

3.5.4 The System Equations

Equation (3.39) with its components given by equation (3.11) is the general form of the element stiffness matrix for two-dimensional elasticity problems. The system equations have the same form as the element equations except that they are expanded in dimension to include all nodes. Hence, when the discretised system has m nodes, the system equations become

$$\mathbf{K}^{(2m\times 2m)}\,\boldsymbol{\delta}^{(2m\times 1)} = \mathbf{F}^{(2m\times 1)} \tag{3.43}$$

where $\boldsymbol{\delta}$ is now a column vector of nodal displacement components for the entire system and $\mathbf{F}$ is the column vector of the resultant nodal forces. For the displacement formulation either force or displacement is known in every node of the system. If body forces and initial strains are absent, the vector $\mathbf{F}$ has zero components except for the components corresponding to nodes where concentrated external forces or displacements are specified.

For steady-state problems, once the system equations are solved for the nodal displacements, the basic relations between stress and strain, and strain and displacement, may be defined to find the stress at any point in any of the elements. A general equation for the stress components, including stresses due to displacements

and initial strains, can be written as

$$\boldsymbol{\sigma}^{(e)} = \mathbf{C}^{(e)}\mathbf{B}^{(e)}\boldsymbol{\delta}^{(e)} - \mathbf{C}^{(e)}\boldsymbol{\varepsilon}_0{}^{(e)} \tag{3.44}$$

If any initial stresses are present, these should also be added.

3.5.5 Formulation for Small Deformation Non-Linear Problems

In the case of non-linear or time dependent stress-strain relationships, the formulation of the problem needs to be modified. For small strain applications and using a fixed Cartesian coordinate system, the equilibrium equations are given as

$$\sigma_{ij,j} + b_i = \rho \ddot{u}_i \qquad i,j = 1,2,3 \tag{3.45}$$

were σ_{ij} are the components of the true or Cauchy stress, ρ the mass density, b_i the components of the body forces and $\ddot{u}_i$ the components of the acceleration vector (the displacement vector δ used previously is replaced with u to avoid ambiguity later). Balance of moments results in the symmetry of the stress tensor such that

$$\sigma_{ij} = \sigma_{ji} \tag{3.46}$$

and the boundary conditions are given in terms of the traction condition

$$\bar{t}_i = \sigma_{ij} n_j \tag{3.47}$$

where t_i refer to the components of the traction vector acting on the boundary and n_j are the components of the normal to the boundary surface. The variational formulation may be stated as

$$\int_\Omega \delta u_i \rho \ddot{u}_i \, d\Omega + \int_\Omega \delta\varepsilon_{ij}\sigma_{ij} \, d\Omega - \int_\Omega \delta u_i b_i \, d\Omega - \int_\Gamma \delta u_i t_i \, d\Gamma = 0 \tag{3.48}$$

or in matrix form as

$$\int_\Omega \delta\mathbf{u}^T \rho \ddot{\mathbf{u}} \, d\Omega + \int_\Omega \delta\boldsymbol{\varepsilon}^T \sigma \, d\Omega - \int_\Omega \delta\mathbf{u}^T \mathbf{b} \, d\Omega - \int_\Gamma \delta\mathbf{u}^T \bar{\mathbf{t}} \, d\Gamma = 0 \tag{3.49}$$

The virtual strains are expressed in terms of the virtual displacements as

$$\delta\varepsilon_{ij} = \tfrac{1}{2}\left(\delta u_{i,j} + \delta u_{j,i}\right) \tag{3.50}$$

or in matrix form as

$$\delta\boldsymbol{\varepsilon} = \mathbf{S}\delta\mathbf{u} \tag{3.51}$$

The finite element approximations for the displacements are given in terms of the shape functions $\mathbf{N}(\mathbf{x})$ and nodal displacements $\tilde{\mathbf{u}}(t)$ as

$$\mathbf{u}(\mathbf{x}, t) = \mathbf{N}(\mathbf{x})\tilde{\mathbf{u}}(t) \tag{3.52}$$

and the virtual displacements may be written as

$$\delta\mathbf{u}(\mathbf{x}, t) = \mathbf{N}(\mathbf{x})\tilde{\mathbf{u}}(t) \tag{3.53}$$

The virtual strains may then be obtained by substitution to give

$$\delta\boldsymbol{\varepsilon} = (\mathbf{SN})\delta\tilde{\mathbf{u}} = \mathbf{B}\ \delta\tilde{\mathbf{u}} \tag{3.54}$$

The equilibrium condition for the discrete problem may then be stated as

$$\mathbf{M}\ddot{\mathbf{u}} + \mathbf{P} = \mathbf{f} \tag{3.55}$$

where

$$\mathbf{M} = \int_{\Omega} \mathbf{N}^T \rho \mathbf{N}\, d\Omega \tag{3.56}$$

$$\mathbf{f} = \int_{\Omega} \mathbf{N}^T \mathbf{b}\, d\Omega - \int_{\Gamma} \mathbf{N}^T\, \bar{\mathbf{t}} d\Gamma \tag{3.57}$$

$$\mathbf{P} = \int_{\Omega} \mathbf{B}^T \boldsymbol{\sigma}\, d\Omega \tag{3.58}$$

In the case of a non-linear or time dependent stress-strain relationship the stress is described as a general function of the strain

$$\boldsymbol{\sigma} = \boldsymbol{\sigma}(\boldsymbol{\varepsilon}) \tag{3.59}$$

In order to obtain the set of algebraic equations required for the solution of the discrete problem, the equilibrium condition is considered at each discrete time step

such that at time t_{n+1} the equilibrium equation may be expressed in a residual form as

$$\Psi_{n+1} = \mathbf{f}_{n+1} - \mathbf{M}\ddot{\mathbf{u}}_{n+1} - \mathbf{P}_{n+1} = 0 \tag{3.60}$$

where the stress divergence terms is given as

$$\mathbf{P}_{n+1} = \int_{\Omega} \mathbf{B}^T \boldsymbol{\sigma}_{n+1}\, d\Omega = \mathbf{P}(\mathbf{u}_{n+1}) \tag{3.61}$$

The discrete displacements, velocities and accelerations for the time step $\Delta t = t_{n+1} - t_n$ are linked by

$$\mathbf{u}_{n+1} = \mathbf{u}_n + \Delta t \dot{\mathbf{u}}_n + \tfrac{1}{2}(1-\beta_2)\Delta t^2 \ddot{\mathbf{u}}_n + \tfrac{1}{2}\beta_2 \Delta t^2 \ddot{\mathbf{u}}_{n+1} \tag{3.62}$$

$$\dot{\mathbf{u}}_{n+1} = \dot{\mathbf{u}}_n + (1-\beta_1)\Delta t\ \ddot{\mathbf{u}}_n + \beta_1 \Delta t\ \ddot{\mathbf{u}}_{n+1} \tag{3.63}$$

Generally u_{n+1} is taken as the basic variable from which $\dot{u}_{n+1}$ and $\ddot{u}_{n+1}$ are calculated. The solution of the non-linear equilibrium equations for the time step therefore requires an iterative procedure, for example the Newton-Raphson method requires that

$$\Psi_{n+1}^{k+1} \cong \Psi_{n+1}^{k} + \frac{\partial \Psi^k}{\partial \mathbf{u}_{n+1}} d\mathbf{u}_n^k = 0 \tag{3.64}$$

where $d\mathbf{u}_n^k$ is the increment change in displacement such that

$$\mathbf{u}_{n+1}^{k+1} = \mathbf{u}_{n+1}^{k} + d\mathbf{u}_n^k \tag{3.65}$$

The above expression may be alternatively expressed in terms of the total increment $\Delta \mathbf{u}_n^{k+1}$ and the converged solution from the previous time step $\mathbf{u}_n$ as

$$\mathbf{u}_{n+1}^{k+1} = \mathbf{u}_n + \Delta \mathbf{u}_n^{k+1} \tag{3.66}$$

The accumulation of the total increment can therefore be expressed as

$$\Delta \mathbf{u}_n^{k+1} = \mathbf{u}_{n+1}^{k+1} - \mathbf{u}_n = \Delta \mathbf{u}_n^k + d\mathbf{u}_n^k \tag{3.67}$$

For the initial iteration

$$\mathbf{u}_{n+1}^{1} = \mathbf{u}_n \tag{3.68}$$

which results in

$$\mathbf{u}_n^1 = 0 \tag{3.69}$$

The displacement increment may therefore be calculated as

$$d\mathbf{u}_n^k = \left(\mathbf{K}_T^k\right)^{-1} \Psi_{n+1}^k \tag{3.70}$$

where $\mathbf{K}_T^k$ is termed the tangent matrix and is defined as

$$\mathbf{K}_T^k = -\frac{\partial \Psi^k}{\partial \mathbf{u}_{n+1}} \tag{3.71}$$

The expression for the tangent matrix may alternatively be expressed in terms of the equilibrium equations as

$$\mathbf{K}_T^k = \frac{\partial \mathbf{P}^k}{\partial \mathbf{u}_{n+1}} + \mathbf{M}\frac{\partial \ddot{\mathbf{u}}_{n+1}}{\partial \mathbf{u}_{n+1}} = \int_\Omega \mathbf{B}^T \mathbf{D}_T^k \mathbf{B}\, d\Omega + \frac{2}{\beta_2 \Delta t^2}\mathbf{M} \tag{3.72}$$

Iteration continues until a solution satisfying the convergence tolerance ε is obtained, i.e.

$$\left\|\Psi_{n+1}^k\right\| \leq \varepsilon \left\|\Psi_{n+1}^1\right\| \tag{3.73}$$

The treatment of problems involving non-linear elasticity is often based on an approach where the strain energy is used to derive the tangent stiffness matrix. The strain energy W may be expressed in terms of the strain

$$W = W(\varepsilon) \tag{3.74}$$

from which the stress may be written as

$$\boldsymbol{\sigma} = \frac{\partial W}{\partial \varepsilon} \tag{3.75}$$

The tangent modulus $\mathbf{D}_T^k$ is then determined from

$$\mathbf{D}_T^k = \left(\frac{\partial^2 W}{\partial \varepsilon \partial \varepsilon}\right)_{n+1}^k \tag{3.76}$$

and the strain-displacement matrix $\mathbf{B}$ from

$$\mathbf{B} = \frac{\partial \varepsilon}{\partial \mathbf{u}} \tag{3.77}$$

3.5.6 Finite Deformation Formulation

Kinematics

The treatment of problems involving large displacements, i.e. finite deformation, involves the use of the reference and deformed configurations. The initial position vector $\mathbf{X}$ may be given in terms of a cartesian coordinate system as

$$\mathbf{X} = X_I \mathbf{E}_I \qquad I = 1, 2, 3 \tag{3.78}$$

where $\mathbf{E}$ is the vector containing the orthogonal unit vectors consistent with the reference configuration. The deformed position vector $\mathbf{x}$ may be described with reference to the current deformed configuration as

$$\mathbf{x}_i = x_i \mathbf{e}_i \qquad i = 1, 2, 3 \tag{3.79}$$

where $\mathbf{e}$ are the orthogonal unit vectors for the current state.

The current position vector may be expressed in terms of the reference configuration as

$$x_i = \phi_i(\mathbf{X}, t) \tag{3.80}$$

where ϕ_i is a mapping function and is analogous to the displacement vector. Using common origins and directions for the reference and deformed configurations allows the displacement vector to be expressed as the change U between the two frames i.e.

$$x_i = \delta_{iI}(X_I - U_I) \tag{3.81}$$

The displacement components may therefore be written in terms of the reference or deformed configurations as

$$u_i = \delta_{iI} U_I \tag{3.82}$$

and

$$U_i = \delta_{iI}\, u_i \tag{3.83}$$

respectively. The displacement vector may be differentiated to give

$$d\mathbf{x} = \frac{\partial \mathbf{x}}{\partial \mathbf{X}}\, d\mathbf{X} = \mathbf{F} d\mathbf{X} \tag{3.84}$$

where $\mathbf{F}$ is the deformation gradient with respect to the reference configuration i.e.

$$\mathbf{F} = \frac{\partial \phi}{\partial \mathbf{X}} \tag{3.85}$$

The expression may also be written in terms of the displacement-derivative matrix $\mathbf{D}$ as

$$d\mathbf{x} = (\mathbf{I} + \mathbf{D})d\mathbf{X} \tag{3.86}$$

where

$$\mathbf{D} = \frac{\partial \mathbf{u}}{\partial \mathbf{X}} \tag{3.87}$$

In order to ensure that the elemental volume remains positive the deformation gradient is subject to the constraint that

$$J = \det \mathbf{F} > 0 \tag{3.88}$$

The determinant J may be used to map the elemental volume in the reference configuration to one in the deformed configuration

$$d\upsilon = JdV \tag{3.89}$$

The deformation gradient may be expressed directly in terms of the displacement as

$$F = \delta_{iI} + \frac{\partial u_i}{\partial X_I} \tag{3.90}$$

In this form the deformation gradient is referred to both the reference and the deformed configurations and it is usual to reconfigure the form to reflect only the reference or deformed configurations.

Stress and strain measures

In the case of large deformations the change in the change in the length of a line element from the reference configuration to the current may be expressed as

$$d\mathbf{x}^2 - d\mathbf{X}^2 = 2d\mathbf{X}^T \mathbf{E}\, d\mathbf{X} \tag{3.91}$$

where $\mathbf{E}$ is referred to as the Green strain tensor which may be expressed as

$$\mathbf{E} = \frac{1}{2}(\mathbf{F}^T\mathbf{F} - \mathbf{I}) \tag{3.92}$$

$$= \frac{1}{2}(\mathbf{D} + \mathbf{D}^T) + \frac{1}{2}\mathbf{D}^T\mathbf{D} \tag{3.93}$$

The term F^TF is referred to as the right Cauchy-Green deformation tensor and is denoted as C_{IJ} such that.

$$C_{IJ} = F_{iI}F_{iJ} \tag{3.94}$$

The strain in the reference configuration may then be expressed as

$$E_{IJ} = \frac{1}{2}\left(\frac{\partial U_I}{\partial X_J} + \frac{\partial U_J}{\partial X_I} + \frac{\partial U_K}{\partial X_I} + \frac{\partial U_K}{\partial X_J}\right) \tag{3.95}$$

If the current configuration is used then the deformation tensor is similarly given as

$$b_{ij} = F_{iI}F_{jI} \tag{3.96}$$

and the strain tensor is written as

$$e_{ij} = \frac{1}{2}(\delta_{ij} - b_{ij}^{-1}) \tag{3.97}$$

The stress measures in the reference and current measures have to be considered due to the implications involved in their interpretation. The measure of stress with respect to the current configuration is termed the Cauchy or True stress $\boldsymbol{\sigma}$ whilst the stress measure taken with respect to the reference configuration is termed the second Piola-Kirchhoff stress $\mathbf{S}$. The relationship between the two stress measures may be expressed by considering an equivalent internal work approach, that is

$$\Pi_i = \int_\Omega \mathbf{S}\ \delta\mathbf{E}\ dV_0 = \int_\Omega \boldsymbol{\sigma}\delta\varepsilon\ dV \tag{3.98}$$

Using the mapping of the elemental volumes given by equation ( ) leads to

$$\int_\Omega \mathbf{S}\ \delta\mathbf{E}\ dV_0 = \int_\Omega J\boldsymbol{\sigma}\delta\varepsilon\ dV_0 \tag{3.99}$$

The term $J\boldsymbol{\sigma}$ is termed the Kirchoff stress and is denoted by τ so that

$$\boldsymbol{\tau} = J\boldsymbol{\sigma} \tag{3.100}$$

The variation of the Green strain may be determined as

$$\delta \mathbf{E} = \frac{1}{2}\mathbf{F}^T \delta \mathbf{D} + \frac{1}{2}\delta \mathbf{D}^T \tag{3.101}$$

The variation in D is may then be expressed as

$$\delta \mathbf{D} = \frac{\partial \delta \mathbf{u}}{\partial \mathbf{x}} \mathbf{F} \tag{3.102}$$

which gives

$$\delta \mathbf{E} = \frac{1}{2}(\mathbf{F}^T \frac{\partial \delta \mathbf{u}}{\partial \mathbf{x}} \mathbf{F} + \frac{\partial \delta \mathbf{u}}{\partial \mathbf{x}} \mathbf{F}) \tag{3.103}$$

The strain measurement conjugate with the Cauchy stress is given by

$$\delta \boldsymbol{\varepsilon} = \frac{1}{2}\left(\frac{\partial \delta \mathbf{u}}{\partial \mathbf{x}} + \frac{\partial \delta \mathbf{u}^T}{\partial \mathbf{x}}\right) \tag{3.104}$$

Comparison of the above two equations gives

$$\delta \mathbf{E} = \mathbf{F}^T \delta \boldsymbol{\varepsilon} \mathbf{F} \tag{3.105}$$

and virtual work expression may be expressed as

$$\Pi_i = \int_\Omega \mathbf{S}\ \mathbf{F}^T \delta \boldsymbol{\varepsilon} \mathbf{F}\ dV_0 = \int_\Omega \boldsymbol{\tau} \delta \boldsymbol{\varepsilon}\ dV_0 \tag{3.106}$$

from which the relationship between the Kirchhoff stress measure and the second Piola-Kirchhoff stress measures is given as

$$\boldsymbol{\tau} = \mathbf{F}\mathbf{S}\mathbf{F}^T \tag{3.107}$$

and the Cauchy and second Piola-Kirchhoff stress measures are related by

$$\boldsymbol{\sigma} = \frac{1}{J}\mathbf{F}\mathbf{S}\mathbf{F}^T \tag{3.108}$$

Equilibrium equations

The equilibrium equations for a solid subjected to finite deformations are similar to those for small deformations given above

$$\frac{\partial \sigma_{ij}}{\partial x_i} + \rho b_j^{(m)} = \rho \dot{v}_j \tag{3.109}$$

where ρ is the mass density in the current configuration, b_j is the body force per unit mass and v_j is the velocity which is given by

$$\dot{v}_j = \frac{\partial \phi_j}{\partial t} = \dot{x}_j = \dot{u}_j \tag{3.110}$$

The mass density may be related to the reference mass density by using the elemental volume mapping i.e.

$$\rho_o = J\rho \tag{3.111}$$

As with small deformations the balance of moments results in the symmetry of the stress tensor, i.e.

$$\sigma_{ij} = \sigma_{ji} \tag{3.112}$$

Reference configuration formulation

The variational formulation may be written in terms of a virtual work expression as

$$\Pi = \int_\Omega W\left(C_{IJ}\right) dV - \Pi_e \tag{3.113}$$

where $W(C_{IJ})$ is a stored energy function. The stress measure that is conjugate with the Green's strain tensor is the second Piola-Kirchoff stress which is given as

$$S_{IJ} = 2\frac{\partial W}{\partial C_{IJ}} = \frac{\partial W}{\partial E_{IJ}} \tag{3.114}$$

The stored energy function may then be expressed as

$$W(E_{IJ}) = \frac{1}{2} D_{IJKL} E_{IJ} E_{KL} \tag{3.115}$$

where D_{IJKL} are material elastic moduli, the stress tensor may therefore be expressed as

$$S_{IJ} = D_{IJKL} E_{KL} \tag{3.116}$$

The external virtual work term is expressed as

$$\Pi_e = \int_\Omega U_I \rho_0 b_I dV + \int_\Gamma U_I \bar{T}_I \, dS \tag{3.117}$$

The variational forms of the virtual work expressions may then be given as

$$\delta\Pi = \int_\Omega \frac{1}{2}\delta C_{IJ} S_{IJ} dV - \delta\Pi_e = 0 \tag{3.118}$$

and

$$\delta\Pi_e = \int_\Omega \delta U_I \rho_0 b_I dV + \int_\Gamma \delta U_I \bar{T}_I \, dS \tag{3.119}$$

The first term may be expressed as

$$\frac{1}{2}\delta C_{IJ} S_{IJ} = \delta E_{IJ} S_{IJ} = \delta F_{iI} F_{iJ} S_{IJ} \tag{3.120}$$

The variation of the deformation gradient is expressed in terms of the variation of the displacements as

$$\delta F_{iI} = \frac{\partial \delta u_i}{\partial X_I} \tag{3.121}$$

The variational equation may now be written as

$$\delta\Pi = -\int_\Omega \delta u_i \left[(F_{iJ} S_{IJ})_{,I} + \delta_{iI} \rho_0 b_I \right] dV + \int_\Gamma \delta u_i \left[F_{iJ} S_{IJ} N_I - \delta_{iI} \bar{T}_I \right] dS = 0 \tag{3.122}$$

which gives the equations of static equilibrium as

$$(F_{iJ} S_{IJ})_{,I} + \delta_{iI} \rho_0 b_I = P_{iI,I} + \rho_0 b_i = 0 \tag{3.123}$$

The finite element approximation is constructed using

$$X_I = \sum N(\xi, \eta, \zeta) \bar{X}_I \tag{3.124}$$

where N are shape functions expressed in terms of the natural coordinates ξ, η and ζ of the element. $\bar{X}_I$ are the nodal values of the coordinate. The approximation of the displacement field is then given as

$$u_i = \sum N(\xi, \eta, \zeta) \bar{u}_i \tag{3.125}$$

$$\frac{\partial u_i}{\partial X_I} = \sum \frac{\partial N}{\partial X_I} u_i \tag{3.126}$$

The variation of the Green strain is expressed as

$$\delta \mathbf{E} = \mathbf{B} \delta \bar{\mathbf{u}} \tag{3.127}$$

The variational equation for the finite element problem is given by

$$\delta\Pi = \delta\bar{\mathbf{u}}^T \int_\Omega \mathbf{B}\mathbf{S}dV - \Pi_e = 0 \tag{3.128}$$

where the external potential is given as

$$\Pi_e = \int_\Omega \mathbf{N}\rho_0 b dV + \int_\Gamma \mathbf{N}T dS \tag{3.129}$$

The tangent matrix is therefore given by

$$K^T = \int_\Omega \mathbf{B}^T\mathbf{D}\mathbf{B}dV + \int_\Omega \frac{\partial \mathbf{B}}{\partial \mathbf{u}}\mathbf{S}dV - \frac{\partial f}{\partial \mathbf{u}} = \mathbf{K}_M + \mathbf{K}_G + \mathbf{K}_L \tag{3.130}$$

Current Configuration Formulation

Recalling that the variation of the Green strain may be written as

$$\delta E_{IJ} = \frac{1}{2}\left(\frac{\partial \delta u_i}{\partial X_I}F_{iJ} + \frac{\partial \delta u_i}{\partial X_J}F_{iI}\right) \tag{3.131}$$

and that the True strain may be then be expressed as

$$\delta E_{IJ} = \delta\varepsilon_{ij}F_{iI}F_{jJ} \tag{3.132}$$

so that

$$\delta E_{IJ}S_{IJ} = \delta\varepsilon_{ij}F_{iI}F_{jJ}S_{IJ} = \delta\varepsilon_{ij}\tau_{ji} = \delta\varepsilon_{ij}\sigma_{ij}J \tag{3.133}$$

The variation of the virtual work may now be expressed as

$$\delta\Pi = \int_\Omega \delta\varepsilon_{ij}\sigma_{ij}JdV - \delta\Pi_e = 0 \tag{3.134}$$

Substituting for $d\upsilon = JdV$ gives

$$\delta\Pi = \int_\omega \delta\varepsilon_{ij}\sigma_{ij}d\upsilon - \delta\Pi_e = 0 \tag{3.135}$$

The external potential may similarly be expressed in terms of the current configuration as

$$\delta\Pi_e = \int_\omega \delta u_i \rho b_i \, d\upsilon + \int_\gamma \delta u_i \bar{t}_i \, dS \tag{3.136}$$

The finite element approximation follows that developed for the small deformation problem, the only difference being that the shape functions and their derivatives

are based on the current configuration which is determined using equation ( ). The stress term in the variational equation is therefore given as

$$\int_{\omega} \delta\varepsilon_{ij}\sigma_{ij}\, dv = \delta\bar{\mathbf{u}}^T \int_{\omega} \mathbf{B}^T\boldsymbol{\sigma} dv \tag{3.137}$$

The residual of the static problem is then given by

$$\Psi = f - \int_{\omega} \mathbf{B}^T\boldsymbol{\sigma} dv = 0 \tag{3.138}$$

The tangent matrix is then calculated

$$K_M = \int_{\omega} \mathbf{B}^T\mathbf{D}\mathbf{B} dv + \mathbf{G}\mathbf{I} \tag{3.139}$$

3.6 Magnetostatic Response Modelling - The Application of the Finite Element Method to Linear Magnetostatic Problems

The solution of magnetostatic problem using the finite element method is well established, an early example is given by [185] in which the solutions for electrostatic field distributions governed by Laplace equations are solved for. Other examples are discussed in [187] and [186]. The solution of the magnetostatic problem is relatively simple and is achieved through the use of a vector potential or more specifically the magnetic vector potential.

3.6.1 Finite element formulation

The induction problem considered within the scope of this study may be treated as magnetostatic, that is, the fields may be considered to be time-invariant. The steady state field strength $\mathbf{H}$ is governed by Maxwell's equations

$$\nabla \times \mathbf{H} = -\mathbf{J} \tag{3.140}$$

$$\nabla^T\mathbf{B} = 0 \tag{3.141}$$

subject to the constitutive relationship

$$\mathbf{B} = \mu\mathbf{H} \tag{3.142}$$

where $\mathbf{B}$ refers to the flux density, $\mathbf{J}$ to the current density and μ to the magnetic permeability. If the material is non-linear, the permeability, μ is a function of $\mathbf{B}$ i.e.

$$\mu = \frac{\mathbf{B}}{\mathbf{H}(B)}$$

The solution for the problem is obtained using a vector potential approach in which the flux density is written in terms of a magnetic vector potential A. The first step involves defining the solution for the case when $\mu = 1$ everywhere within the domain of the problem Ω. The field intensity $\mathbf{H}$ that satisfy this case and the governing equations is given by

$$\mathbf{H}_s = \frac{1}{4}\pi \int_\Omega \frac{\mathbf{J} \times (\mathbf{r} - \mathbf{r}')}{(\mathbf{r} - \mathbf{r}')^T(\mathbf{r} - \mathbf{r}')}\, d\Omega \tag{3.143}$$

where $\mathbf{r}'$ refers to the coordinates of the problem domain Ω. The total field strength is then given by

$$\mathbf{H} = \mathbf{H}_s + \mathbf{H}_m \tag{3.144}$$

in which $\mathbf{H}_m$ accounts for the contribution of the areas where the permeability is other than unity. Substitution of equation (3.144) into equations (3.140, 3.141 and 3.142) gives

$$\nabla \times \mathbf{H}_m = 0 \tag{3.145}$$

$$\nabla^T \mathbf{B} = 0 \tag{3.146}$$

$$\mathbf{B} = \mu(\mathbf{H}_s + \mathbf{H}_m) \tag{3.147}$$

Introducing the vector potential A as

$$\mathbf{H}_m = \nabla \times \mathbf{A} \tag{3.148}$$

results in the governing equation

$$\nabla^T \mu \nabla A + \nabla^T \mu \mathbf{H}_s = 0 \tag{3.149}$$

Following the application of the variational principle, the functional

$$\Pi = \frac{1}{2}\int_{\Omega} (\nabla A)^T \mu \nabla A d\Omega + \int_{\Omega} A \nabla^T \mu \mathbf{H}_s d\Omega \tag{3.150}$$

gives, on minimisation, the satisfaction of the original governing equations.

Finite element descretisation follows similar procedures as discussed previously. The vector potential is assumed to have the form

$$A = \sum N_i a_i = \mathbf{Na} \tag{3.151}$$

where $\mathbf{N}$ is the vector of appropriate shape functions. The minimisation of the variational equation gives

$$\int_{\Omega} (\nabla N_i)^T \mu \nabla \mathbf{N} d\Omega + \int_{\Omega} N_i \nabla^T \mu \mathbf{H}_s d\Omega = 0 \tag{3.152}$$

which may be restated as a standard set of discrete equations of the form

$$\mathbf{Ka} + \mathbf{f} = \mathbf{0} \tag{3.153}$$

with

$$K_{ij} = \int_{\Omega} (\nabla N_i)^T \mu \nabla N_j d\Omega \tag{3.154}$$

$$f_i = \int_{\Omega} N_i \nabla^T \mu \mathbf{H}_s d\Omega \tag{3.155}$$

3.6.2 Boundary Conditions

Boundary conditions for the magnetostatic problem may be classified within three groups

1. Dirichlet: In this type of boundary condition, the value of the vector potential A is explicitly defined on the boundary, the most common use of Dirichlet-type boundary conditions is to define a zero value for the vector potential along a boundary to keep flux from crossing the boundary. This is commonly used to simulate symmetry conditions.

2. Neuman:. This boundary condition specifies the normal derivative of the vector potential along the boundary. It is usually employed along a boundary to force flux to pass the boundary at exactly a 90 degree angle to the boundary, i.e. $\frac{\partial A}{\partial n} = 0$, thereby allowing accurate modelling of interfaces between material with widely differing permeabilities.

3. Mixed: The mixed boundary condition is a combination of the Dirichlet and Neumann boundary conditions, the boundary condition is used to prescribe a relationship between the value of the vector potential and its normal derivative at the boundary i.e.

$$c_0 \frac{\partial A}{\partial n} + c_1 A = 0 \tag{3.156}$$

3.6.3 Open boundary problems

A common problem encountered in the application of the finite element method to the magnetostatic problem involves the realistic representation of the boundary condition where

$$A = 0 \qquad for \qquad r = \infty \tag{3.157}$$

The simplest approach is to define a boundary sufficiently far enough away from the area of interest . This results in a large solution domain with correspondingly large solution times. There are several techniques that may be used to overcome this problem.

Asymptotic boundary conditions

The application of a so-called mixed or asymptotic boundary condition can provide a suitable approximation to an open boundary condition. If a two dimensional problem is considered then as $r \rightarrow \infty$, the magnetic vector potential A will tend to zero. If a circular shell of radius r_0 is contained within the unbounded domain then

the vector potential can be given as

$$A(r,\theta) = \sum_{m=1}^{\infty} \frac{a_m}{r^m} \cos(m\theta + \alpha_m) \tag{3.158}$$

where a_m and α_m are parameters specified such that the solution matches the prescribed potential on the surface of the circle. The open field solution for a large radius r can be approximated by

$$A(r,\theta) \simeq \frac{a_n}{r^n} \cos(n\theta + \alpha_n) \tag{3.159}$$

and differentiating with respect to r gives

$$\frac{\partial A}{\partial r} = -\frac{n a_n}{r^{n+1}} \cos(n\theta + \alpha_n) \tag{3.160}$$

Solving for a_n and substituting back gives

$$\frac{\partial A}{\partial r} + \left(\frac{n}{r}\right) A = 0 \tag{3.161}$$

This is similar to the form of the mixed boundary condition as given previously by equation (3.156). In this case the asymptotic boundary condition may be specified as

$$c_1 = \frac{n}{\mu_0 r_0} \tag{3.162}$$

$$c_0 = 0 \tag{3.163}$$

Kelvin transformation

The application of the so-called Kelvin transformation to the open boundary problem is discussed in [183] and [184]. The far field region is typically homogenous and free of sources and the field equation for the magnetic vector potential will take the form (in polar notation)

$$\frac{1}{r}\frac{\partial}{\partial r}\left(r\frac{\partial A}{\partial r}\right) + \frac{1}{r^2}\left(\frac{\partial^2 A}{\partial \theta^2}\right) = 0 \tag{3.164}$$

It is assumed that the near-field region is contained within a circular shell of radius r_o which is centered at the origin. The unbounded region may be mapped onto a bonded region. If a variable R is defined such that

$$R = \frac{r_0^2}{r} \tag{3.165}$$

then the differential equation may be written as

$$\frac{\partial}{\partial r} = \frac{\partial}{\partial R}\left(\frac{dR}{dr}\right) = -\frac{\partial}{\partial R}\left(\frac{R}{r_o}\right)^2 \tag{3.166}$$

and the differential equation is written as

$$\frac{1}{R}\frac{\partial}{\partial R}\left(R\frac{\partial A}{\partial R}\right) + \frac{1}{R^2}\frac{\partial^2 A}{\partial \theta^2} = 0 \tag{3.167}$$

The form of the problem has the same as that for the near-field region. The implication is that the far field region may be modelled by considering the superposition of two domains the first representing the region of interest using the conventional formulation and the second representing the far field effects using the above formulation.

3.6.4 Solvers

For the solution of most problems employing the vector potential, variations of the Iterative Conjugate Gradient solver are generally used. This technique is appropriate for the solution of magnetostatic problems as generally the matrices are symmetric and sparse. For magnetostatic problems, a modified form termed the preconditioned conjugate gradient (PCG) code [188] may be used to increase the efficiency of the solution. The Incomplete Cholesky preconditioner approach has also been used [188], however this does require additional computational effort. The Symmetric Successive Over-Relaxation (SSOR) preconditioner, as described in [189], is also used with the advantage that this preconditioner promotes solution speed.

Chapter 4

Development of Constitutive Equations for TRIP Steels

4.1 Introduction

The martensitic transformation that occurs in metastable TRIP steels as a result of plastic straining provides a method for the correlation of strain with applied load. However, the prediction of martensite evolution as a function of load requires a well-developed and consistent constitutive model. It should also be recognised that there are essentially two modes of martensite transformation; the so-called stress-assisted and the strain-induced modes. At temperatures above the martensite start temperature, transformation can be induced via stress-assisted nucleation. The transformation is thought to be initiated at the sites responsible for transformation as a result of cooling. The transformation behaviour in the so-called stress assisted regime has been modelled by Olson and Cohen [190] where the treatment focuses on the thermodynamic influence of the applied stress in the cooling kinetics. The following discussion is primarily concerned with transformation dominated by strain-induced nucleation which generally occurs in the temperatures above the martensite start temperature. Transformation, in this case, is controlled by nucleation sites created

by plastic strain and the kinetics involve a complex relationship between slip in the austenite phase and the transformation parameters [191]. The following discussion deals with the functional dependence of the martensite evolution on the strain and stress state within the material. Various models describing the transformation kinetics and corresponding constitutive formulations are presented. The models range from relatively simple treatments in which only the plastic strain is considered to complex versions in which the strain rate, the stress state and temperature influences are included .

4.2 Kinetics of Martensite Transformation

Martensite formation involves the transformation of the metastable austenite phase through a shear process in the austenite lattice structure. The reaction is diffusionless and results in a hard structure which is highly crystallographic. The resultant lath-like or lenticular microstructure has well defined habit planes within each grain of transformed martensite. In general the reaction may be considered to be athermally activated; the transformation is initiated at the martensitic start temperature $M_s$and ceases at the M_f temperature when the austenite phase has fully transformed to martensite. In practice not all the austenite transforms and a small amount of retained austenite is usually present. The rate at which the austenite is cooled must be sufficiently high such that the diffusion controlled ferrite and pearlite reactions are suppressed [192].

4.2.1 Nucleation and Growth of Martensite

Although the martensite transformation reaction is considered to be athermal, the reaction may proceed at a constant temperature due to the dependence of the transformation kinetics on the chemical free energy, the strain energy and interfacial energy between the parent and martensite phases [193]. From the thermal perspective

the driving force required to initiate the reaction may be expressed as the difference between the martensite start temperature M_s and the temperature at which the austenite and martensite have the same free energy T_0.

The classical approach to homogeneous nucleation assumes that the nucleus is initiated by a simple shear of the parent phase without the aid of grain boundaries or other types of lattices defects. The resultant free energy change ΔG should include the change in chemical free energy Δg, the strain energy and the interfacial energy. For an oblate spheroidal martensite nucleus with radius r and semi-thickness c , the free energy change is given by

$$\Delta G = \frac{4}{3}\pi r^2 c\Delta g + \frac{4}{3}\pi r c^2 A + 2\pi r^2 \alpha \tag{4.1}$$

where A is referred to as the strain energy factor, α is the free energy per unit area of the interface between parent phase and nucleus and Δg is the chemical free energy change per unit volume. The critical nucleus size σ required to initiate the activation of the nucleus is defined where the free energy is stationary with respect to the size parameters r and c, the critical values of which may be expressed as

$$c' = -\frac{2\sigma}{\Delta G} \tag{4.2}$$

$$r' = \frac{4A\sigma}{\Delta g^2} \tag{4.3}$$

which results in an overall free energy change of

$$\Delta G' = \frac{32}{3}\pi A^2 \frac{\sigma^3}{\Delta g^4}$$

For practical purposes the values of $\Delta G'$ proposed by the above treatment are too large therefore presenting an unrealistically high barrier to successful martensite nucleation based on thermal fluctuations alone. For this reason it has been suggested that martensite nucleation occurs heterogeneously on pre-existing sub-critical nuclei which are beyond the stationary point of the free energy size parameter relationship. The nuclei are considered to consist of a semi-coherent dislocation interface with the austenite and growth occurs by nucleation of adjacent dislocations thereby extending the interface boundary. Olson and Cohen [190] have specifically postulated that

the nucleation results due to faulting on the closest packed planes derived from existing groups of dislocations such as occurs at boundaries between grains, incoherent twins and inclusions. Experimental evidence also suggests that the growth velocity of the martensite transformation process is essentially independent of temperature therefore indicating that the growth process is not thermally activated. In addition, there is also evidence to suggest that isothermal growth is possible and the process is thought to be driven by slow isothermal nucleation rather than a slow growth mechanism [194].

The Effect of Deformation

Superimposed elastic and plastic stress fields have the effect of reinforcing the strain energy component of the transformation reaction as the shape change due to the shear process is a plastic deformation process. This has the effect of increasing the M_s temperature. In certain cases the M_s temperature may be close to the operating temperature and the resultant increase in M_s due to the application of plastic deformation initiates the martensite transformation reaction [195].

4.2.2 The Olsen-Cohen Transformation Model

Olson and Cohen [196] postulated that martensite nucleation occurs at the intersection of shear bands in metastable austenite. The shear bands have low values of stacking fault energies and may consist of ε' martensite, mechanical twins and dense bundles of stacking faults [197]. Nucleation is considered to be based on three basic components; the course of shear band formation, the probability of shear band intersections and the probability of a particular shear band intersection generating active nucleation sites for martensitic nucleation.

Considering the course of shear band formation, the incremental increase of the shear band volume fraction, f^{sb}, with respect to an incremental increase in applied

plastic strain, ε^p, may be expressed as

$$df^{sb} = (1 - f^{sb})\alpha d\varepsilon^p \tag{4.4}$$

The parameter α is considered to be independent of the strain and accounts for the rate of increase of the volume fraction of shear bands, f^{sb}, with respect to the plastic strain ε^p for low values of strain, i.e. when $f^{sb} \simeq 0$. α Is however dependent on the stacking fault energy and the strain rate as low stacking fault energies and high strain rates promote shear band deformation over slip deformation which should be reflected in an appropriate increase in the value of α. The number of shear bands per unit volume, N_v^{sb}, of austenite may be expressed in terms of the average volume of the shear bands, $\bar{v}^{sb}$, as

$$N_v^{sb} = \frac{f^{sb}}{\bar{v}^{sb}} \tag{4.5}$$

Therefore at low strains where $\frac{df^{sb}}{d\epsilon} = \alpha$, the shear band volume fraction, f^{sb}, increases linearly and at high strains f^{sb} approaches saturation.

Considering now the shear band intersections within the austenite parent phase, the number of shear band intersections per unit volume of austenite, N_v^I, may be expressed in terms of the number of shear bands as

$$N_v^I = K(N_v^{sb})^n \tag{4.6}$$

where K and n are constants. In the cases where the shear bands are randomly orientated $n = 2$ and $K = \frac{1}{16}\pi^2 a^2$, however in practice the shear bands are initially parallel and become more random as secondary shear effects produce additional shear bands. This is usually reflected in a value of n greater than 2.

Each shear band intersection has the potential to initiate the nucleation of a martensite transformation reaction. The incremental increase in the number of active nucleation sites per unit volume of austenite, $N_v^{\alpha'}$ may be expressed in terms of the number of shear band intersections per unit volume of austenite, N_v^I, and a probability parameter, p, as

$$dN_v^{\alpha'} = pdN_v^I \tag{4.7}$$

The probability parameter reflects the probability of an active nucleation site developing at a particular shear band intersection. If the probability is considered in terms of a potency value, that being defined as the minimum chemical driving force required to promote nucleation, then if that potency is described with a Gaussian distribution, the probability that the shear band intersections will develop into active nucleation site can be described in terms of a Gaussian frequency distribution. If it is further considered that the entropy change is generally constant then the chemical driving force will be a linear function of temperature and the probability parameter, p, can therefore be expressed as a Gaussian function of the temperature.

The growth of martensite units is usually limited to the lath shaped shear band intersections and the average volume of each martensite unit, $\bar{v}^{\alpha'}$, may therefore be considered constant. In this case the incremental increase in the martensite volume fraction, $f^{\alpha'}$, may be related to the incremental increase in active nucleation sites, $dN_v^{\alpha'}$, by

$$df^{\alpha'} = (1 - f^{\alpha'})\bar{v}^{\alpha'} dN_v^{\alpha'} \tag{4.8}$$

The martensite volume fraction, $f^{\alpha'}$, may therefore be expressed as

$$f^{\alpha'} = 1 - \exp\left(\frac{p\bar{v}^{\alpha'}K}{(\bar{v}^{sb})^n}\, f^{sb}\right) \tag{4.9}$$

Substituting for f^{sb} yields the relationship between the martensite volume fraction and plastic strain ϵ as

$$f^{\alpha'} = 1 - \exp\left\{-\beta\left[1 - \exp\left(-\alpha\varepsilon^p\right)\right]\right\} \tag{4.10}$$

where

$$\beta = \frac{p\bar{v}^{\alpha'}K}{(\bar{v}^{sb})^n} \tag{4.11}$$

The three parameters α, β, and n may therefore be used to characterise the kinetics of the strain induced transformation reaction in terms of the temperature and plastic strain.

4.2.3 The Stringfellow Transformation Model

The above approach was extended by Stringfellow et. al. [198] to account for the influence of the stress state on the evolution of martensite. In order to incorporate the stress state sensitivity the kinetics of the reaction are considered in terms of a rate based approach. Using a similar approach to that used in the Olson-Cohen model described above, the rate of increase in the martensite volume fraction, $\dot{f}^{\alpha'}$, may be expressed in terms of the rate of increase in the active nucleation sites per unit volume of austenite, $\dot{N}_v^{\alpha'}$, as

$$\dot{f}^{\alpha'} = (1 - f^{\alpha'})\bar{v}^{\alpha'}\dot{N}_v^{\alpha'} \tag{4.12}$$

where $\bar{v}^{\alpha'}$ is the average volume of a martensite unit, The number of active nucleation sites, N_v^I, is again expressed in terms of the probability p of a given shear band intersection developing into an active nucleation site, the rate of increase of the number of nucleation sites per unit volume of austenite can therefore be expressed as

$$\dot{N}_v^{\alpha'} = p\dot{N}_v^I + N_v^I\,\dot{p} \tag{4.13}$$

In order to develop the relationship for the rate of increase in the number of shear band intersections, the same relationship between the number of active nucleation sites per unit volume, N_v^I, and the number of shear bands per unit volume, N_v^{sb}, as that used in the Olson-Cohen model is employed i.e.

$$N_v^I = K(N_v^{sb})^n \tag{4.14}$$

where N_v^{sb} is stated in terms of the shear band volume fraction, f^{sb}, and the average volume of the shear bands, $\bar{v}^{sb}$

$$N_v^{sb} = \frac{f^{sb}}{\bar{v}^{sb}} \tag{4.15}$$

The rate of increase of the volume fraction of shear bands, $\dot{f}^{sb}$, is based on the rate form of equation (4.15) and may be stated as

$$\dot{f}^{sb} = (1 - f^{sb})\alpha\dot{\varepsilon}^p \tag{4.16}$$

where α is a temperature dependent parameter accounting for shear band evolution at low strains (as described previously) and $\dot{\varepsilon}^p$ is the plastic strain-rate in the austenite parent phase. Integrating gives the shear band volume fraction as

$$f^{sb} = 1 - \exp(-\alpha\varepsilon^p) \tag{4.17}$$

Using equations (4.14) and (4.17), the number of shear band intersections per unit volume of austenite, N_v^I may be expressed in terms of the plastic strain rate as

$$N_v^I = K\left[\frac{1-\exp(-\alpha\varepsilon^p)}{\bar{v}^{sb}}\right]^n \tag{4.18}$$

and the rate of increase in the number of shear band intersections is given by differentiation of the above equation.

$$\dot{N}_v^I = \frac{nK\alpha}{(\bar{v}^{sb})^n}\{[1-\exp(-\alpha\varepsilon^p)]^{n-1}\exp(-\alpha\varepsilon^p)\}\dot{\varepsilon}^p \tag{4.19}$$

The Stringfellow model also employs the concept that the development of active nucleation sites at shear band intersections is controlled by a probability that the potency of the driving force will initiate nucleation. In this case the temperature based chemical free energy driving force used in the Olson-Cohen model is extended to a thermodynamic driving force which includes the influence of the stress state. As in the Olson-Cohen model the probability of nucleation is based on the assumption that the potency may be described in terms of a Gaussian distribution. Therefore, the probability p that a shear band intersection will initiate the nucleation reaction can be stated in the form of a cumulative frequency distribution with respect to the normalised thermodynamic driving force g as

$$p = \frac{1}{\sqrt{2\pi}}\int_{-\infty}^{g}\exp\left[-\frac{1}{2}\left(\frac{g'-\bar{g}}{s_g}\right)^2\right]dg' \tag{4.20}$$

where $\bar{g}$ is the mean and s_g the standard deviation of the driving force g. The Stringfellow model proposes that the thermodynamic driving force may be expressed as a linear combination of a temperature parameter Θ and a stress state parameter Σ i.e.

$$g = g_0 - g_1\Theta + g_2\Sigma \tag{4.21}$$

The temperature controlled parameter Θ is expressed in terms of the ratio of the difference between the actual temperature and the martensite start temperature M_s and the difference between the martensite limit and start temperatures

$$\Theta = \frac{T - M_s}{M_d - M_s} \tag{4.22}$$

The stress state parameter Σ, termed the triaxiality parameter, is expressed as

$$\Sigma = \frac{-\sigma_m}{\sqrt{3}\sigma_d} \tag{4.23}$$

where σ_m and σ_d are is the volumetric and deviatoric stress invariants respectively of the true stress tensor $\mathbf{T}$.

$$\sigma_m = \tfrac{1}{3}\, tr\, \mathbf{T} \tag{4.24}$$

$$\sigma_d = \sqrt{\tfrac{1}{2}\mathbf{S}\cdot\mathbf{S}} \tag{4.25}$$

The tensor $\mathbf{S}$ is the deviatoric stress tensor which may be defined in terms of the true stress tensor as.

$$\mathbf{S} = \mathbf{T} - \frac{1}{3}(tr\ \mathbf{T})\mathbf{1} \tag{4.26}$$

where $\mathbf{1}$ is a second order identity tensor.

The thermodynamic driving force as expressed above ensures that the probability of nucleation decreases with increasing temperature and increases with increasing triaxiality. However the triaxiality ratio ensures that the probability is not directly influenced by the magnitudes of the stress invariants. Further, whilst temperature affects both the growth of shear bands and the probability of nucleation, the above treatment decouples the influences of the plastic strain rate and stress state in that the affect of the strain rate is limited to the growth of shear bands whilst the affect of the stress-state is limited to the probability of nucleation.

Under isothermal conditions the rate of change of the temperature parameter Θ will be zero and the rate of change of the probability parameter will be given by

$$\dot{p} = \frac{g_2}{\sqrt{2\pi}s_g} \exp\left[-\frac{1}{2}\left(\frac{g-\bar{g}}{s_g}\right)^2\right]\dot{\Sigma} \tag{4.27}$$

the rate of change of the triaxialty parameter is given as

$$\dot{\Sigma} = \Sigma \left(\frac{\dot{\sigma}_m}{\sigma_m} - \frac{\dot{\sigma}_d}{\sigma_d} \right) \tag{4.28}$$

The rate of change of the martensite volume fraction is calculated as

$$\dot{f}^{\alpha'} = (1 - f^{\alpha'})(A\ \dot{\varepsilon}^p + B\ \dot{\Sigma}) \tag{4.29}$$

where

$$A = \alpha\beta n(1 - f^{sb})(f^{sb})^{n-1}p \tag{4.30}$$

$$B = \frac{g_2}{\sqrt{2\pi}}\beta(f^{sb})^n \exp\left[-\frac{1}{2}\left(\frac{g - \bar{g}}{s_g} \right)^2 \right] \tag{4.31}$$

and

$$\beta = \frac{K\bar{v}^{\alpha'}}{(\bar{v}^{sb})^n} \tag{4.32}$$

4.2.4 The Tomita-Iwamoto Transformation Model

Although the Stringfellow model accounts for the effects of temperature, plastic strain and stress state, the effect of strain rate is not included. Experimental observations have suggested that the martensite transformation reaction is sensitive to the strain rate due to evidence that the mode of deformation is increasingly controlled by shear band deformation as the strain rate is increased [199]. To account for this Tomita et. al [200] have proposed a modification of the Stringfellow transformation model in which the parameter α accommodates the effect of strain rate.

The increase in the number of shear bands produced at higher strain rates will lead to a greater number of shear band intersections resulting in a higher number of potential sites for martensite nucleation. Considering that the number of shear bands is directly influenced by the parameter α the Tomita-Iwamoto model assumes that α is related to the strain-rate by a power-law expression of the form

$$\alpha = \alpha_0 \left(\frac{\dot{\varepsilon}^p}{\dot{\varepsilon}_y} \right)^M \tag{4.33}$$

where

$$\alpha_0 = \alpha_1 + \alpha_2 T + \alpha_3 T^2 \tag{4.34}$$

and M is the strain rate sensitivity exponent and $\dot{\varepsilon}_y$ is the reference strain rate. Tomita and Iwamoto have also suggested a further improvement based on the premise that the growth of shear bands is influenced by the stress state and therefore that α should include the triaxiality parameter Σ. The resultant expression for α_0 has the form

$$\alpha = \alpha_1 + \alpha_2 T + \alpha_3 T^2 - \alpha_4 \Sigma \tag{4.35}$$

The Tomita-Iwamoto model also suggests that the strain-induced transformation can occur when the sum of the chemical driving force, given by the difference between the free energy of each phase, and an additional mechanical driving force due to deformation exceeds the minimum chemical driving force required to initiate nucleation. A simplified version of the thermodynamic driving force, g, was therefore employed which is expressed as

$$g = -T + g_1 \Sigma \tag{4.36}$$

where $g_1$is a constant [201].

4.3 Constitutive Equation Formulation

Transformation induced plasticity steels may be classified in a general sense as multiphase materials due to their two-phase nature. The formulation of a suitable model for the prediction of the materials response to external loading must account for the influence of the heterogenous microstructure inherent in multiphase materials. The material heterogeneity is pronounced in TRIP steels due to the differences in the mechanical properties of the austenite and martensite phases, that is, the intrinsic elastic and plastic responses of each material portion can vary from point to point. Due to the heterogeneity imposed by the microstructure at the mesoscale level, neither the stress or the strain will be homogenous throughout the loaded material. Various models based on classical averaging approaches have been proposed by Aernoudt et.

al. [202], Nemat-Nasser et. al [203] and Stouffer and Dame [204] to deal with the mechanical anisotropy of crystalline and multiphase materials by homogenization of stress and/or strain for the mesoscopically heterogeneous phases. The averaging method allows the development of constitutive equations at the macroscopic scale without incorporating microstructure dynamics, this is advantageous in terms of the reduced complexity of the solution.

4.3.1 The Eshelby Inclusion Model

Eshleby [205] proposed an elastic homogenization approach for a two-phase material based on the analysis of the stress-strain relationship for an inclusion of spheroidal or ellipsoidal shape contained within an infinite matrix. The stress and strain distributions are developed by relaxing the material thus generating an elastic response in the inclusion and the matrix. The derivation of the constitutive equations is initially developed for an inclusion which has similar mechanical properties to that of the matrix, this solution is extended to cater for materials in which the material properties for the inclusion and matrix differ substantially. If the inclusion is considered in isolation without the constraint of the surrounding matrix, transformation will result in a change in shape and volume of the inclusion and hence a corresponding strain ε^t. If the constraints imposed by the matrix are taken into account then stress will be generated within the inclusion in order to maintain its original shape. The resultant stress in the inclusion, σ^i, will be proportional to the deviation of the transformed inclusion from its original shape.

$$\sigma^i_{ij} = C_{ijkl}\left(\varepsilon^c_{kl} - \varepsilon^t_{kl}\right) \tag{4.37}$$

or in matrix notation

$$\sigma^i = \mathrm{C}(\varepsilon^c - \varepsilon^t) \tag{4.38}$$

where ε^c is the strain imposed by the surrounding matrix in order to maintain the original shape of the inclusion. C is the fourth-order elasticity tensor for the material. If the macroscopic stress and strain are assumed to approach zero at an

infinite distance from the inclusion then the general form for the imposed strain as proposed by Mura [206] and Indenbom and Lothe [207] may be written as

$$\varepsilon_{ij}^{c} = D_{ijkl}\, \varepsilon_{kl}^{t} \tag{4.39}$$

or

$$\boldsymbol{\varepsilon}^{c} = \mathbf{D}\, \boldsymbol{\varepsilon}^{t} \tag{4.40}$$

where $\mathbf{D}$ is a fourth-order elastic tensor. A analytical solution was derived by Eshelby using Hookes law, stress equilibrium and strain compatibility. The solution implies that the components of $\mathbf{D}$ may be specified in terms two parameters, α and β, that define the proportionality between the dilational and deviatoric strain components

$$\begin{aligned} \varepsilon^{c\ dil} &= \alpha \varepsilon^{t\ dil} \\ \varepsilon_{ij}^{c\ dev} &= \beta \varepsilon_{ij}^{t\ dev} \end{aligned} \tag{4.41}$$

The strains $\varepsilon^{c\ dil}$ and $\varepsilon^{t\ dil}$ are the scaler dilational components given by

$$\begin{aligned} \varepsilon^{c\ dil} &= \frac{\varepsilon_{ii}^{c}}{3} \\ \varepsilon^{t\ dil} &= \frac{\varepsilon_{ii}^{t}}{3} \end{aligned} \tag{4.42}$$

and $\varepsilon_{ij}^{c\ dev}$ and $\varepsilon_{ij}^{t\ dev}$are the deviatoric components

$$\begin{aligned} \varepsilon_{ij}^{c\ dev} &= \varepsilon_{ij}^{c} - \varepsilon^{c\ dil}\delta_{ij} \\ \varepsilon_{ij}^{t\ dev} &= \varepsilon_{ij}^{t} - \varepsilon^{t\ dil}\delta_{ij} \end{aligned} \tag{4.43}$$

δ_{ij} is the Kronecker delta and is defined as

$$\begin{aligned} \delta_{ij} &= 1 \qquad i = j \\ \delta_{ij} &= 0 \qquad i \neq j \end{aligned} \tag{4.44}$$

The proportionality parameters α and β are given as

$$\begin{aligned} \alpha &= \left(\frac{1}{3}\right)\left(\frac{1+\nu}{1-\nu}\right) \\ \beta &= \left(\frac{1}{15}\right)\left(\frac{4-5\nu}{1-\nu}\right) \end{aligned} \tag{4.45}$$

Eshelby demonstrated that the above solution may be extended to cater for the case where the inclusion and matrix have dissimilar properties and the material is under load. In effect a solution may be obtained by reducing the problem such that the body consisting of matrix with inhomogeneous inclusion is replaced with an unbounded matrix and a transformed inclusion with the same properties as that of the matrix. This approach implies that an equivalent transformation strain should be derived such that it corresponds with the strain field of the inhomogeneous inclusion

$$\varepsilon_{ij}^{t} = D'_{ijkl}\varepsilon_{kl}^{m} \tag{4.46}$$

or

$$\boldsymbol{\varepsilon}^{t} = \mathbf{D}'\boldsymbol{\varepsilon}^{m} \tag{4.47}$$

where $\mathbf{D}'$ is a fourth-order elastic tensor and $\boldsymbol{\varepsilon}^{m}$ is the strain tensor for the matrix. As previously, the components of $\mathbf{D}'$ may be defined in terms two proportionality parameters, α' and β', such that

$$\begin{aligned} \varepsilon^{t\ dil} &= \alpha'\varepsilon^{m\ dil} \\ \varepsilon_{ij}^{t\ dev} &= \beta'\varepsilon_{ij}^{m\ dev} \end{aligned} \tag{4.48}$$

where the dilational strain components are given by

$$\begin{aligned} \varepsilon^{t\ dil} &= \frac{\varepsilon_{ii}^{t}}{3} \\ \varepsilon^{m\ dil} &= \frac{\varepsilon_{ii}^{m}}{3} \end{aligned} \tag{4.49}$$

and the deviatoric components by

$$\begin{aligned} \varepsilon_{ij}^{e\ dev} &= \varepsilon_{ij}^{e} - \varepsilon^{e\ dil}\delta_{ij} \\ \varepsilon_{ij}^{m\ dev} &= \varepsilon_{ij}^{m} - \varepsilon^{m\ dil}\delta_{ij} \end{aligned} \tag{4.50}$$

In this case the proportionality parameters α' and β' are the given as

$$\begin{aligned} \alpha' &= \frac{\kappa^{i} - \kappa^{m}}{\left(\kappa^{m} - \kappa^{i}\right)\alpha - \kappa^{m}} \\ \beta' &= \frac{\mu^{i} - \mu^{m}}{\left(\mu^{m} - \mu^{i}\right)\beta - \mu^{m}} \end{aligned} \tag{4.51}$$

where κ^i and κ^m are bulk moduli for the inclusion and matrix respectively and μ^i and μ^m are the Lamé constants for the inclusion and matrix respectively. α and β are calculated as shown previously in equation (4.45). The true inclusion strain can be calculated by substitution of the equivalent transformation strain given by equation (4.47) into equation (4.40) so that

$$\varepsilon^c = \mathbf{D}\,\mathbf{D}'\varepsilon^m = \mathbf{D}^*\varepsilon^m \tag{4.52}$$

The transformation strain may be given in terms of the imposed strain using equation (4.40)

$$\varepsilon^t = \mathbf{D}^{-1}\varepsilon^c \tag{4.53}$$

and the stress in the inclusion may be obtained by substitution of the transformation stress into equation (4.37)

$$\sigma^i = \mathbf{C}\left(\varepsilon^c - \mathbf{D}^{-1}\varepsilon^c\right) = \mathbf{C}\left(\mathbf{I} - \mathbf{D}^{-1}\right)\varepsilon^c \tag{4.54}$$

where $\mathbf{I}$ is a fourth-order unit tensor. For the case where the stress and strain fields tend to zero at an infinite distance from the inclusion the stress in the inclusion is given as

$$\sigma^i = \mathbf{C}\left(\mathbf{I} - \mathbf{D}^{-1}\right)\varepsilon^i \tag{4.55}$$

where $\varepsilon^c = \varepsilon^i$. If the stress and strain fields at an infinite distance from the inclusion are non-zero then above equation is simply modified

$$\sigma_i - \sigma^m = -\mathbf{L}\left(\varepsilon^i - \varepsilon^m\right) \tag{4.56}$$

where $\mathbf{L}$ is referred to as the interaction tensor and is given as

$$\mathbf{L} = -\mathbf{C}\left(\mathbf{I} - \mathbf{D}^{-1}\right) \tag{4.57}$$

4.3.2 The Stringfellow Constitutive Model

The constitutive model described by Stringfellow et. al. [198, Stringfellow] for the modelling of the stress-strain behaviour of TRIP steels is essentially an extension

of the Eshelby inclusion model as described above, in this case the model is based on a generalised treatment of an evolving two-phase composite material undergoing large, finite deformation. More specifically the model is formulated to address the following observations as evidenced during testing of TRIP steels [208].

1. Each phase is strain-hardening and exhibits different hardening parameters. This leads to a correspondingly large difference between the average plastic strains for each phase.

2. The evolution of the martensite phase is strongly dependent on temperature, the stress state, plastic strain and the plastic strain rate [199].

3. The phase transformation results in a so-called transformation strain due to a shape strain and a positive volume change.

4. The martensite phase formed at high levels of plastic strain is harder than that formed at lower levels of plastic strain due to the observation that the transformed martensite phase inherits the dislocation sub-structure of the parent austenite phase.

The resultant constitutive model therefore focuses on the prediction of the stress-strain behaviour based on the influence of both the strain hardening due to the evolution of martensite and the strain softening that results from the transformation mechanism. A primary feature of the model is the use of the Eshelby model, as described previously, to apportion the plastic strain between the two phases.

Rate constitutive formulation

The evolution of the stress state in the two-phase material is based on an isotropic hypoelastic formulation and the rate kinematics on which the formulation is based are expressed using a finite deformation formulation based on the use of the Juamann-Zaremba stress rate

$$\overset{\nabla}{\mathrm{T}} = \dot{\mathrm{T}} + \dot{\omega}\mathrm{T} - \mathrm{T}\dot{\omega} \tag{4.58}$$

where $\mathbf{T}$ is the stress in the current configuration (Kirchhoff stress) and $\dot{\omega}$ is the vorticity tensor which is the skew-symmetric portion of the rate of deformation (velocity gradient) tensor. The total strain-rate may be considered in terms of an additive form containing the elastic strains $\dot{\varepsilon}^e$ and plastic strains $\dot{\varepsilon}^p$,i.e.

$$\dot{\varepsilon} = \dot{\varepsilon}^e + \dot{\varepsilon}^p \tag{4.59}$$

It has been shown that a hypoelastic formulation is a suitable approximation to the hyperelastic form if the elastic strain-rates are small [209] and, assuming that the martensite and austenite phases have similar elastic properties, the stress-rate may by described by

$$\overset{\nabla}{\mathbf{T}} = \mathbf{C}(\dot{\varepsilon} - \dot{\varepsilon}^p) \tag{4.60}$$

where $\mathbf{C}$ is the isotropic elasticity tensor for the two phase material. The elasticity tensor may be expressed in terms of the shear modulus G and the bulk modulus K as

$$\mathbf{C} = 2G\,\mathbf{I} + \left(K - \frac{2}{3}G\right)(\mathbf{1} \otimes \mathbf{1}) \tag{4.61}$$

$\mathbf{I}$ and $\mathbf{1}$ are used to represent fourth-order and second-order unit tensors respectively.

The total strain rate may be decomposed into the deviatoric and dilational parts

$$\dot{\varepsilon} = \dot{\varepsilon}^{dev} + \dot{\varepsilon}^{dil} \tag{4.62}$$

$$= \dot{\varepsilon}^{dev} + \tfrac{1}{3}(\mathrm{tr}\ \dot{\varepsilon})\mathbf{1} \tag{4.63}$$

If an equivalent total shear strain-rate $\dot{\gamma}^t$ and dilation rate $\dot{e}_v$ are defined as

$$\dot{\gamma}^t = \sqrt{2}\,\|\dot{\varepsilon}^{dev}\| \tag{4.64}$$

$$\dot{e}_v = \tfrac{1}{3}(\mathrm{tr}\ \dot{\varepsilon}) \tag{4.65}$$

then the total strain rate may be written as

$$\dot{\varepsilon} = \frac{1}{\sqrt{2}}\dot{\gamma}^t\mathbf{M} + \dot{e}_v\mathbf{1} \tag{4.66}$$

The tensor $\mathbf{M}$ is a unit tensor coaxial with the deviatoric strain-rate, i.e.

$$\mathbf{M} = \frac{\dot{\varepsilon}^{dev}}{\|\dot{\varepsilon}^{dev}\|} \tag{4.67}$$

The plastic strain-rate can be decomposed in a similar manner into deviatoric and dilational parts

$$\dot{\varepsilon}^p = \dot{\varepsilon}^{p\ dev} + \dot{\varepsilon}^{p\ dil} \tag{4.68}$$

$$= \dot{\varepsilon}^{p\ dev} + \tfrac{1}{3}(\mathrm{tr}\ \dot{\varepsilon}^p)\mathbf{1} \tag{4.69}$$

and by defining an equivalent plastic shear strain-rate $\dot{\gamma}^p$ and plastic dialation rate $\dot{e}_v^p$ as

$$\dot{\gamma}^p = \sqrt{2}\,\|\dot{\varepsilon}^p\| \tag{4.70}$$

$$\dot{e}_v^p = \tfrac{1}{3}(\mathrm{tr}\ \dot{\varepsilon}^p) \tag{4.71}$$

the plastic strain-rate can be written as

$$\dot{\varepsilon}^p = \frac{1}{\sqrt{2}}\dot{\gamma}^p\mathbf{N} + \dot{e}_v^p\mathbf{1} \tag{4.72}$$

The tensor $\mathbf{N}$ is a unit tensor taken to be coaxial with the plastic strains which in turn are assumed to be coaxial with the deviatoric stresses, this implies that

$$\mathbf{N} = \frac{\mathbf{S}}{\|\mathbf{S}\|}$$

The bulk stress $\bar{\sigma}$ and the equivalent shear stress $\bar{\tau}$ are defined as scalar invariants of the Cauchy stress tensor $\mathbf{T}$ as

$$\bar{\sigma} = -\frac{1}{3}\,tr\ \mathbf{T} \tag{4.73}$$

$$\bar{\tau} = \sqrt{\tfrac{1}{2}\mathbf{S}\cdot\mathbf{S}} \tag{4.74}$$

and therefore the rate forms of the bulk stress and the equivalent shear stress are given by

$$\dot{\bar{\sigma}} = -\tfrac{1}{3}\overset{\nabla}{\mathbf{T}}\cdot\mathbf{1} = -\,K(\dot{e}_v^t - \dot{e}_v^p) \tag{4.75}$$

$$\dot{\bar{\tau}} = \tfrac{1}{\sqrt{2}}\overset{\nabla}{\mathbf{T}}\cdot\mathbf{N} = G(\beta\dot{\gamma}^t - \dot{\gamma}^p) \tag{4.76}$$

The equivalent shear stress and pressure rates are expressed in terms of the martensite transformation parameters by linking the plastic strain and dilation rates with the transformation variables. In order to facilitate this the plastic strain rate is decomposed further into a combination of strains resulting from slip in the material and an additional inelastic strain rate resulting from the transformation process.

$$\dot{\varepsilon}^p = \dot{\varepsilon}^{slip} + \dot{\varepsilon}^{trans} \tag{4.77}$$

Transformation strain

Stringfellow et. al. used a similar method to that proposed by Hutchinson and Tvergaard [210] to account for the strain softening observed as a result of the martensite transformation process. This involved the introduction of an additional inelastic transformation strain-rate term which is correlated with shape-strain coaxial with the unit deviatoric tensor **N** and the volume change associated with the transformation, Δ_v. The transformation strain-rate therefore has the following form

$$\dot{\varepsilon}^{trans} = \dot{f}\left(\frac{1}{\sqrt{2}}A\mathbf{N} + \frac{1}{3}\Delta_v \mathbf{1}\right) \tag{4.78}$$

where A is a dimensionless parameter accounting for the net shape-strains coaxial with **N** [211]. Based on experimental observation, the parameter A is calculated as follows

$$A = A_0 + A_1\left(\frac{\bar{\tau}}{s_a}\right) \tag{4.79}$$

where A_0 and A_1 are constants and s_a is a reference value for the hardness of the austenite phase.

Deviatoric plastic strain-rate

The equivalent deviatoric plastic strain-rate may be defined as

$$\dot{\gamma}^{slip} = \sqrt{2}\frac{\dot{\varepsilon}^{slip}}{\left\|\dot{\varepsilon}^{slip}\right\|} \tag{4.80}$$

and may be considered as a simple combination of additive strains resulting from the two phases as follows

$$\dot{\gamma}^{slip} = f\,\dot{\gamma}_m + (1-f)\,\dot{\gamma}_a \tag{4.81}$$

The equivalent plastic shear strain-rate may then be written as

$$\dot{\gamma}^{p} = f\,\dot{\gamma}_m + (1-f)\,\dot{\gamma}_a + A\dot{f} \tag{4.82}$$

The relationship between the equivalent shear stress and the equivalent shear strain-rate for each phase is assumed have the form

$$\tau_i = \mu_i \dot{\gamma}_i \tag{4.83}$$

It is also assumed that the macroscopic behaviour for the two phase material may be described in the same way i.e.

$$\bar{\tau} = \mu_i \dot{\bar{\gamma}}^p \tag{4.84}$$

The local and global stresses within the two phases are expressed using Eshelby's solution

$$\dot{\gamma}_i = \frac{5\bar{\mu}}{3\bar{\mu} + 2\mu_i} \dot{\bar{\gamma}}^p \tag{4.85}$$

$$\tau_i = \frac{5\mu_i}{3\bar{\mu} + 2\mu_i} \bar{\tau} \tag{4.86}$$

Equation (4.82) may be rewritten as

$$f\chi_m + (1-f)\chi_a + A\chi_f = 1 \tag{4.87}$$

by letting

$$\chi_m = \frac{\dot{\gamma}_m}{\dot{\bar{\gamma}}^p} \tag{4.88}$$

$$\chi_a = \frac{\dot{\gamma}_a}{\dot{\bar{\gamma}}^p} \tag{4.89}$$

$$\chi_f = \frac{\dot{f}}{\dot{\bar{\gamma}}^p} \tag{4.90}$$

The relationship between the local and global shear strain-rates given by equation may also be rewritten as

$$\chi_i \left(\frac{3}{5} + \frac{2\mu_i}{5\bar{\mu}} \right) = 1 \tag{4.91}$$

The viscoplastic relationship between the shear stress and shear strain in each phase is assumed to have the following power-law form

$$\dot{\gamma}_i = \left(\frac{\tau_i}{s_i} \right)^M \dot{\gamma}_0 \tag{4.92}$$

where s is a reference shear strength level and $\dot{\gamma}_0$ a reference shear strain-rate. The two phase material is also assumed to behave according to the same model, i.e.

$$\dot{\bar{\gamma}}^p = \left(\frac{\bar{\tau}}{\bar{s}} \right)^M \dot{\gamma}_0 \tag{4.93}$$

4.3.3 The Tomita-Iwamoto Constitutive Models

As with the Stringfellow model the plastic strain rate is assumed to be the sum of the plastic strain rate induced by slip deformation in the two phase material and the plastic strain rate induced by the transformation [201]. In addition the transformation strain rate can be separated into deviatoric and dilational components. As with the previous model the deviatoric component is assumed to be coaxial with the deviatoric stress. The deviatoric component is given as

$$\dot{\varepsilon}_{ij}^{p\ dev} = \sqrt{\frac{3}{2}} R\ \dot{f}^m n_{ij} \tag{4.94}$$

where

$$n_{ij} = \frac{\sigma'_{ij}}{\sqrt{\frac{2}{3}}\bar{\sigma}} \tag{4.95}$$

and

$$R = R_0 + R_1 \left(\frac{\bar{\sigma}}{\sigma_y^a} \right) \tag{4.96}$$

The dilational component is expressed in terms of the volume change accompanying the transformation

$$\dot{\varepsilon}_{ij}^{p\ dil} = \frac{1}{3} \Delta v \dot{f}^m \delta_{ij} \tag{4.97}$$

The plastic strain rate is derived using the work-equivalent measure of the representative plastic strain rate and is given as

$$\dot{\varepsilon}_{ij}^{p} = p_{ij} \dot{\bar{\varepsilon}}^p + s_{ij} \Delta v \dot{f}^m \tag{4.98}$$

where

$$p_{ij} = \frac{3\sigma'_{ij}}{2\bar{\sigma}} \tag{4.99}$$

$$s_{ij} = -p_{ij}\Sigma + \frac{\delta_{ij}}{3} \tag{4.100}$$

$$\dot{\bar{\varepsilon}}^p = \dot{\bar{\varepsilon}}^{p\ slip} + R\ \dot{f}^m + \Sigma \Delta v \dot{f}^m \tag{4.101}$$

The apportionment of the plastic strains between the two phases is carried out as described by Stringfellow et. al. using a modified for of Eshelby's inclusion approach. The thermoelastic constitutive equation is assumed to be [212]

$$\varepsilon_{ij}^e = B_{ijkl}^e(T)\ \sigma_{kl} + \alpha \delta_{ij}(T - T_0) \tag{4.102}$$

The rate form of the equation is given by

$$\dot{\varepsilon}^e_{ij} = B^e_{ijkl}(T)\ \dot{\sigma}_{kl} + \alpha_{ij}\dot{T} \tag{4.103}$$

where

$$\alpha_{ij} = \alpha\delta_{ij} - \frac{1}{E^2}\frac{\partial E}{\partial T}\left\{(1-\nu)\,\sigma_{ij} - \nu\ \delta_{ij}\ \sigma_{\max}\right\} \tag{4.104}$$

The inverse relation gives the stress rate

$$\dot{\sigma}_{ij} = D^e_{ijkl}\ \dot{\varepsilon}^e_{kl} - \beta_{ij}\dot{T} \tag{4.105}$$

where

$$\beta_{ij} = \frac{\alpha E}{1-2\nu}\delta_{ij} - \frac{1}{E}\frac{\partial E}{\partial T}\ \sigma_{ij} \tag{4.106}$$

Introducing the plastic strains into the constitutive equations results in

$$\overset{\nabla}{S}_{ij} = D^e_{ijkl}\ (\dot{\varepsilon}_{kl} - \ \dot{\varepsilon}^p_{kl}) - \beta_{ij}\dot{T} \tag{4.107}$$

substituting for the plastic strains

$$\overset{\nabla}{S}_{ij} = D^e_{ijkl}\ \dot{\varepsilon}_{kl} - \beta_{ij}\dot{T} - P_{ij}\dot{\bar{\varepsilon}}^p - (Q_{ij} - \sigma_{ij})\,\Delta v\dot{f}^m \tag{4.108}$$

where

$$\beta_{ij} = \frac{\alpha E}{1-2\nu}\delta_{ij} \tag{4.109}$$

$$P_{ij} = 3G\frac{\sigma'_{ij}}{\bar{\sigma}} \tag{4.110}$$

$$Q_{ij} = -p_{ij}\Sigma + \frac{\delta_{ij}}{3}\left(\frac{E}{1-2\nu}\right) \tag{4.111}$$

It was also proposed that a heat conduction equation be used to account for the latent heat due to transformation [200]

$$\rho C\dot{T} = \sigma_{ij}\dot{\varepsilon}^p_{ij} + \kappa\nabla^2 T - \rho l_m\dot{f}^m \tag{4.112}$$

To account for the difference between the uniaxial tension and compression curves for TRIP steels the equivalent stress is modified

$$f(J_2, J_3) = J_2 - \kappa\frac{J_3}{J_2^{1/2}} - \frac{1}{3}\bar{\sigma}^2 = 0 \tag{4.113}$$

where

$$J_2 = \frac{1}{2}\sigma'_{ij}\sigma'_{ij} \tag{4.114}$$

$$J_3 = \det\ \sigma'_{ij} \tag{4.115}$$

The parameter κ reflects the development of the microstructure and texture of the material. An evolution equation is proposed by Miller and McDowell [213]

$$\dot{\kappa} = C_k(1-\kappa)\dot{\bar{\varepsilon}}^{p\ slip} \tag{4.116}$$

This implies that the equivalent stress is expressed as

$$\bar{\sigma} = \sqrt{3\left(J_2 - \kappa\frac{J_3}{\sqrt{J_2}}\right)} \tag{4.117}$$

This modified form results in

$$p_{ij} = \frac{3}{2\bar{\sigma}}\frac{\partial f}{\partial \sigma_{ij}} \tag{4.118}$$

Chapter 5

Mechanical-Magnetostatic Response Modelling Examples

5.1 Introduction

The methodology involved in predicting the mechanical and corresponding magnetostatic response of TRIP steel components and structures was divided into two phases. The first phase involved the simulation of the martensite transformation as a function of applied loading, i.e. establishing the location and amount of transformed material. This was determined using a finite element model incorporating the transformation kinetics and constitutive equations as described previously. The finite element analyses were implemented as non-linear material models using an updated kinematic formulation based on the procedures discussed in Chapter 3. The martensite volume fraction was determined for each load increment as a function of the stress and strain increments for input into the magnetostatic model. Once the location and amount of transformed material was known a second finite element model was created, this being the magnetostatic model. The magnetostatic model was formulated to included the measurement elements and the magnetic permeability of the TRIP steel was adjusted for each load increment according to the

amount of transformed material present for any given location within the TRIP steel component. The magnetostatic models were analysed using a linear formulation as discussed in Chapter 3.

In order to demonstrate the application of the numerical modelling methodology, two test-cases are presented. The tests-cases are derived from practical real-world examples of peak strain sensors that are currently under development. The aim of the analyses described here was to provide predications of the electrical response characteristics of the peak strain sensors as a function of mechanical loading.

The first test-case involves the prediction of the response of a sensor element used within so-called passive strain monitors [100]. These monitors are designed to provide simple non-destructive strain measuring systems for evaluating structural integrity or damage for a wide range of structures. The passive monitors are used to evaluate local material condition at specific points by attaching the monitor such that it straddles the region of interest as illustrated in figure 5.1. Typically, the monitor is situated parallel to the high stress direction or at an angle with respect to a multiaxial stress coordinate system. Displacement between the attachment points is correlated with the peak strain measured which is in turn derived from the amount of martensite transformation within the TRIP steel sensor element. Measurement of the transformation is achieved using an inductance bridge which essentially consists of a pair of identical current carrying coils with the sensor element placed along the center of one of the coils, the other coil is used to compensate for temperature effects. Transformation of the TRIP steel sensor element will cause a change in permeability and hence a change in the inductance of the measurement coil which

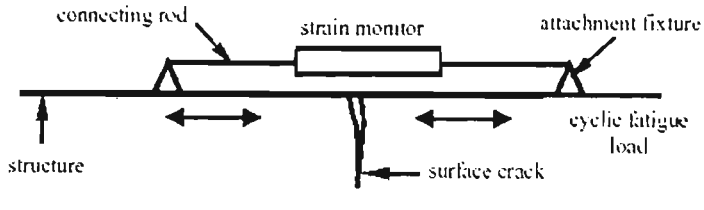

Figure 5.1: Strain monitor attachment

is calculated by monitoring the balance of the inductance bridge. The behaviour of the sensor element is investigated as a function of enforced displacement and is also evaluated for a range of temperatures.

The second test-case addresses the performance evaluation of dual-function engineering components [9], in this case an aircraft bolt. Dual function components are a natural consequence of TRIP steels as they were originally developed as structural materials and can be used to fabricate high strength engineering components, dual function components are therefore designed to act as both load carrying component and sensor simultaneously. A proposal is currently being considered to replace the steel bolts used to mount the wings of a C-130 transport aircraft to the fuselage with alternatives manufactured using high-strength TRIP steel. The motivation for the proposal is primarily concerned with the costs associated with the periodic removal of the bolts for inspection and crack detection. The inspection procedure requires removal of the aircraft from service and approximately 200 man-hours for the removal of the wing attachment bolts [10]. The development a smart wing bolt that would be capable of sensing its deformation state without the labour intensive inspection procedures presents a simple cost-effective solution to the problem. The strain sensing methodology is similar to that used for the passive strain monitor described above in that strain is correlated with the amount of material transformation using an induction coil. The position and orientation of the induction coil is critical as transformation is localised to areas of high stress. Results are presented for two coil locations and for a range of temperatures, further results are presented for a modified bolt designed to induce localised transformation in the region below the head of the bolt.

5.2 TRIP Steel Sensor Element

5.2.1 Geometry

Sensor Element

The sensor elements used in the peak strain monitors are shaped as thin ribbon tensile specimens as shown in figure 5.2. The relative displacement between the attachment points is transferred by mechanical clamping to the sensor element. As the deformation is localised to the gauge section of the element the gauge length determines the sensitivity of the gauge to the imposed displacement. For the purposes of the analysis the dimensions of the sensor element were specified as per the parameters contained in table 5.1.

Induction coil

In order to gain the greatest sensitivity in the measurement of the changing permeability of the sensor, the sensor element is placed through the coil such that the coil surrounds the gauge length of the sensor element with a clearance of 0.1 mm between the sensor and inner portion of the coil. It was assumed that coil was manufactured to a length of 6.6 mm using 2500 turns of 70 μm diameter copper wire wound on a mandrel with a diameter of 1.6 mm. This results in a coil with an outer diameter of approximately 5.2 mm.

5.2.2 Sensor Material Characterisation

For the purposes of the analysis and due to availability of relevant material data, the material model used for the sensor element is based on the characteristics of 304

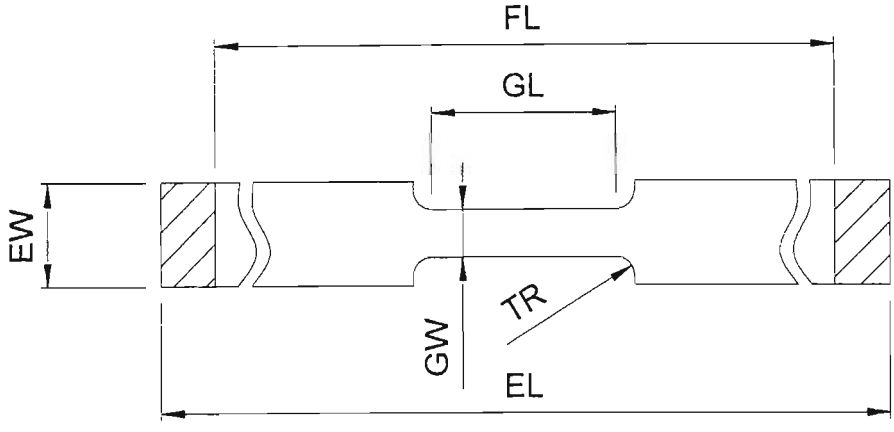

Figure 5.2: TRIP steel sensor element geometry

Parameter	Dimension
Gauge length (GL)	2.54 mm
Gauge width (GW)	0.64 mm
Element length (EL)	70.5 mm
Element width (EW)	1.4 mm
Element thickness (ET)	0.13 mm
Free length (FL)	8.5 mm
Transition radius (TR)	0.254 mm

Table 5.1: Dimensions of sensor element

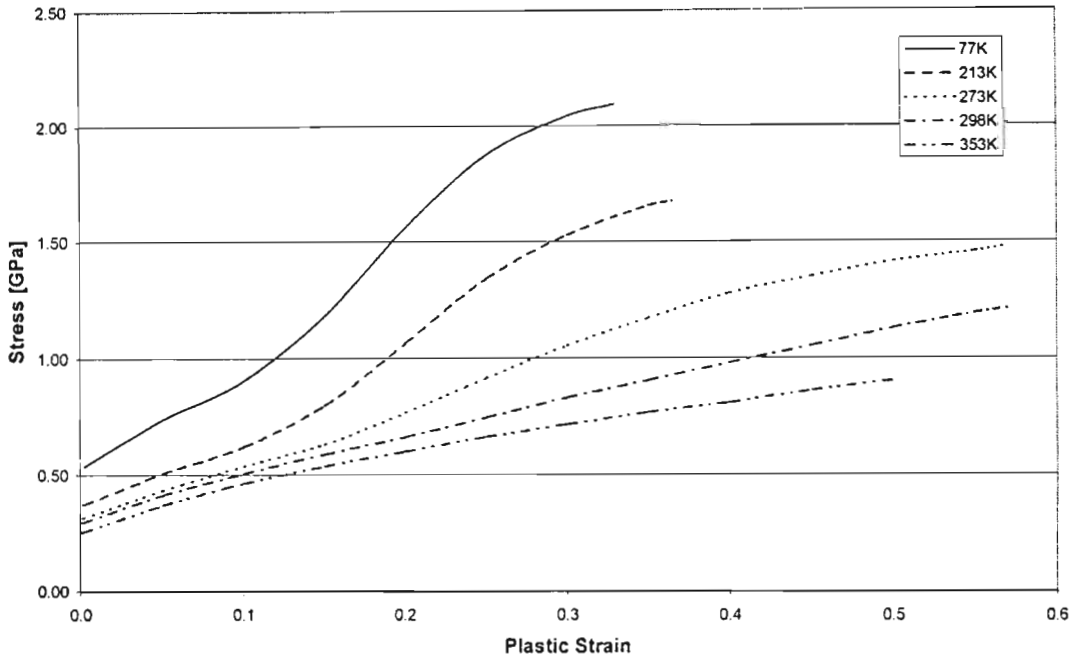

Figure 5.3: The stress - strain relationships for 304 stainless steel at various temperatures [201]

stainless steel. The material is an austenitic steel which undergoes strain-induced martensitic transformation and is therefore classified as a TRIP steel. The relationship between the equivalent material stress $\bar{\sigma}$ and the plastic strain ε^p for 304 stainless steel is shown in figure 5.3 for temperatures of 77 K, 213 K, 273 K, 298 K and 353 K [214].

The evolution of martensite as a function of plastic strain is predicted using the Olson-Cohen model [45] - [47] described earlier which employs only a measure of the plastic strain within the material. The martensite volume fraction in given by

$$f^m = 1 - \exp(-\beta(1 - \exp(-\alpha\varepsilon^p))^n \tag{5.1}$$

where α and β are temperature dependent parameters. The values of α and β used here are those determined through experimentation by Hecker et. al. [199] which were given as follows

	77	213	273	298	353
α	13.040	10.435	7.065	5.000	0.960
β	2.087	2.087	1.939	0.870	0.800

Table 5.2: 304 stainless steel martensite evoluation parameters

The resultant relationships for the martensite volume fraction with respect to plastic strain for a range of temperatures are shown in figure 5.4

5.2.3 Finite Element models

Mechanical response model

The finite element model used to determine the mechanical response of the sensor element when subjected to tensile loading was constructed using plane-stress linear triangular finite elements and is shown in figure 5.5 Tensile loading was applied along the longitudinal axis of the sensor element by loading the right-hand-side vertical edge. Due to the transverse and longitudinal symmetry of the problem, the finite element model is simplified by considering only a quarter of the original domain i.e. the upper right hand side. In addition, due to the physical clamping arrangement, only the portion of the sensor element between the mechanical clamps was modelled.

Magnetostatic response model

The magnetostatic response model used to predict the change in inductance as a function of tensile load is shown in figure 5.6. The model includes the induction coil in addition to the sensor element, both were located in the center of a circular domain used to cater for far-field effects. As with the mechanical response model,

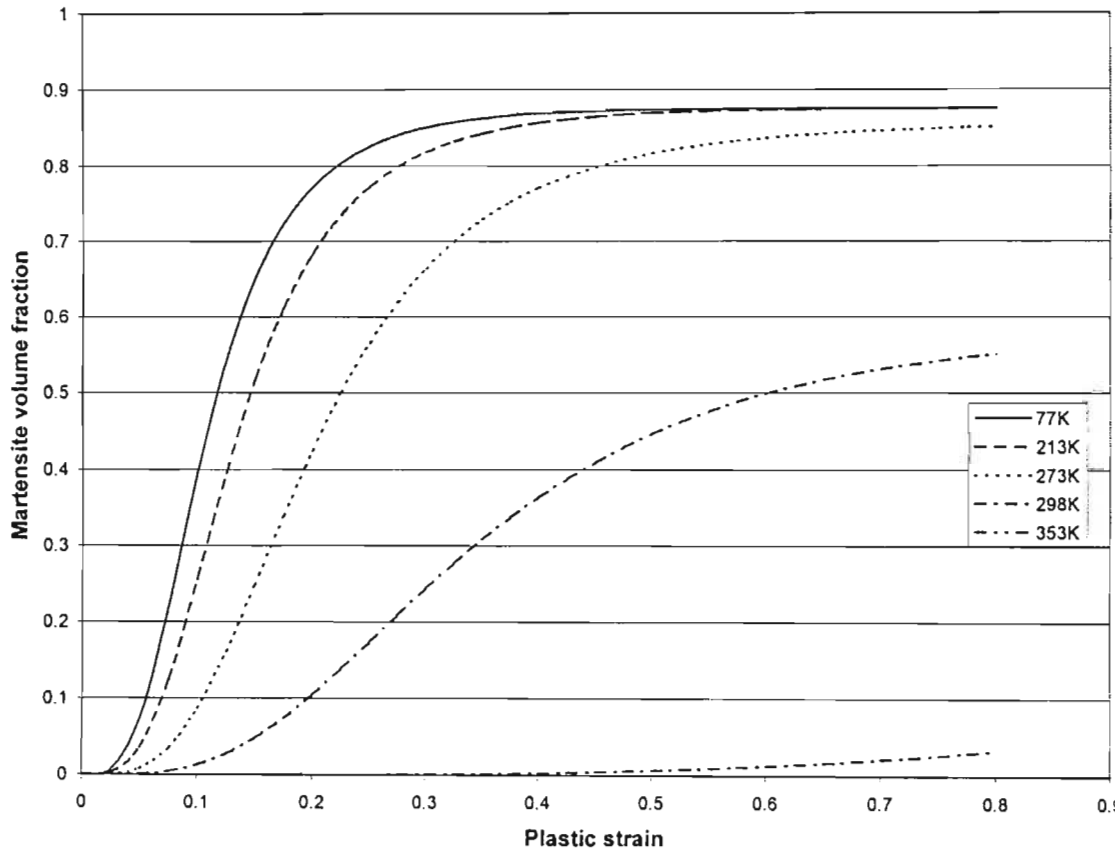

Figure 5.4: The martensite volume fraction as a function of plastic strain for 304 stainless steel at various temperatures

Figure 5.5: Finite element model of TRIP steel sensor element

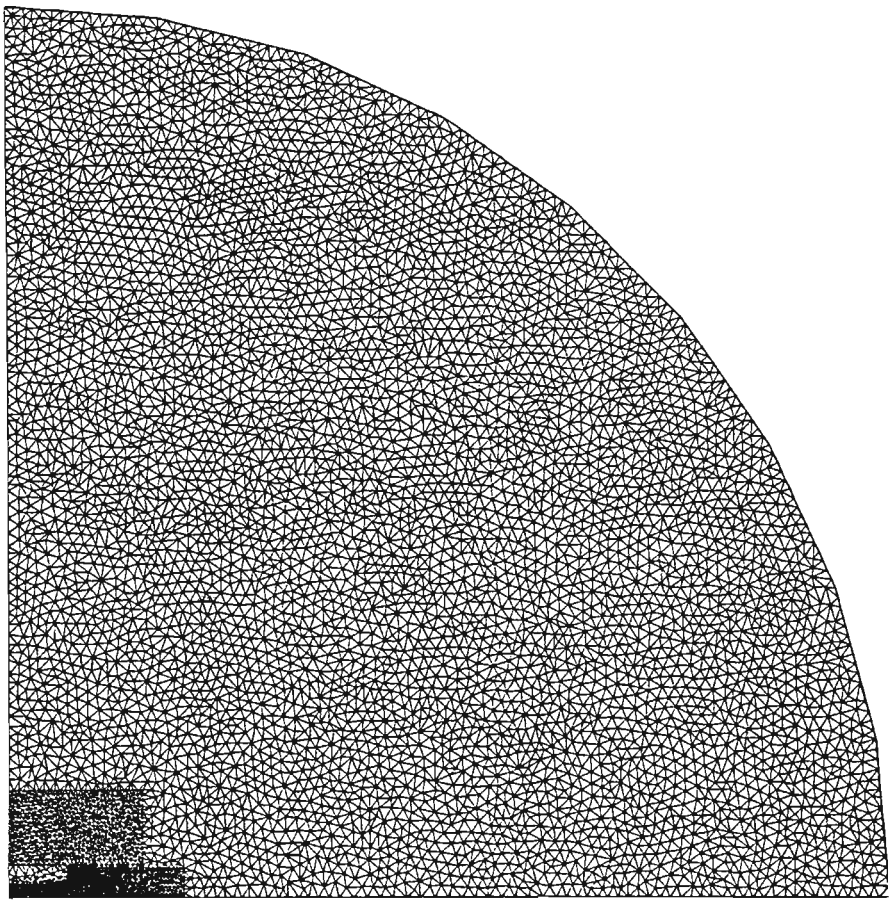

Figure 5.6: Finite element model of sensor element for magnetostatic modelling

the symmetry conditions allow the problem to be reduced to a quarter of the original geometry.

The boundary conditions are specified such that the flux lines do not cross the longitudinal axis of symmetry whilst those crossing the transverse axis do so normal to the vertical axis i.e.

$$A = 0 \quad for \quad y = 0 \tag{5.2}$$

$$\frac{\partial A}{\partial n} = 0 \quad for \quad x = 0 \tag{5.3}$$

where A is the magnetic vector potential. A third boundary condition was used to correct for far-field effects along the outer boundary of the circular domain. This boundary condition was of the mixed type where

$$\left(\frac{1}{\mu_0 \mu_r}\right) \frac{\partial A}{\partial n} + c_o A + c_1 = 0 \tag{5.4}$$

where

$$c_0 = \frac{1}{\mu_0 r} \tag{5.5}$$

$$c_1 = 0 \tag{5.6}$$

μ_0 and μ_r are the permeabilities of air and core material respectively and r is the radius of the domain boundary. The elements within the domain representative of the measurement coil included a current density component J which is arbitrarily specified and is used to calculate the change in coil inductance in response to the change in sensor element permeability. As mentioned previously, the localised permeability of the sensor element material is modified on an incremental basis corresponding to the incremental solution of the mechanical response problem. The inductance for a specific load increment is determined by integrating the product of the magnetic vector potential and the current density over the volume of the induction coil and dividing the result by the current carried by the coil i.e.

$$L = \frac{\int A \cdot J \, dV}{i^2} \tag{5.7}$$

5.2.4 Results and Discussion

The mechanical and corresponding electrical responses for the sensor element were determined for temperatures of 77 K, 213 K, 273 K, 298 K and 353 K. Figure 5.7 shows the predicted change of the coil inductance as a function of the extension of the sensor element for the various temperatures considered. The evolution of the martensite volume fraction and the corresponding changes in flux density and orientation are shown in Figures 5.7a.

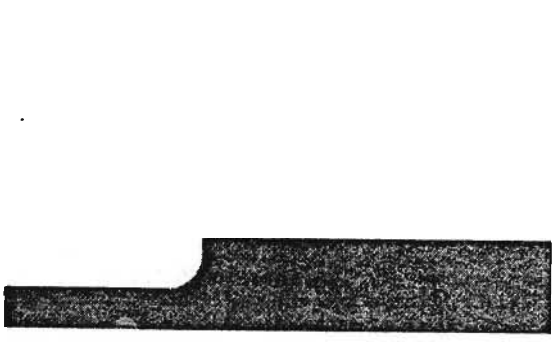

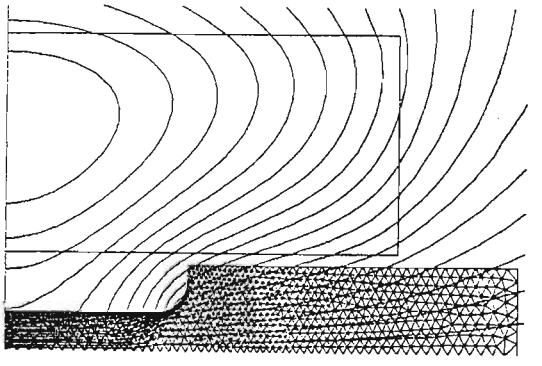

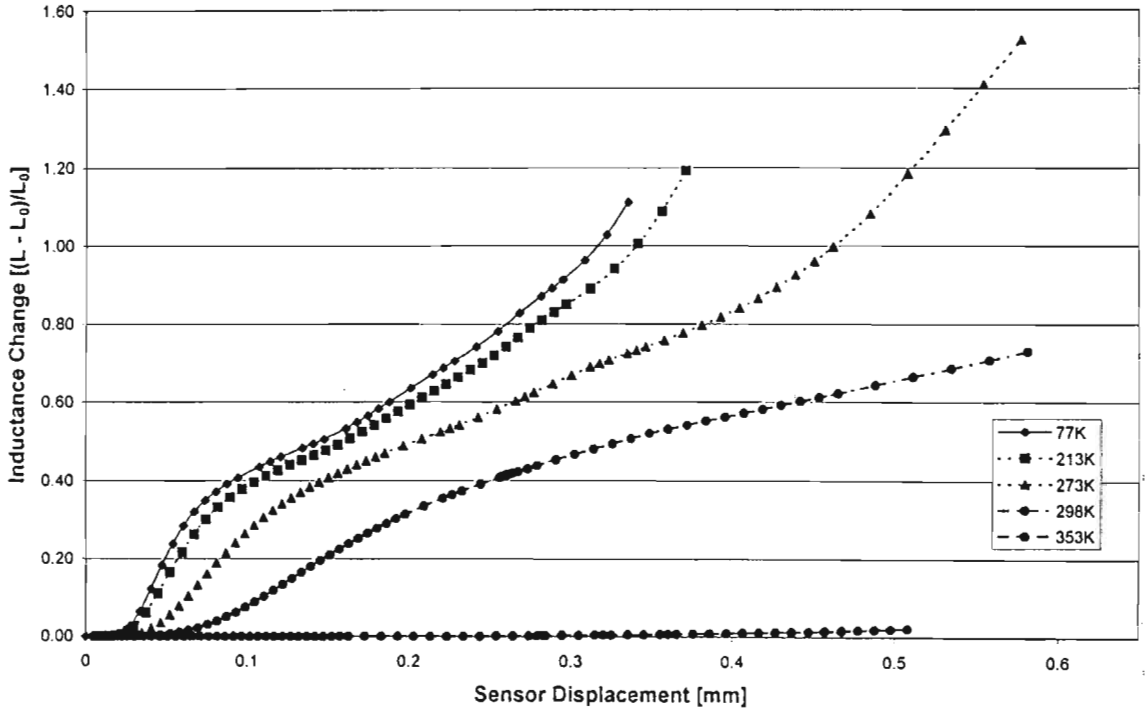

Figure 5.7: Inductance change as a function of sensor displacement at various temperatures

sensor extension = 0.082 mm

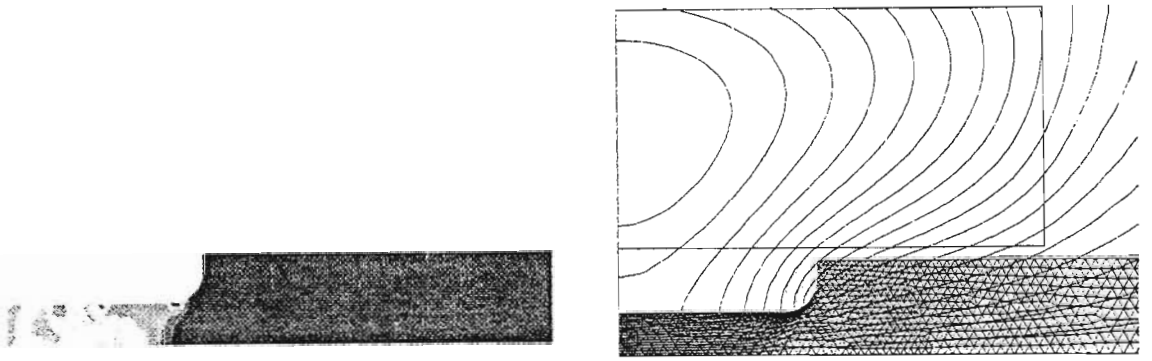

sensor extension = 0.126 mm

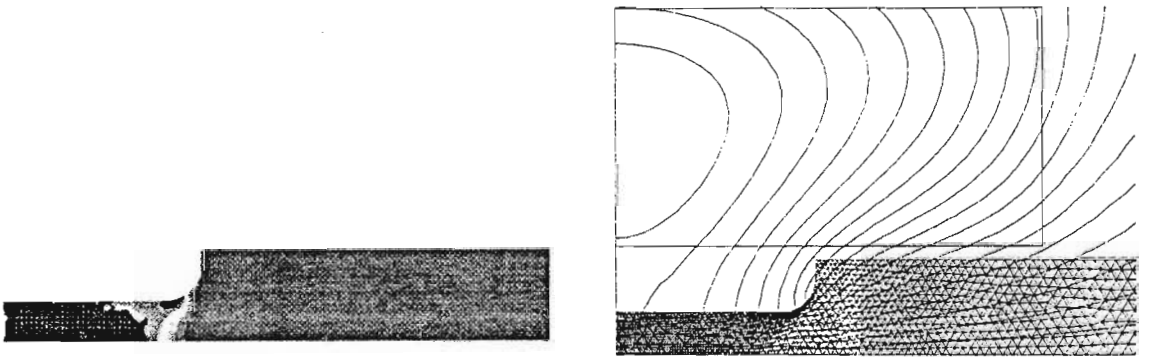

sensor extension = 0.163 mm

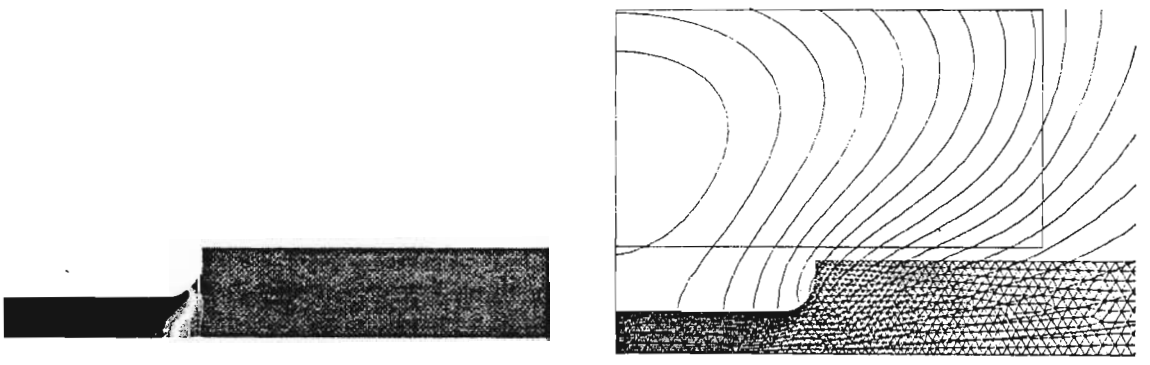

sensor extension = 0.200 mm

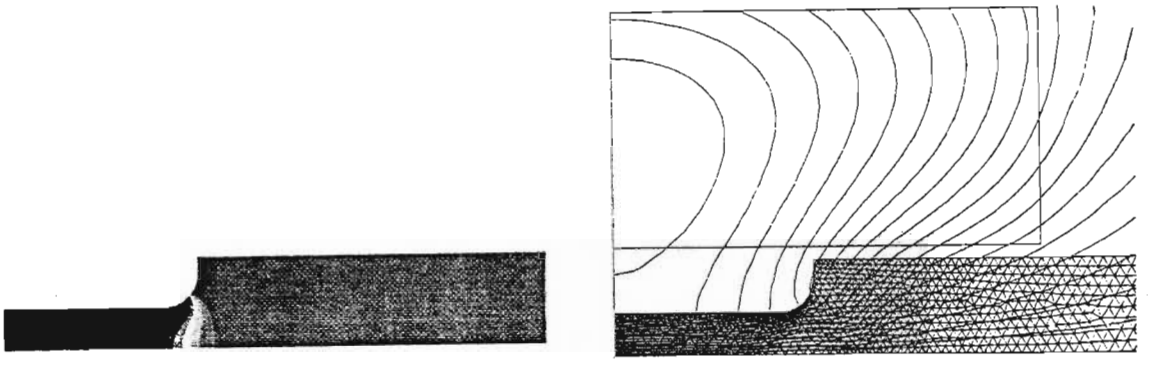

sensor extension = 0.237 mm

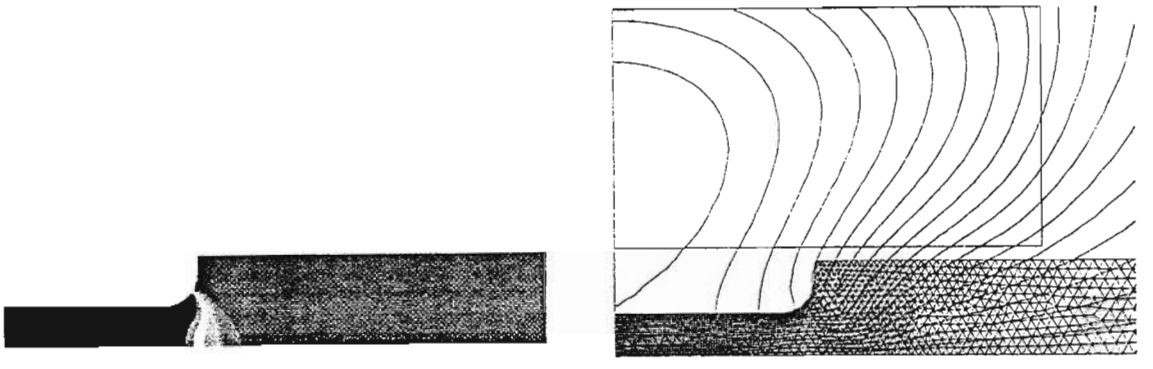

sensor extension = 0.275 mm

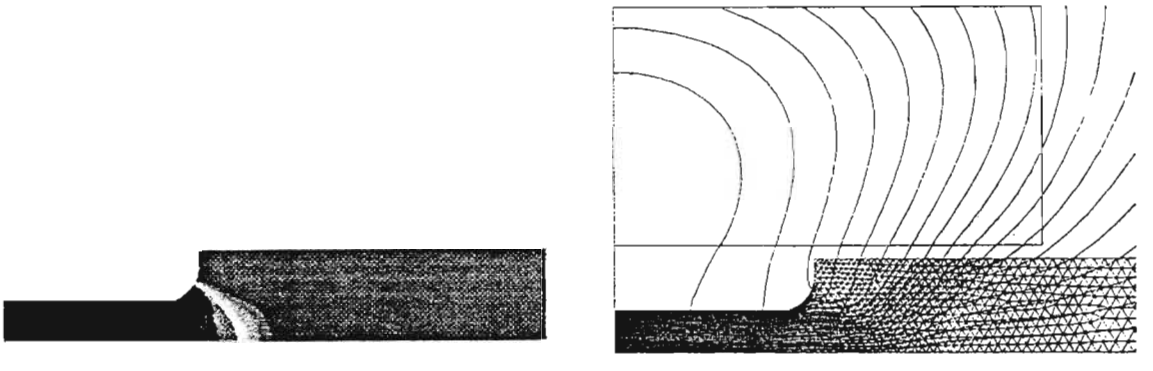

sensor extension = 0.371 mm

Figure 5.7a: Evolution of martensite and the corresponding magnetostatic response for increasing extension

The results of the simulation indicate that the sensor response is strongly dependent on temperature, the response curve at a temperature of 353 K implies that the

sensor is almost unresponsive to strain at this temperature. As the temperature is decreased, the sensor element becomes progressively more responsive, however, the response curve becomes non-linear and it is thought that this is mainly due to the influence of the localised stress concentration at the base of the fillet and the non-linear stress-strain behaviour as shown in figure 5.3. It may be possible to reduce this characteristic by modifying the fillet radius. In addition it was also noted that a distinctive incubation period is required before the change in inductance becomes measurable.

5.3 Aircraft Bolt

5.3.1 Geometry

The aircraft bolt is a simple threaded fastener with geometry as shown in figure 5.8. In order to monitor the change in magnetostatic response, the variation in material permeability was monitored at two locations, the first being in the vicinity of the fillet between the shank and the head of the bolt and the second in the root of the first thread which engages with the nut. In order to improve the sensitivity of the bolt to tensile loading a modified geometry has been proposed which includes a stress concentration feature [104]. In this case the feature takes the form of a groove located under the head of the bolt. The groove increases the stress concentration and hence promotes martensite transformation in a location that favours convenient sensor placement. The magnetostatic response was determined by simulating washer type induction coils placed under the head of the coil and in the vicinity of the first thread.

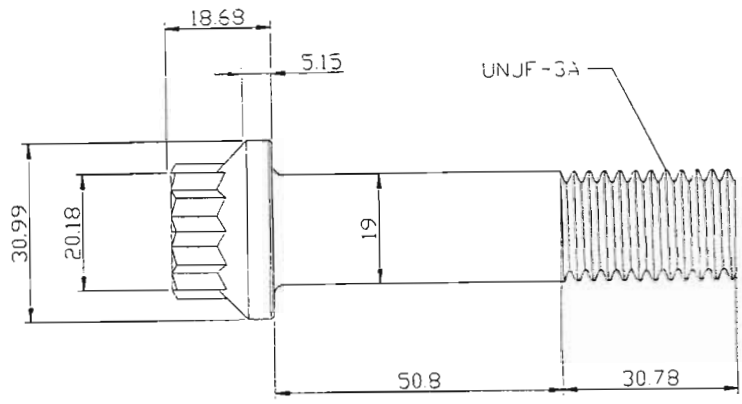

Figure 5.8: Geometry of the aircraft bolt

5.3.2 Material properties

Currently the bolts are manufactured from a high strength steel which does not exhibit transformation characteristics. For the purposes of the analysis the response characteristics are examined for a bolt manufactured from 304 stainless steel with stress-strain and transformation properties as specified in section 5.2.2 above and shown in figures 5.3 and 5.4. It should be noted that the room temperature properties of 304 stainless steel are not suitable for application to the aircraft bolt however the material is used solely to demonstrate the application of the response modelling technique.

5.3.3 Mechanical response model

In order to simplify the modelling of the aircraft bolt, it was assumed that the helical nature of the threads could be neglected. The resultant symmetry enabled the finite element model of the aircraft bolt to be simplified by constructing an axisymmetric model as shown in figure 5.9. The model was constructed using three node triangular axisymmetric elements. The tensile loading was applied under the head of the bolt and constraints were applied to those nodes on the left-hand-side

flanks of the threads to simulate the action of the nut.

5.3.4 Magnetostatic response model

The finite element model of the aircraft bolt used to determine the magnetostatic response is shown in figures 5.10 and 5.11, as with the mechanical model, symmetry of the geometry and the resultant magnetic field enabled simplification of the original domain. The bolt was located in the center of a semi-circular domain to allow for the realistic simulation of far-field effects. As mentioned previously the induction coils were washer shaped and were located under the head of the coil and next to the first thread. The coils had an inner diameter of 12 mm, an outer diameter of 22 mm and a thickness of 3 mm. The boundary conditions were specified such that flux lines did not cross the longitudinal axis of symmetry i.e.

$$A = 0 \quad for \quad r = 0$$

A second boundary condition was used to correct for far field effects along the outer boundary of the circular domain. This boundary condition was of the mixed type where

$$\left(\frac{1}{\mu_0 \mu_r}\right) \frac{\partial A}{\partial n} + c_o A + c_1 = 0$$

where

$$\begin{aligned} c_0 &= \frac{1}{\mu_0 r} \\ c_1 &= 0 \end{aligned}$$

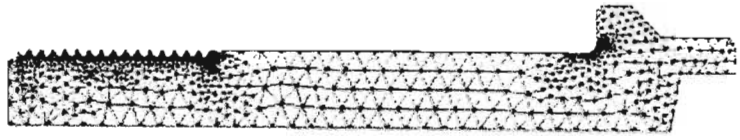

Figure 5.9: Finite element model of the aircraft bolt

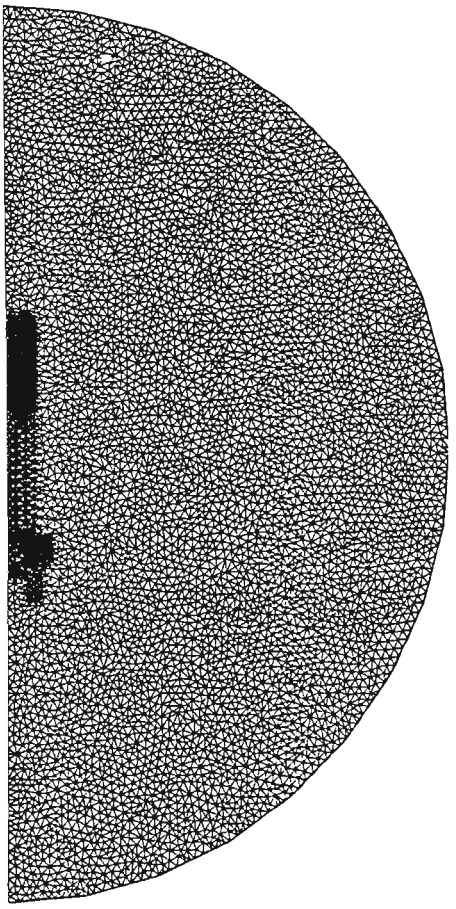

Figure 5.10: Finite element model for magnetostatic analysis of the aircraft bolt

μ_0 and μ_r are the permeabilities of air and core material respectively and r is the radius of the domain boundary. The elements within the domain representative of the measurement coil included a current density component J which was arbitrarily specified and was used to calculate the change in coil inductance in response to the change in bolt material permeability. The localised permeability of the bolt material was modified on an incremental basis corresponding to the incremental solution of the mechanical response problem which was solved earlier. The change is inductance was calculated by evaluating the integral of the current and field strength in the coil as follows

$$L = \frac{\int AJ \, dV}{i^2}$$

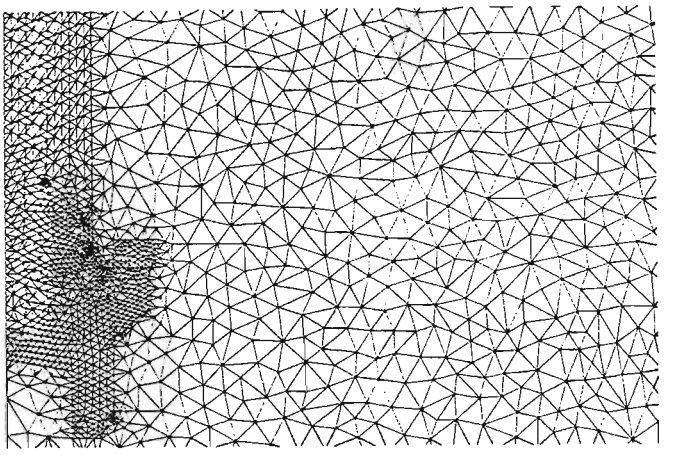

Figure 5.11: Detailed view of the megnetostatic response model of the aircraft bolt.

5.3.5 Results and Discussion

Temperature effects

The response of the bolt when subjected to tensile loading under various temperatures is shown in figure 5.12. The evolution of martensite and the corresponding magnetostatic results are shown in figure 5.14.

It is clear that the magnetostatic response is highly dependent on temperature and therefore the bolt may indicate different peak strain values for similar loadings depending on the operating temperature. The temperature history is therefore an important aspect that would need to be considered when interpreting peak strain measurements. However, the magnetostatic results at relatively low levels of strain are similar and the magnetostatic response could be used to effectively measure the condition of the bolt. In addition, the incubation strains are similar for the three temperatures and this would complement this mode of operation. This approach is practical as high strains and the corresponding high stresses are undesirable in aircraft components.

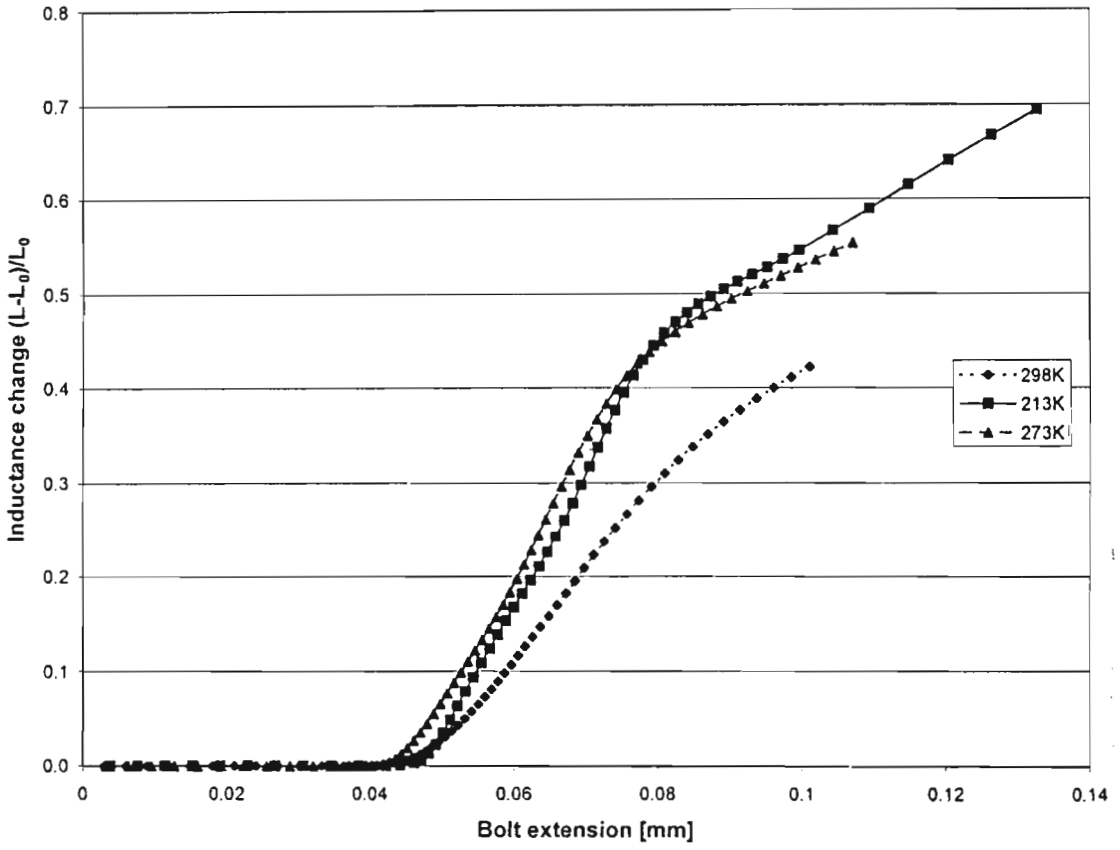

Figure 5.12: Inductance change vs. bolt extension for various temperatures

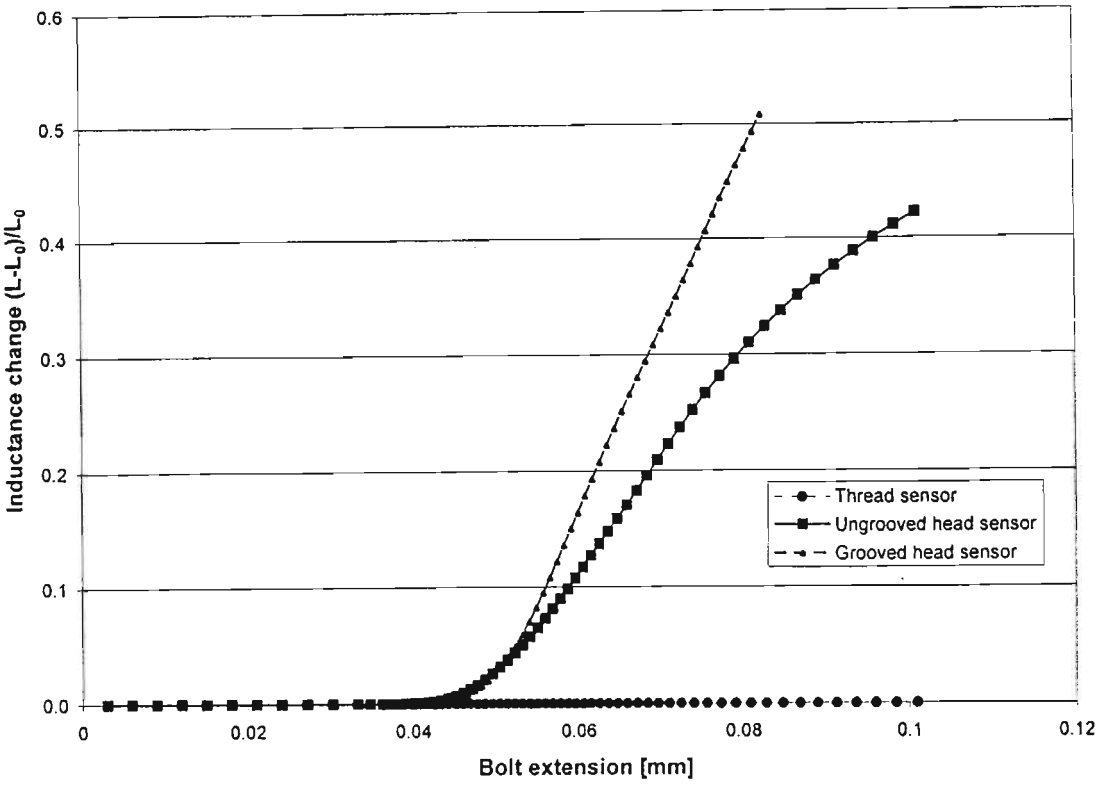

Figure 5.13: Inductance change measured for head sensors (both grooved and ungrooved) and thread sensor for TRIP aircraft bolt

Geometry effects

The results of mechanical analysis of the bolt indicated that two regions are potential sites for inductance measurements. The first region is located under the head and the second in the first thread root. The localised stress concentrations is these regions promote martensite transformation whilst the bolt is under a relatively low nominal load. Initially transformation is limited to the area in the thread root, however, continued loading causes transformation to develop in the shank-head fillet region which eventually becomes the dominant transformation area. This is clearly seen in figure 5.13 which includes the response curves for the two locations.

The change in inductance measured due to transformation in the thread root is

measurable but is considerably less than that for the shank-head fillet. The addition of the groove below the head of the bolt does increase the sensitivity of the bolt to the tensile loading as can be seen in figure 5.13, it can also be seen that the groove enhances the linearity of the sensor response. The evolution of martensite is shown for increasing extension values in figure 5.15

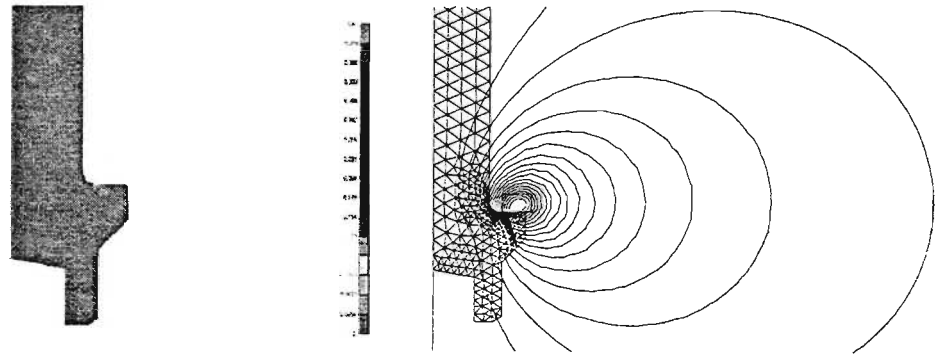

Bolt extension = 0.060 mm

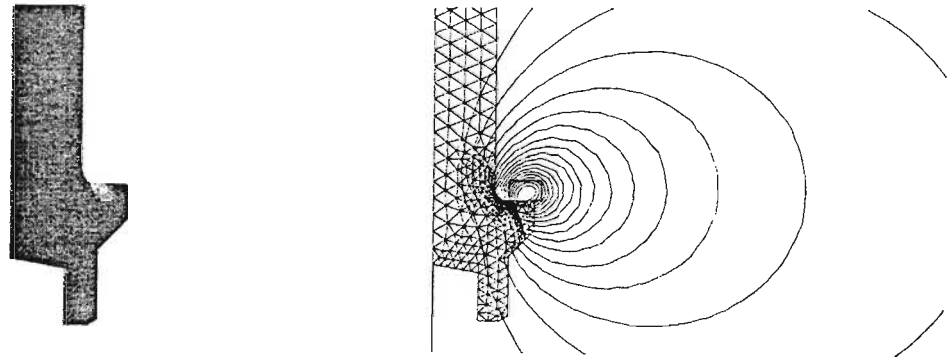

Bolt extension = 0.065 mm

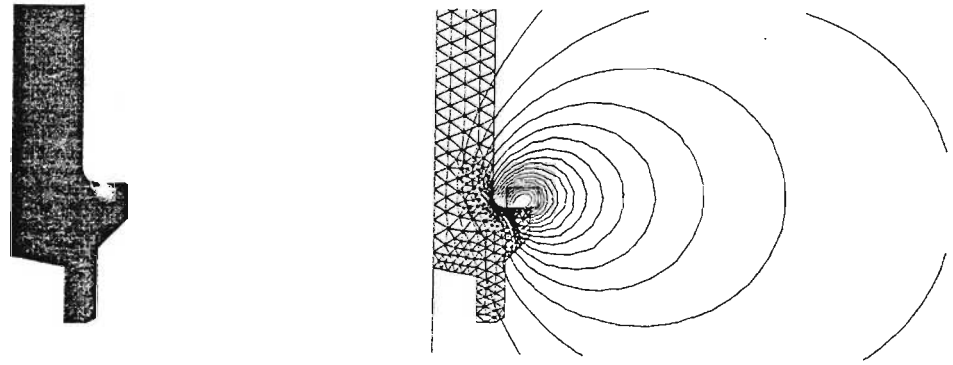

Bolt extension = 0.071 mm

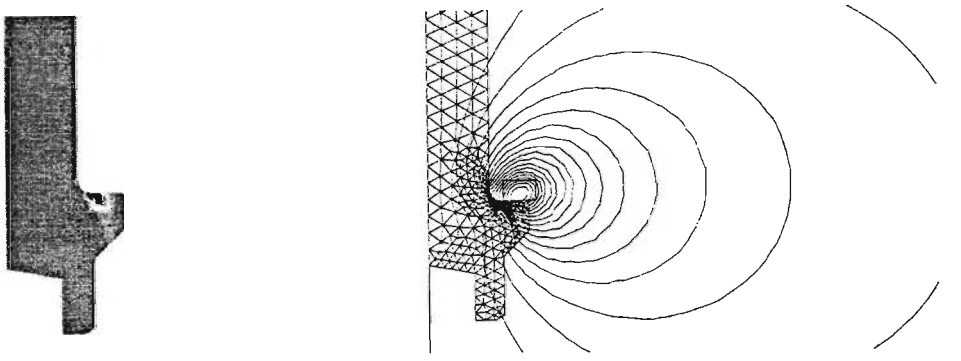

Bolt extension = 0.079 mm

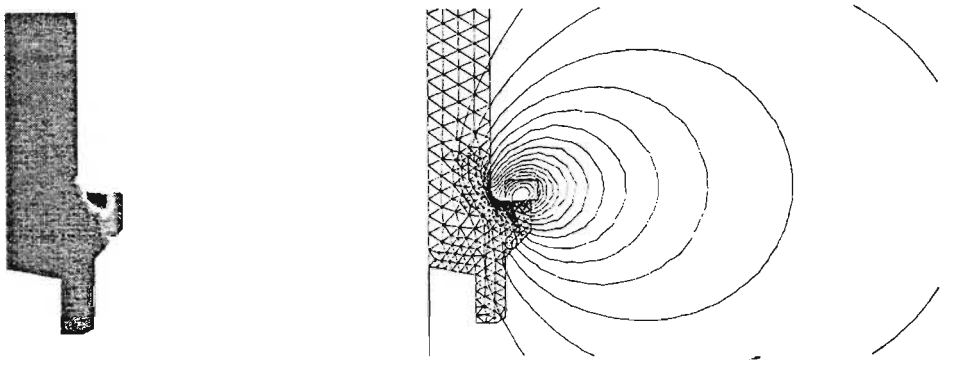

Bolt extension = 0.089 mm

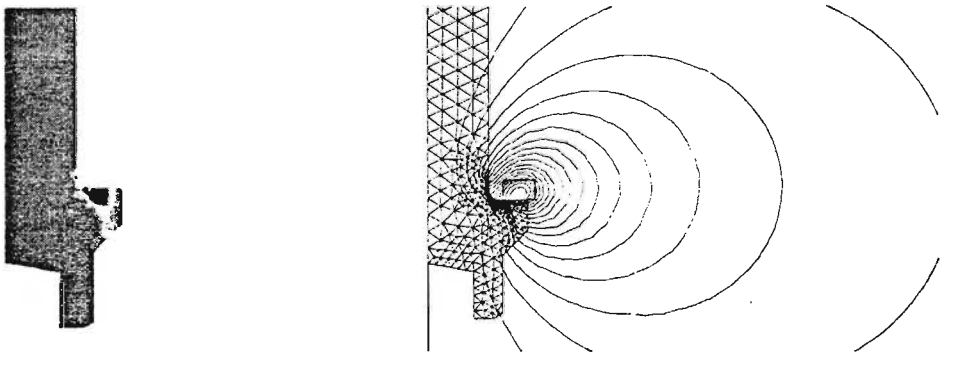

Bolt extension = 0.101 mm

Figure 5.14 Evolution of martensite and the corresponding magnetostatic response for increasing extension

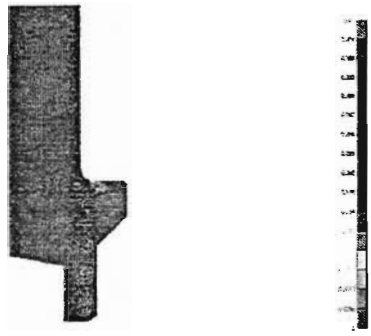

Bolt extension = 0.060 mm

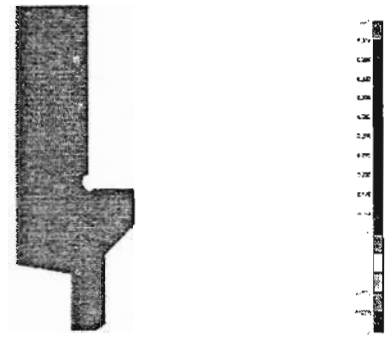

Bolt extension = 0.060 mm

Bolt extension = 0.065 mm

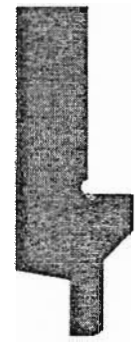

Bolt extension = 0.065 mm

Bolt extension = 0.071 mm

Bolt extension = 0.070 mm

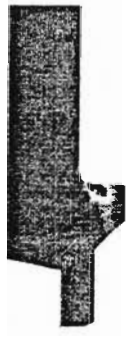

Bolt extension = 0.079 mm

Bolt extension = 0.074 mm

Bolt extension = 0.089 mm

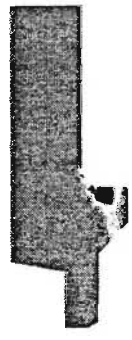

Bolt extension = 0.079 mm

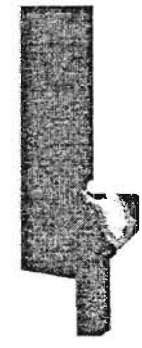

Bolt extension = 0.100 mm

Bolt extension = 0.082 mm

Figure 5.15 Comparison of the evolution of martensite for the ungrooved and grooved bolts

Chapter 6

Conclusion

Smart materials encompass a very broad range of materials which on the one hand can be manipulated under given input conditions or which have the inherent ability to indicate the amount of deformation. The damage indicating materials fall into two classes; materials which are composites of normal structural material and sensors to obtain feedback which will be referred to as class II smart materials, and those which contain an inherent feature that changes with deformation and therefore can be used as a damage indicator. These latter materials are referred to as class I smart materials. TRIP steels fall into the class I category. The inherent advantage of a class I smart material over a class II smart material is that the material can act a both structure and sensor simultaneously without any need for the attachment of sensors. In addition the class I smart materials will retain information useful in assessing damage regardless of what happens to the system in the event of power loss etc. This is an advantage when it comes to damage assessment and in the utilisation of passive monitoring systems for infrastructural concerns.

The foundations and some of the practical issues for the development of a mechanical-magnetostatic prediction capability have been presented in this work. The martensitic transformation that occurs in metastable TRIP steels as a result of plastic straining provides a method for the correlation of strain with applied load. The

prediction of martensite evolution as a function of load requires a well-developed and consistent constitutive model that couples the mechanical parameters with the evolution of martensite within the parent phase. The functional dependence of the martensite evolution on the strain and stress state within the material, various models describing the transformation kinetics and corresponding constitutive formulations were presented and discussed. The models range from relatively simple treatments in which only the plastic strain is considered to complex models in which the strain rate, the stress state and temperature influences are included.

The central goal of the methodology described here was the integration of finite element codes for the prediction of the mechanical and magnetostatic response of smart sensors based on strain memory alloys. The versatility and flexibility of the finite element method allows response predictions for a wide range of sensor geometries and materials to be considered. The approach presents an opportunity for the development of sensors that are optimised to provide maximum sensitivity for application in structural health monitoring systems.

The methodology developed to predict the mechanical and corresponding magnetostatic response of strain memory, specifically TRIP steel, components and structures was divided into two phases. The first phase involved the simulation of the martensite transformation as a function of applied loading, i.e. establishing the location and amount of transformed material. This was determined using the finite element method to develop a model incorporating the transformation kinetics and constitutive equations appropriate for TRIP steels. The finite element analyses were implemented as non-linear material models using an updated kinematic formulation based on the procedures. The martensite volume fraction was determined for each load increment as a function of the stress and strain increments for input into the magnetostatic model. Once the location and amount of transformed material was known a second finite element model was created, this being the magnetostatic model. The magnetostatic model was formulated to included the magnetic permeability of the TRIP steel which was adjusted for each load increment according to the amount of transformed material calculated for any given location within the

TRIP steel component. The magnetostatic models were analysed using a simple linear formulation.

In order to demonstrate the application of the numerical modelling methodology, two test-cases were presented. The tests-cases were derived from practical real-world examples of peak strain sensors that are currently under development. The aim of the analyses described was to determine the response of the electrical response characteristics of the peak strain sensors as a function of mechanical loading. The results of the analyses of the test cases compared well with the expected responses and the analyses demonstrated that the technique may be used to refine sensor geometries and arrangements to obtain maximum performance from the sensor. It was however noted that the technique is heavily reliant on accurate material data in the form of a well developed constitutive model. The response calculations carried out for the test cases were based on the use of a constitutive model for 304 stainless steel due to availability of test data for the material. Should a different material be used comprehensive testing would be required to identify the mechanical and transformation parameters required for accurate modelling.

Although the test cases presented here concentrated on the analysis of temperature effects and the influence of geometry, the methodology may be used to analyse other issues, for example, analyses run during the course of the work showed that coil geometry has a definite effect on sensor response and may be optimised to promote sensor efficiency. As the methodology is based on the use of finite element modelling, there exists great scope for additional work such as integration of the mechanical and magnetostatic models with optimisation routines that could rationally optimise sensor response and placement. This would be particularly beneficial in the case of the dual phase components where the part geometry may be complex and sensor location may be restricted.

Bibliography

[1] Hanagud, S., NageshBabu, G. L.and Zang, J., Smart Structures - An Overview, *Developments in Theoretical and Applied Mechanics Vol XVI*, ed. by Antar, B., The University of Tennessee Space Institute, TN, 1992.

[2] Thompson L., Westermo B., Crum D., Law W. and Trombi R., Smart Structural Fasteners for Aircraft and Construction Industries, *Proc.of the SPIE Conf. on Smart Structures and Materials*, Newport Beach, USA, 1999.

[3] Chang, F., Structural Health Monitoring: A Summary Report, *Structural Health Monitoring: Current Status and Perspectives*, ed. by Chang, F., CRC Press, 1997.

[4] Kudva, J. N., Smart Structures Concepts for Aircraft Structural Health Monitoring, *Proc. of the SPIE Conf. on Smart Structures and Materials*, Alburquerque, USA, 1993.

[5] Rogers, C. A., Liang, C. and Li, S., Active Damage Control of Hybrid Material Systems Using Induced Strain Actuators, *Proc. of the 32nd AIAA/ASME/ASCE/AHS/ASC Structures, Structural Dynamics and Materials Conf.*, Baltimore, USA, 1991.

[6] Fisher M. and Hill E., Neural Network Burst Pressure Prediction in Fibreglass/Epoxy Vessels using Acoustic Emission, *Proc. of the 6th International Symposium on Acoustic Emission from Composite Materials*, San Antonio, Texas, June 1998.

[7] Zackay, V., E. Parker, D. Fahr and R. Busch , The Enhancement of Ductility in High-Strength Steels, *Trans. of ASM*, **60**, pp. 252-259, 1967.

[8] Gerberich, W. W., C. Martin and V. Zackay, Serrated Stress-Strain Curves of Metastable Austenite in Alloy Steels, *Trans. of ASM*, **58**, pp. 85-94, 1965.

[9] Zackay, V. and E. R. Parker, Some Fundamental Considerations in the Design of High-Strength Metallic Materials, *Chap. 4 of High Strength Materials, Proc. of Berkeley Intl. Conf.*, June 15-18, 1964, ed. by V. F. Zackay, John Wiley and Sons, NY, pp. 130-166, 1965.

[10] Gerberich, W. W., P. L. Hemmings and V. Zackay, Preliminary Toughness Results on TRIP Steel, *ASM Trans.*, Tech. Notes 61, pp. 843-847, 1968.

[11] Antolovich, S., Fracture Toughness and Strain-induced Phase Transformation, T*rans. of Met. Soc. of AIME*, **242**, pp. 2371-2373, 1968.

[12] Gerherich, W. W., P. L. Hemmings, V. Zackay and E. R. Parker, Interactions Between Crack Growth and Strain Induced Transformation, in Fracture 1969, *Proc. Of 2nd Conf. On Fracture*, Brighton, England, April 1969, Ed. by B. L. Pratt, Chapman and Hall Ltd, England, pp. 288-305, 1969.

[13] Gold, V., and T. J. Koppenaal, Anomalous Ductility of TRIP Steel, *Trans. of ASM*, **62**, pp. 607-610, 1969.

[14] Hall, J. A., V. Zackay and E. R. Parker, Structural Observations in a Metastable Austenitic Steel, *Trans. of ASM*, **62**, pp. 965-976, 1969.

[15] Gerberich, W. W., K. L. Hemmings and V. F. Zackay, Observations of Strain-Induced Martensite Around a Crack, *Trans. of Met. Soc. AIME*, **245**, pp. 1124-1126, May 1969.

[16] Altstetter, C. and M. Rashid, Defects and Strengthening in Transformed Crystals, *Proc. of 2nd Intl. Conf. on Strength of Metals and Alloys*, Pacific Grove, CA, pp. 846-950, 1970.

[17] McCoy, R. A., W. W. Gerberich and V. F. Zackay, On the Resistance of TRIP Steel to Hydrogen Embrittlement, *Met. Trans.*, **1**, pp. 2031-2134, 1970.

[18] Gerberich, W. W., G. Thomas, E. R. Parker and V. F. Zackay, Metastable Austenites: Decomposition and Strength, Lawrence Berkeley Laboratory, Report UCRL- 20309, 1970.

[19] Gerberich, W. W., G. Thomas, E. R. Parker and V. Zackay, Metastable Austenites: Decomposition and Strength, *Proc. of 2nd Intl. Conf. on Strength of Metals and Alloys*, Pacific Grove, CA, pp, 894-899, 1970.

[20] Tamura, I., T. Maki, H. Hato, Y. Tomamato and M. Okada, Strength and Ductility of Austenitic Iron Alloys Accompanying Strain Induced Martensitic Transformation, *Proc.of 2nd Intl. Conf. on Strength of Metals and Alloys*, Pacific Grove, CA, pp. 900-904, 1970.

[21] Owen, W.S., Strengthening by Phase Transformation, *Proc.of 2nd Intl. Conf on Strength of Metals and Alloys*, Pacific Grove, CA, pp. 795-814, 1970.

[22] Antolovich and S. B. Singh, On the Toughness Increment Associated with Austenite to Martensite Phase Transformation in TRIP Steels, *Met. Trans.*, **2**, pp. 2135-2141, 1971.

[23] Gerberich, W. W., P. L. Hemmings and V. Zackay, Fracture and Fractography of Metastable Austenites, *Met. Trans.*, **2**, pp. 2243-2253, 1971.

[24] Webster, D., Development of a High Strength Stainless Steel with improved Toughness and Ductility, *Met. Trans,* **2**, pp. 2097-2104, 1971.

[25] Fahr, D., Stress and Strain Induced Formation of Martensite and its Effects on Strength and Ductility of Metastable Austenitic Stainless Steels, *Met. Trans.*, **3**, pp. 1893 1992, 1971.

[26] Chanani, G., V. Zackay and E. R. Parker, Tensile Properties of 0.05 to 0.2 pct Carbon TRIP Steels, *Met. Trans.*, **2**, pp. 133-139, 1971.

[27] Antolovich, S. and S. Singh, On the Toughness Increment Associated with the Austenite to Martensite Transformation in TRIP Steels, *Met. Trans.*, **2**, pp. 2135-2141, 1971.

[28] Chanani, G. R., S. Antolovich and W. W. Gerberich, Fatigue Crack Propagation in TRIP Steels, *Met. Trans.*, **3**, pp. 2661-2672, 1972.

[29] Lecroisey, F. and A. Pineau, Martensitic Transformations Induced by Plastic Deformation in the Fe-Ni-Cr-C System, *Met. Trans.*, **3**, pp. 387-396, 1972.

[30] Koppenaal, T. J., A Thermal Processing Technique for TRIP Steels, *Met. Trans.*, **3**, pp. 1549-1554, 1972.

[31] Antolovich, S. and D. Fahr, An Experimental Investigation of the Fracture Characteristics of TRIP alloys, *Eng. Frac. Mech.*, 4, pp. 133-144, 1972.

[32] Woodford, D.A., Cavitation Erosion Induced Phase Transformations in Alloys, *Met. Trans.*, **3**, pp.1137-1145, 1972.

[33] Bhandarkar, D., V. Zackay and E. R. Parker, Stability and Mechanical Properties of Some Metastable Austenitic Steels, *Met. Trans.*, **3**, pp, 2619-2631, 1972.

[34] Bhandarkar, D., V. F. Zackay, and E. R. Parker, Stability and Mechanical Properties of Some Metastable Austenitic Stainless Steels, Report LBL-125, June 1972.

[35] Guimaraes, J. R. and R. J. De Angelis, Stress-Strain Relationship During Transformation Enhanced Plasticity, *Met. Trans.*, **4**, pp. 2379-2381, 1973.

[36] Weiss, V. et al, The Relationships Between the Transformation Characteristics and the Fracture and Fatigue Properties of TRIP Steels, Syracuse University, report for AMMRC AD-773 712, AMMRC CTR 73-50, Dec. 1973

[37] Koppenaal, T. J., Research in Development of Improved TRIP Steels, Army Materials and Mechanical Research Centre, AD-756 953, final report, AMMRC CTR 73-4, Jan., 1973

[38] Abrassat, F., Stress Induced Martensitic Transformation in Two Carbon Stainless Steels, Applications to TRIP Steels, *Met. Trans.*, **4**, pp. 2205-2216, 1973.

[39] Parker, E. R. and V. Zackay, Enhancement of Fracture Toughness in High Strength Steel by Microstructural Control, *Eng. Frac. Mech.*, **5**, pp. 147-165, 1973.

[40] Chanani, G. and S. Antolovich, Low Cycle Fatigue of a High Strength Metastable Austenitic Steel, *Met. Trans.*, **5**, pp. 217-229, 1974.

[41] Breedis, J. F. and L. Kaufman, Formation of HCP and BCC Phases in Austenitic Iron Alloys, *Met. Trans.*, **2**, pp. 2359-2371, Sept. 1974.

[42] Maxwell, P. C., A. Goldberg and J. Shyne, Influence of Martensite Formed During Deformation on the Mechanical Behaviour of Fe-Ni-C Alloys, *Met. Trans.*, **5**, pp. 1319-1324, 1974.

[43] Maxwell, P. C., A. Goldberg and J. C. Shyne, Stress Assisted and Strain Induced Martensites in Fe-Ni-C alloys, *Met. Trans.*, **5**, pp. 1305-1318, 1974.

[44] Zackay, V. F., D, Bhandarkar and E. R. Parker, The Role of Deformation Induced Phase Transformation in the Plasticity of some Iron-Base Alloys, report LBL-2775, Aug. 1974.

[45] Olson, G. B. and M. Cohen, A General Mechanism of Martensitic Nucleation: Part I. General Concepts and the FCC to HCP Transformation, *Met. Trans.*, **7A**, pp. 1897-1904, Dec. 1976.

[46] Olson, G. B. and M. Cohen, A General Mechanism of Martensitic Transformations: Part II. FCC to BCC and Other Martensitic Transformations, *Met. Trans.*, **7A**, pp. 1905-1914, Dec. 1976.

[47] Olson, G. B. and M. Cohen, A General Mechanism of Martensitic Nucleation Part III. Kinetics of Martensitic Transformation, *Met. Trans.*, **7A**, pp. 1915-1923, Dec. 1976.

[48] Azrin, M, G. B. Olson and R. A. Gagne, Inhomogeneous Deformation and Strain Rate Effects in High-Strength TRIP Steels, *M S&E*, **23**, pp, 33-41, 1976.

[49] Strife, J.R., M. J. Carr, and G. S. Ansell, The Effect of Austenite Pre-strain Above Md Temperature on Martensitic Transformation in Fe-Ni-Cr-C Alloys, *Met. Trans.*, **8A**, pp, 1471-1484, Sept. 1977.

[50] Remy, L. and A. Pineau, Twinning and Strain-Induced FCC to HCP Transformation in the Fe-Cr-C System, *M S&E*, **28**, pp, 99-107, 1977

[51] Olson, G. B., M. Azrin and H. Band, AC-Permeability Measurement of Strain Induced Martensite During Tensile Deformation of TRIP Steels, U.S, Army Materials and Mechanics Research Center, Report AMMRC TR 77-10, March 1977.

[52] Olson, G. B. and M. Azrin, Transformation Behaviour of TRIP Steels, *Met. Trans.*, **9A**, pp. 713-721, 1979.

[53] Zackay, V., M. Bhandarkar and E. R, Parker, The Role of Deformation Induced Phase Transformation in the Plasticity of Some Iron-Base Alloys, *Chap. 11 in Advances in Deformation Processing*, Ed. by J. J. Burke and V, Weiss, Plenum Pub. Co., NY, NY, pp. 351-404, 1979.

[54] Azrin, M., G. Olson and R. A. Gagne, Warm Extrusion of TRIP Steels Process Control and Tensile Properties, *M S&E*, **40**, pp. 175-185, 1979.

[55] Olson, G. B., R Chair, M. Azrin and R. A. Gagne, Fatigue Strength of TRIP Steels, *Met. Trans.*, **11A**, pp. 1069-1071, 1980.

[56] Azrin, M., G. Olson, E. B. Kula and J. Marley, Soviet Progress in Thermomechanical Treatment of Metals, *J. App. Metalworking*, **1**, No. 2, 1980.

[57] Staudhammer, K. P., L. E. Murr and S. S. Hecker, Nucleation and Evolution of Strain Induced Martensitic (B.C.C.) Embryos and Substructure in Stainless

Steels: A Transmission Electron Microscope Study, *Acta Met.* , **31**, No. 2., pp. 267-274, 1983.

[58] Radcliffe, S. V. and E. B Kula, Deformation, Transformation and Strength, Chap. 12, pp. 321-363, ibid.

[59] Post, C. B. and W. S. Eberly, Stability of Austenite in Stainless Steels, *Trans. ASM*, **39**, pp. 868-890,1947.

[60] Angel, T., Formation of Martensite in Austenitic Stainless Steels, Effects of Deformation, Temperature, and Composition, *JISI*, pp. 165-174, May, 1954

[61] Cina, B., Effect of Cold Work on the Gamma Alpha Transformation in Some Fe-Ni-Cr Alloys, *JISI*, pp. 406-422, Aug, 1954.

[62] Fiedler, H, C., B. L. Averbach and M. Cohen, The Effect of Deformation on the Martensitic Transformation in Austenitic Stainless, *Trans. of ASM*, **47**, pp. 265-285, 1955.

[63] Form, G. W. and W. M. Baldwin, The Influence of Strain Rate and Temperature on the Ductility of Austenitic Stainless Steels, *Trans. of ASM*, **48**, pp. 474-485, 1956.

[64] Powell, G. W., E. R. Marshall, and W. A. Backofen, Strain Hardening of Austenitic Stainless Steels, *Trans. of ASM*, **50**, pp. 479-497, 1958.

[65] J. C. Shyne, V. F. Zackay, and D. J. Schmatz, The Strength of Martensite Formed from Cold-Worked Austenite, *Trans. of ASM*, **52**, pp. 346-361, 1960.

[66] Irvine, K. J., F. B Pickering and J. Garstone, The Effect of Composition on the Structure and Properties of Martensite, *JISI*, **196**, pp. 660-668, Sept. 1960.

[67] Morton, A. J. and C. M. Wayman, Theoretical and Experimental Aspects of the "225" Austenite Martensite Transformation in Iron Alloys," Acta Met., 14, pp. 1567-1581, 1966.

[68] Zackay, V. F., M. W. Justusson, and D. J. Schmatz, Strengthening by Martensitic Transformation, *Chap. 7, Strengthening Mechanisms in Solids*, ASM, pp. 179-216, 1962.

[69] Guntner, C. J. and R. P Reed, The Effect of Experimental Variables Including the Martensitic Transformation on the Low Temperature Mechanical Properties of Austenitic Stainless Steels, *Trans. of ASM*, **55**, pp. 399-419, 1962.

[70] Dulieu, D. and J. Nutting, Influence of Solute Additions on the Stacking Fault Energy of Iron Nickel-Chromium Austerities, *in Metallurgical Developments in High Strength Steels*, Special Report 86, JISI, pp.140-145, 1964.

[71] Crocker, A. G., Shear Resolution Applied to the Martensite Reaction in Steel, *Acta Met.*, **13**, pp. 815-825,1965.

[72] Bressanelli, J. P. and A. Moskowitz, Effects of Strain-Rate, Temperature, and Composition on Tensile Properties of Metastable Austenitic Stainless Steels, *Trans of ASM*, **59**, pp. 223-239, 1966.

[73] Raymond, L., W. W. Gerberich and C. Martin, The Role of Carbon in Ausforming, in High Strength Materials, *Proc. of Intl. Conf., Berkeley*, CA, June 15-18, 1964, ed. by V. Zackay, John Wiley and Sons, NY, NY, pp. 297-307, 1965.

[74] Phillips, R. and W. E. Duckworth, The Effect of Alloying Additions on the Ausforming Response of Steels, ibid, pp. 307-326.

[75] Thomas, G., D. Schmatz and W. W. Gerberich, Structure and Strength of Some Ausformed Steels, Chap. 7, pp. 251-297, ibid

[76] Abrassart, F., F. Lecroisey and A. Pineau, Martensitic Transformations and Plasticity in the Fe-Ni-Cr-C System, *Proc. 2nd Intl. Conf. on Strength of Metals and Alloys*, Pacific Grove, CA, pp. 905-909, 1970.

[77] Colling, D. A. and R. Kossowsky, Strengthening of Fe-Ni-Cr Alloy by Martensite-to-Austenite Reverse Transformation, *Proc. 2nd Intl. Conf. on Strength of Metals and Alloys*, Pacific Grove, CA, pp. 917-921, 1970.

[78] Smith, H. and D. R. West, The Strengthening of Stainless Steels by the Reverse Martensite Transformation, *Proc. 2nd Intl. Conf. on Strength of Metals and Alloys*, Pacific Grove, CA, pp. 892-893, 1970.

[79] Bolling, G. F. and R. H. Richman, The Plastic Deformation-Transformation of Paramagnetic FCC Fe-Ni-C Alloys, *Acta Met.*, **18**, pp. 673-681, 1970.

[80] Goodchild, D., W. T. Roberts and D. Wilson, Plastic Deformation and Phase Transformation in Textured Austenitic Stainless Steels, *Acta Met.*, **18**, pp. 1137-1145, 1970.

[81] Suzuki, T. and M. Wuttig, The Triggering Mechanism of the Martensitic Transformation, *Met. Trans.*, **3**, pp. 1555-1560, 1972.

[82] Pineau, A. G. and R. Pelloux, Influence of Strain-Induced Martensitic Transformations on Fatigue Crack Growth Rates in Stainless Steels, *Met. Trans.*, **5**, pp, 1103-1112, 1974.

[83] Hennessy, D., G. Steckel and C. Altstetter, Phase Transformation of Stainless Steel During Fatigue, *Met. Trans.*, **7A**, pp. 415-424, 1976.

[84] Kula, E. B. and M. Azrin, Thermomechanical Processing of Ferrous Alloys, *Advances in Deformation Processing*, Chapter 8, Ed. by Burke and Weiss, Plenum Pub. Corp., 1978.

[85] Zackay, V. F., Carlson and Jackson, High Nitrogen Austenitic Cr-Mn Steels, *Trans. of ASM*, **49**, pp. 509-525, 1956.

[86] Buhr, R. K., S. L. Gertsman, and J. Reekie, Transformation Products in Cold-Worked Austenitic Manganese Steel, *Trans. of ASM*, 1957.

[87] Schaller, F. and V. F. Zackaty, Low Temperature Embrittlement of Austenitic Cr-Mn-N-Fe Alloys, *Trans. of ASM*, **51**, pp. 609-628, 1959.

[88] Shyne, J., F. W. Schaller, and V. F. Zackay, The Tensile and Yield Strength of Cr-Mn-N Steels at Low Temperatures, *Trans. of ASM*, **52**, pp. 848-854, 1960.

[89] Drobnjak, D. J. and J. G. Parr, Deformation Substructure and Strain-Hardening Characteristics of Metastable Fe-Mn Austenites, *Met. Trans.*, **1**, pp. 759-765, April 1970.

[90] Lefevre, Tricot, Gueussier and Castro, Properties of a New Family of Stainless Steels without Nickel, *Met. Trans.*, **5**, Nov. 1974.

[91] Sipos, K., L. Remy, and A. Pineau, Influence of Austenite Predeformation on Mechanical Properties and Strain-induced Martensitic Transformations of a High-Manganese Steel, *Met. Trans.*, **7A**, pp. 857-864, June, 1976.

[92] Haddick, G. and L. Thompson, E. Parker and V. Zackay, The Development of Nickle Free Austenitic Stainless Steels for Ambient and Cryogenic Applications, Lawrence Berkeley Laboratory report LBL-7397, Feb. 1978.

[93] Thompson, L., and B. Westermo, The Utilisation of Metastable Peak-Strain-Indicating (PSI) Materials in Critical Lifeline Engineering Applications, *1992 ASME Pressure Vessel and Piping Conf. PVP Vol. 27*, Eds. A. C. Singhal, L. R. L. Wang and T. Ariman, pp. 97-106. American Society of Mechanical Engineers, New Orleans, 1992.

[94] Thompson, L. D. and B. Westermo, The Development of a New Strain Measurement Methodology for Structural Damage Assessment and Monitoring, *Advances in Instrumentation and Control, Instrument Society of America*, Vol. 47, Part 2, pp. 1295-1303, Houston, 1992.

[95] Westermo, B. and L. Thompson, A New Testing and Evaluation Technology for Damage Assessment and Residual Life Estimation in Aircraft Structures, *Proc.14th Aerospace Testing Seminar*, pp. 510, Manhattan Beach, CA, 1993.

[96] Thompson, L. and B. Westermo, A New Strain Measurement Technology for Material Damage Assessment, *Proc. North American Smart Material and Structures Conference*, ed. by J. S. Sirkis, pp. 380-391, Feb. 1994.

[97] Thompson, L. D. and B. D. Westermo, Applications of a New Solid-State Structural Health Monitoring Technology, *Proc. 2nd European Conference on Smart Structures and Materials*, Glasgow, Scotland, Oct. 1994.

[98] Westermo, B. D. and L. D. Thompson, Smart Structural Monitoring: A New Technology, *SENSORS*, 15-18 Nov. 1994.

[99] Thompson, L. and B. Westermo, Passive Monitoring Systems for Structural Damage Assessment, *Proc. 1995 North American Conf. On Smart Structures and Materials*, San Diego, CA, Mat. 1995.

[100] Westermo, B. and L. Thompson, Design and Evaluation of Passive and Active Structural Health Monitoring Systems for Bridges and Buildings, *Proc. 1995 North American Conf. On Smart Structures and Materials*, San Diego, CA, Mar. 1995.

[101] Dunning, J. S. and L. D. Thompson, Development of Smart Solid State Structural Damage Assessment Systems for Underground Facilities, *Proc.1995 North American Conf. On Smart Structures and Materials*, San Diego, CA, Mar. 1995,

[102] Thompson, L. D. and B. D. Westermo, Development of Smart Structural Attachment Fixtures, *Proc. 1996 North American Conf. On Smart Structures and Materials*, San Diego, CA, Feb 1996.

[103] Westermo, B., A passive Structural Health Monitoring System for Bridges, *Proc. 1996 NDT Conference*, San Diego, CA, Feb, 1996.

[104] Thompson, L., B. Westermo and R. Waldbusser, Smart Materials Based Structural Health Monitoring Systems Development for Aerospace Applications, *Proc. 42nd International Instrumentation Symposium*, San Diego, CA, May 1996.

[105] Forsythe, G. E. and Wasow, W. R., *Finite Difference Methods for Partial Differential Equations*, John Wiley and Sons, New York, 1960.

[106] Richtmeyer, R. D. and Morton, K. W., *Difference Methods for Initial-Value Problems*, 2nd ed., Wiley-Interscience, New York, 1967.

[107] Huebner, K. H. and Thornton, E. A., *The Finite Element Method for Engineers*, John Wiley and Sons, Toronto, 1982.

[108] Kapkowski, J., *A Finite Element Study of Elastic Plastic Stress Distributions in Notched Specimens under Tension*, Meddelelse SKB II/M 13, Department of Ship Structures, The Technical University of Norway, 1968.

[109] Gallagher, R. H., Gellatly, R. A., Padlog, J. and Mallett, R. H., (1967), A Discrete Element Procedure for Thin-Shell Instability Analysis, *AIAA Journal*, **5**, No. 1.

[110] Zienkiewicz, O. C., *The Finite Element Method in Structural and Continuum Mechanics*, McGraw-Hill Book Company, New York, 1968.

[111] Courant, R., Variational Methods for the Solutions of Problems of Equilibrium and Vibrations, *Bull. Am. Math. Soc.*, **49**, 1943.

[112] Euler, L., *Methods Inveniendi Lineas Curvas Maximi Minimine Proprietate Gaudentes'*, M. Bousquet, Lausanne and Geneva, 1774.

[113] Polya, G., Sur une Interpretation de la Methode des Differences Fines Qui Peut Fournir des Bornes Superieures ou Inferieures', *C. R. Acad. Sci.*, **235**, 1952.

[114] Polya, G., *Estimates for Eigenvalues: Studies Presented to Richard von Mises'*, Academic Press, New York, 1954.

[115] Hersch, J., Equations Differentielles et Fonctions de Cellules, *C. R. Acad. Sci.*, **240**, 1995.

[116] Weinberger, H. F., Upper and Lower Bounds for Eigenvalues by Finite Difference Methods, *Commun. Pure Appl. Math*, **9**, 1956.

[117] Weinberger, H. F., Lower Bounds for Higher Eigenvalues by Finite Difference Methods, *Pac. J. Math.*, **8**, 1958.

[118] Greenstadt, J., On the Reduction of Continuous Problems to Discrete Form, *IBM J. Res. Dev.*, **3**, 1959.

[119] Morse, P. M. and Feshback, H., *Methods of Theoretical Physics*, McGraw-Hill Book Company, New York, 1953.

[120] White, G. N., *Difference Equations for Plane Thermal Elasticity*, LAMS-2745, Los Alamos Scientific Laboratory, Los Alamos, New Mexico, 1962.

[121] Friedrichs, K. O., *A Finite Difference Scheme for the Neumann and the Dirichlet Problem*, NYO-9760, Courant of Mathematical Sciences, New York University, New York, 1962.

[122] Cea, J., Approximation Variationnelle des Problemes aux Limites, *Ann. Inst. Fourier*, **14**, 1964.

[123] Kellogg, R. B., Difference Equations on a Mesh Arising from a General Triangulation', *Math. Comp.*, **18**, 1964.

[124] Kellogg, R. B., Ritz Difference Equations on a Triangulation, *Proc. of the Conf. on the Application of Computing Methods to Reactor Problems*, Argonne National Laboratory, 1965.

[125] Ciarlet, P. G., *Variational Methods for Non-Linear Boundary Value Problems*, Thesis, Case Institute of Technology, Cleveland, Ohio, 1966.

[126] Oganesjan, L. A., Convergence of Difference Schemes in Case of Improved Approximation of the Boundary (in Russian), *Zh. Vychisl. Mat. Mat. Fiz.*, **6**, 1966.

[127] Varga, R. S., Hermite Interpolation-Type Ritz Methods for Two- Point Boundary Value Problems, *Numerical Solutions of Partial Differential Equations*, ed. J. H. Bramble, Academic Press, New York, 1967.

[128] Friedrichs, K. O. & Keller, H. B., A Finite Difference Scheme for Generalized Neumann Problems, *Numerical Solutions of Partial Differential Equations*, J. H. Bramble (ed.), Academic Press, New York, 1967.

[129] Aubin, J. P., Approximation des Espaces de Distributions et des Operateurs Differentiels, *Bull. soc. Math. Fr.*, Mem. 12, 1667.

[130] Ciarlet, P. G., Schultz, M. H. & Varga, R. S., Numerical Methods of High-Order Accuracy for Non-Linear Boundary Value Problems. I: One-Dimensional Problem, *Numer. Math.*, **9**, 1967.

[131] Goel, J.J., Construction of Basic Functions for Numerical Utilization of Ritz's Method', *Numer. Math.*, **12**, 1967.

[132] Zlamal, M., On the Finite Element Method, *Numer. Math.*, **12**, 1968.

[133] Birkhoff, G., Schultz, M. H. & Varga, R. S., Piecewise Hermite Interpolation in One and Two Variables with Applications to Partial Differential Equations, *Numer. Math.*, **11**, 1968.

[134] Schultz, M. H., L-Multivariate Approximation Theory, *SIAM J. Numer. Anal.*, **6**, 1969.

[135] Zenisek, A., Interpolation Polynomials on the Triangle, *Numer. Math.*, **15**, 1970.

[136] Bramble, J. H. and Zlamal, M., Triangular Elements in the Finite Element Method, *Math. Comp.*, **24**, 1970.

[137] Carlson, R. E. and Hall, C. A., Ritz Approximation to Two- Dimensional Boundary Value Problems, *Numer. Math.* , **18**, 1971.

[138] Babuska, I., The Rate of Convergence for the Finite Element Method, *SIAM J. Numer. Anal.*, **8**, 1971.

[139] Babuska, I., Error Bounds for the Finite Element Method, *Numer. Math.*, **16**, 1971.

[140] Fix, G. and Nassif, N., On Finite Element Approximations to Time-Dependent Problems, *Numer. Math.*, **19**, 1972.

[141] Yamamoto, Y. and Tukuda, N., A Note on the Convergence of Finite Element Solutions, *Int. J. Numer. Methods, 15, 1972*

[142] Fried, I., Discretization and Computational Errors in High-Order Finite Elements, *AIAA Journal*, **9**, 1972.

[143] Fried, I., Accuracy of Complex Finite Elements, *AIAA Journal*, **10**, 1972.

[144] Oden, J. T., *Finite Elements of Nonlinear Continua*, McGraw-Hill Book Company, New York, 1972.

[145] Birkhoff, G. and Garabedian, H. L., Smooth Surface Interpolation, *J. Math. Phys.*, **39**, 1960.

[146] De Boor, C., Bicubic Spline Interpolation, *J. Math. Phys.*, **41**, 1962.

[147] Birkhoff, G. and De Boor, C., Piecewise Polynomial Interpolation and Approximation, *Approximation of Functions*, ed. H. L. Garabedian, Elsevier Publishing Company, Amsterdam, 1965.

[148] Ahlberg, J. H., Nilson, E. N. and Walsh, J. L., *The Theory of Splines and Their Applications*, Academic Press, New York, 1967.

[149] Prenter, P. M., *Splines and Variational Methods*, John Wiley and Sons, New York, 1975.

[150] Gordon, W. J., Distributive Lattices and the Approximation of Multivariate Functions, *Proc. of the Symposium on Approximation with Special Emphasis on Spline Functions*, University of Wisconsin, May 5-7, 1969, Academic Press, New York.

[151] Schoenberg, I. J. (ed.), *Approximations with Special Emphasis on Spline Functions*, Academic Press, New York, 1969.

[152] Gordon, W. J., Spline-Blended Surface Interpolation Through Curve Networks, *J. Math. Mech.*, **19**, 1969.

[153] Greville, T. N. E. (ed.), *Theory and Applications of Spline Functions*, Academic Press, New York, 1969.

[154] Varga, R. S., Functional Analysis and Approximation Theory in Numerical Analysis, *SIAM* (Regular Conference Series in Applied Mechanics), Philadelphia, Pennsylvania, 1971.

[155] Strang, W. G. and Fix, G., *An Analysis of the Finite Element Method*, Prentice-Hall, Englewood Cliffs, N.J., 1974.

[156] Babuska, I. and Aziz, A. K., (ed.), *The Mathematical Foundations of the Finite Element Method - With Applications to Partial Differential Equations*', Academic Press, New York, 1973.

[157] Whiteman, J. (ed.), *The Mathematics of Finite Elements and Applications*, Academic Press, New York, 1973.

[158] Oden, J. T., Some Aspects of Recent Contributions to the Mathematical Theory of Finite Elements, *Advances in Computational Methods in Structural Mechanics and Design, Proc. of the 2nd U.S.-Japan Seminar*, University of Alabama Press, Huntsville, Alabama, 1974.

[159] Hrenikoff, A., Solution of Problems in Elasticity by the Framework Method, *J. Appl. Mech.*, **8**, 1941.

[160] McHenry, D., A Lattice Analogy for the Solution of Plane Stress Problems, *J. Inst. Civ. Eng.*, **21**, 1943.

[161] Newmark, N. M., *Numerical Methods of Analysis in Engineering*, ed. L. E. Grinter, Macmillan Company, New York, 1949.

[162] Argyris, J. H., Energy Theorems and Structural Analysis', *Aircraft Eng.*, **26**, 1954.

[163] Argyris, J. H., Energy Theorems and Structural Analysis, *Aircraft Eng.*, 27, 1955.

[164] Argyris, J. H., The Matrix Analysis of Structures with Cut-Outs and Modifications, *Proc. of the 9th International Congress on Applied Mechanics, Section II: Mechanics of Solids, 1956.*

[165] Argyris, J. H. and Kelsey, S., Structural Analysis by the Matrix Force Method with Applications to Aircraft Wings, *Wiss. Ges. Luftfahrt Jahrb*, 1956.

[166] Argyris, J. H., The Matrix Theory of Statics, *Ing. Arch.*, **25**, 1957.

[167] Argyris, J. H. and Kelsey, S., The Analysis of Fuselages of Arbitrary Cross-Section and Taper, *Aircraft Eng.*, **31**, 1959.

[168] Argyris, J. H. and Kelsey, S., *Energy Theorems and Structural Analysis*, Butterworth and Company, London, 1960.

[169] Turner, M. J., Clough, R. W., Martin, H. C. & Topp, L. C., Stiffness and Deflection Analysis of Complex Structures, *J. Aeronaut. Sci.*, **23**, 1956.

[170] Clough, R. W., The Finite Element Method in Plane Stress Analysis, *Proc.of 2nd ASCE Conference on Electronic Computation*, Pittsburgh, PA,1960.

[171] Besseling, J. F., The Complete Analogy Between the Matrix Equations and the Continuous Field Equations of Structural Analysis, *International Symposium on Analogue and Digital Techniques Applied to Aeronautics*, Liege, Belgium, 1963.

[172] Melosh, R. J., Basis for the Derivation of Matrices for the Direct Stiffness Method, *AIAA Journal*, **1**, 1963.

[173] De Veubeke, B. F., *Upper and Lower Bounds in Matrix Structural Analysis, AGARD-ograph 72*, ed. B. F. de Veubeke, Pergamon Press, New York, 1964.

[174] Jones, R. E., A Generalization of the Direct-Stiffness Method of Structural Analysis, *AIAA Journal*, **220**, 1965.

[175] Zienkiewicz, O. C. and Cheung, Y. K., Finite Elements in the Solution of Field Problems, *Engineer*, **220**, 1965.

[176] Oden, J. T. and Reddy, J. N., *An Introduction to the Mathematical Theory of Finite Elements*, John Wiley and Sons, New York, 1976.

[177] Hildebrand, F. B., *Methods of Applied Mathematics*', Prentice- Hall, Englewood Cliffs, N.J., 1965.

[178] Oden, J. T. and Somogyi, D., Finite Element Applications in Fluid Dynamics, *Proc. ASCE J. Eng. Mech. Div.*, **95**, 1969

[179] Zienkiewicz, O. C., *The Finite Element Method*, 3rd Ed., McGraw-Hill Book Company, New York, 1977.

[180] Felippa, C. A. and Clough, R. W., The Finite Element Method in Solid Mechanics', in *SIAM-AMS Proceedings*, Vol. 2, American Mathematical Society, Providence, R.I, pp. 210-252, 1970.

[181] Oliveira, E. R. A., Theoretical Foundations of the Finite Element Method', *Int. J. Solids Struct.*, Vol. 4, pp. 929-952, 1968.

[182] Pian, T.H.H. and Tong, P.,Basis of Finite Element Methods for Solid Continua', *Int. J. Numer. Methods Eng.*, **1**, p. 26, 1969.

[183] Lowther, D.A., Freeman, E.M. and Forghani B., A sparse matrix open boundary method for finite element analysis, *IEEE Transactions on Magnetics*, **25**(4), pp. 2810-2812, July 1989.

[184] Freeman, E.M and Lowther, D.A, An open boundary technique for axisymmetric and three dimensional magnetic and electric field problems, *IEEE Transactions on Magnetics*, **25**(5), 4135-4137, September 1989.

[185] Zienkiewicz, O.C., Arlett, P.L. and Bahrani, A.L., Solution of three-dimensional field problems by the finite element method, *The Engineer*, **27** October 1967.

[186] Silvester, P. and Hsieh M.S., Non-linear magnetic field analysis of D.C. machines, *IEEE Transactions on Magnetics*, **7**, 5-89, 1970

[187] Silvester, P. and Hsieh M.S., Finite element solution of two dimensional exterior field problems, *Proc. IEEE.* **118**, 1971

[188] Silvester, P.P., *Finite Elements for Electrical Engineers,* Cambridge University Press, 1990

[189] Fletcher, C.A., *Computational techniques for fluid dynamics*, Springer-Verlag, 1998G.

[190] B. Olson and M. Cohen, *Metall. Trans.* **13A**, 1907, 1982

[191] T. Narutani, G. B. Olson and M. Cohen, *J. Physique* **43**, C4-429, 1982

[192] Kurdjumov, G. V., Phenomena occuring in the quenching and tempering of steel, *12th Hatfield Memorial Lecture J.I.S.I.*, **195**, 26, 1960

[193] Kuafman, L. and Cohen, M., Thermodynamics and kinetics of martensite transfromations. *Prog. in Metal Physics*, **7**, 165, 1958

[194] Thomas, G., Electron microscopy investigations of ferrous martensites. *Met. Trans.*, **2**, 2373, 1971

[195] Honeycombe, R. W. K., *Steels Microstructure and Properties*, Edward Arnold, London,1981

[196] Olson, G.B. and Cohen, M., Kinetics of strain-induced martensitic nucleation. Met. Trans., **6A**, 791, 1975

[197] Venables, J. A., *Phil. Mag.*, **7**, 35, 1964

[198] Stringfellow, R. G., Parks, D. M. and Olson G. B., A constitutive model for transformation plasticity accompanying strain-induced martensitic transformations in metastable austenitic steels. *Acata. Mettall.* **40**, 1703, 1992

[199] Hecker, S. S., Stout, M. G., Staudhammer, K. P. and Smith, J. I., Effects of strain state and strain rate on deformation-induced transformation in 304 stainless steel: part I. Magnetic measurments and mechanical behaviour. *Met. Trans.*, **13A**, 619, 1982

[200] Tomita, Y. and Iwamoto, T., Constitutive modeling of TRIP steel and its application to the improvement of mechanical properties. *Int. J. Mech. Sci.*, **37**, 1295, 1995

[201] Tomita, Y. and Iwamoto, T, Investigation on deformation mode depenence of strain-induced martensitic transformation in TRIP steels and modelling of transformation kinetics, *Int. J. Mech. Sci.*, **40**, 173, 1998

[202] Aernoudt, E. P., van Houtte and Leffers, T., Chapter 3: Deformation and Textures of Metals at Large Strains, Vol 6., ed. Mughrabi,1993

[203] Nemat-Nasser, S. and Hori, M., Micromechanics: Overall Properties of Heterogenous Materials. *North Holland Series in Applied Mathematics and Mechanics*, North Holland, Amsterdam, 1993

[204] Stouffer, D. C. and Dame, L. T, *Inelastic Defomoration of Metals.* John Wiley, New York, 96.

[205] Eshelby, J. D., *Proc. R. Soc. London* **A 241**, 376, 1957

[206] Mura, T., *Micromechanics of Defects in Solids.* Martinus Nijhoff, Dordrecht, 1987

[207] Indenbom, V. L. and Orlov, S .S., Sov. Phys.- JETP **6**, 274, 1967

[208] Olson, G. B. Innovations in ultrahigh-strength steel technology, *34th Sagamore Army Materials Conference Proceedings,* 3, 1990

[209] Anand, L., *Int. J. Plas.* **1**, 213, 1985

[210] Hutchinson, J. W and Tvergaard, V., *ASTM STP 1020*, 61, 1989

[211] Olson, G. B., Tsuzaki, K. and Cohen, M., *Mat. Res. Soc. Symp. Proc.* **57**, 129, 1987

[212] Tomita, Y., Shindo, A. and Sasayama, T., Plane strain tension of themo-elasto-viscoplastic blocks, *Int. J. Mech. Sc.* **32**, 613, 1990

[213] Miller, M.P. and McDowell, D. L., Modeling large strain multiaxial effects in FCC ploycrystals, *Int. J. Plas.* **12**(7), 875, 1996

[214] Tomita, Y., and Shibutani, Y., Estimation of deformation behaviour of TRIP steels: smooth/ringed-notched specimens under mnotonic and cyclic loading. *Int. J. Plasticity*, **16**, 769, 2000.